



**A description of
MEDUSA-2.0**

A. Yool et al.

MEDUSA-2.0: an intermediate complexity biogeochemical model of the marine carbon cycle for climate change and ocean acidification studies

A. Yool, E. E. Popova, and T. R. Anderson

National Oceanography Centre; University of Southampton Waterfront Campus, European Way, Southampton SO14 3ZH, UK

Received: 31 January 2013 – Accepted: 5 February 2013 – Published: 21 February 2013

Correspondence to: A. Yool (axy@noc.ac.uk)

Published by Copernicus Publications on behalf of the European Geosciences Union.

Title Page

Abstract

Introduction

Conclusions

References

Tables

Figures

⏪

⏩

◀

▶

Back

Close

Full Screen / Esc

Printer-friendly Version

Interactive Discussion



Abstract

MEDUSA-1.0 (**M**odel of **E**cosystem **D**ynamics, nutrient **U**tutilisation, **S**equestration and **A**cidification) was developed as an “intermediate complexity” plankton ecosystem model to study the biogeochemical response, and especially that of the so-called “biological pump”, to anthropogenically-driven change in the World Ocean (Yool et al., 2011). The base currency in this model was nitrogen from which fluxes of organic carbon, including export to the deep ocean, were calculated by invoking fixed C : N ratios in phytoplankton, zooplankton and detritus. Since the beginning of the industrial era, the atmospheric concentration of carbon dioxide (CO₂) has significantly increased above its natural, inter-glacial background concentration. Simulating and predicting the carbon cycle in the ocean in its entirety, including ventilation of CO₂ with the atmosphere and the resulting impact of ocean acidification on marine ecosystems, therefore requires that both organic and inorganic carbon be afforded a full representation in the model specification. Here, we introduce MEDUSA-2.0, an expanded successor model which includes additional state variables for dissolved inorganic carbon, alkalinity, dissolved oxygen and detritus carbon (permitting variable C : N in exported organic matter), as well as a simple benthic formulation and extended parameterisations of phytoplankton growth, calcification and detritus remineralisation. A full description of MEDUSA-2.0, including its additional functionality, is provided and a multi-decadal hindcast simulation described (1860–2005), to evaluate the biogeochemical performance of the model.

1 Introduction

Since the beginning of the industrial era, the atmospheric concentration of carbon dioxide (CO₂) has significantly increased above its natural, inter-glacial background concentration. Further increases are predicted by climate models, e.g. to 450–650 ppm by the mid-21st-century (Houghton et al., 2001). Rising atmospheric CO₂ is mitigated by uptake on land and in the ocean, with the latter accounting for about 30 % of

GMDD

6, 1259–1365, 2013

A description of MEDUSA-2.0

A. Yool et al.

Title Page

Abstract

Introduction

Conclusions

References

Tables

Figures

◀

▶

◀

▶

Back

Close

Full Screen / Esc

Printer-friendly Version

Interactive Discussion



A description of MEDUSA-2.0

A. Yool et al.

Title Page

Abstract

Introduction

Conclusions

References

Tables

Figures

◀

▶

◀

▶

Back

Close

Full Screen / Esc

Printer-friendly Version

Interactive Discussion



anthropogenic emissions (Sabine et al., 2004). This uptake by the ocean is driven by what are known as the solubility and biological pumps, the former via dissolution of CO_2 in cold waters that are mixed to depth, and the latter as the sinking and downward mixing of organic matter into the ocean interior (Volk and Hoffert, 1985). Global warming will likely cause significant changes in ocean circulation, ecosystems and carbon export (Doney et al., 2012). Primary productivity, as calculated from ocean colour measurements, is decreasing (Behrenfeld et al., 2006), a result of changes in upper ocean temperature and stratification and their influence on nutrients for phytoplankton growth. Modelling studies have similarly indicated that increased stratification in response to future CO_2 emission scenarios leads to decreased primary production and associated export of carbon (e.g. Bopp et al., 2001; Steinacher et al., 2010).

The potential of the ocean to take up CO_2 from the atmosphere is vast because CO_2 is buffered by the carbonate chemistry of seawater, keeping concentrations low relative to other components (HCO_3^- and CO_3^{2-}). Ocean acidification is a further consequence of the chemical equilibrium in seawater because, as anthropogenic CO_2 invades, it combines with H_2O to form HCO_3^- and H^+ . Model hindcasts indicate that surface ocean pH has declined from its preindustrial value of 8.2 to 8.1 today, an increase in acidity of 30 % (Orr et al., 2005). Forward predictions indicate substantial further decreases, e.g. 0.3 to 0.4 pH units, by 2050 depending on future CO_2 emissions (Orr et al., 2005). The chemical impact of ocean acidification has the potential to affect ocean ecosystems and associated biogeochemistry in many ways (Doney et al., 2009). In particular, it leads to decreasing saturation state for the two main forms of calcium carbonate (CaCO_3) produced by marine calcifiers, aragonite and calcite. Coccolithophores, foramaniferans and pteropods are thus particularly vulnerable to such changes (Fabry et al., 2008; Gangstø et al., 2011). Acidification and decreasing CaCO_3 production have several consequences for the ocean carbon cycle. Production of CaCO_3 removes twice as much alkalinity as it does CO_2 from seawater (Frankignoulle et al., 1994) such that decreasing CaCO_3 leads to elevated $p\text{CO}_2$ and a negative feedback with the atmosphere. On the other hand, the rain ratio, i.e. the ratio of CaCO_3 : POC in sinking

particulate organic carbon Archer, 1991 will decline and with it carbon export flux to the deep ocean. Furthermore, if the export of organic carbon is closely bound by ballasting minerals including carbonate (Armstrong et al., 2002; Klaas and Archer, 2002), a decrease in CaCO_3 production could lead to a substantial shadowing of the depth scale of remineralisation (Heinze, 2004).

Previously, we introduced an “intermediate complexity” plankton model, MEDUSA-1.0: **M**odel of **E**cosystem **D**ynamics, nutrient **U**tutilisation, **S**equestration and **A**cidification (Yool et al., 2011). This model expanded beyond the traditional nutrient-phytoplankton-zooplankton-detritus (NPZD) models by having multiple currencies (N, Si and Fe) and by separating plankton into “small” and “large” size classes, yet incorporated sufficiently few tracers to be readily tractable in global ocean general circulation models. A multi-decadal hindcast simulation was undertaken and results presented for global nutrient fields, primary production, distributions of phytoplankton types and export of detritus. Here, we introduce MEDUSA-2.0, an expanded successor model which represents dissolved inorganic carbon (DIC) and $p\text{CO}_2$ in the ocean, thereby allowing the calculation of air–sea CO_2 fluxes as well as an explicit representation of ocean acidification and its impact on ecosystem processes. The new model includes additional state variables for dissolved inorganic carbon, alkalinity, dissolved oxygen and detritus carbon (permitting variable C : N in exported organic matter), as well as a simple benthic formulation and extended parameterisations of phytoplankton growth and detritus remineralisation. A full description of the additional functionality of MEDUSA-2.0 is provided. A multi-decadal hindcast simulation is described (1860–2005), and this hindcast is used to provide a means of evaluating the performance of MEDUSA-2.0.

A description of MEDUSA-2.0

A. Yool et al.

Title Page

Abstract

Introduction

Conclusions

References

Tables

Figures

◀

▶

◀

▶

Back

Close

Full Screen / Esc

Printer-friendly Version

Interactive Discussion



2 MEDUSA-2.0

2.1 State variables

MEDUSA-1.0 resolves 11 state variables distributed between the nitrogen (6), silicon (2) and iron (1) cycles. The remaining 2 state variables denote chlorophyll for each of the model's 2 phytoplankton classes. Because of its key role in organising marine productivity, nitrogen is MEDUSA-1.0's primary currency. In this framework, the cycling of carbon (and other elements) can only be estimated from the explicitly modelled elemental cycles, and then only if fixed stoichiometric relationships are assumed.

In order to incorporate the carbon and oxygen cycles, MEDUSA-2.0 adds a further 4 state variables to the existing framework. These include total dissolved inorganic carbon (DIC), total alkalinity (TA) and dissolved oxygen. The final additional state variable is detrital carbon for the slow-sinking component of non-living particulate organic carbon (POC). For simplicity, MEDUSA-2.0 retains MEDUSA-1.0's assumption of fixed C : N ratios for the plankton pools (phytoplankton, zooplankton), but since these pools do not have identical C : N ratios (e.g. zooplankton are assumed to have a lower ratio; Anderson, 2005) the flow of organic material to detrital pools, both slow- and fast-sinking, has a variable C : N ratio depending upon which processes (plankton mortality, zooplankton egestion) contribute to it. In the case of fast-sinking detritus, this is still handled implicitly within MEDUSA-2.0, so can be easily accommodated. Since slow-sinking detritus is already represented by an explicit nitrogen state variable, a corresponding carbon variable must be added to accommodate this. Note that, again for simplicity, iron is still coupled rigidly to nitrogen, so there is no corresponding state variable for detrital iron. Figure 1 presents a schematic diagram of MEDUSA-2.0, showing the state variables (pelagic and benthic) and the ecological connections between them.

GMDD

6, 1259–1365, 2013

A description of MEDUSA-2.0

A. Yool et al.

Title Page

Abstract

Introduction

Conclusions

References

Tables

Figures

◀

▶

◀

▶

Back

Close

Full Screen / Esc

Printer-friendly Version

Interactive Discussion



A description of MEDUSA-2.0

A. Yool et al.

Title Page

Abstract

Introduction

Conclusions

References

Tables

Figures

◀

▶

◀

▶

Back

Close

Full Screen / Esc

Printer-friendly Version

Interactive Discussion



The full list of 3-D water column state variables for MEDUSA-2.0 is as follows:

Pn	Non-diatom phytoplankton	mmol N m^{-3}
Pd	Diatom phytoplankton	mmol N m^{-3}
Chl _{Pn}	Chlorophyll in non-diatoms	mg chl m^{-3}
Chl _{Pd}	Chlorophyll in diatoms	mg chl m^{-3}
Pd _{Si}	Diatom phytoplankton (silicon)	mmol Si m^{-3}
Z _μ	Microzooplankton	mmol N m^{-3}
Z _m	Mesozooplankton	mmol N m^{-3}
D	Slow-sinking detritus (N)	mmol N m^{-3}
D _C	Slow-sinking detritus (C)	mmol C m^{-3}
N	Nitrogen nutrient	mmol N m^{-3}
S	Silicic acid	mmol Si m^{-3}
F	Iron nutrient	mmol Fe m^{-3}
DIC	Dissolved inorganic carbon	mmol C m^{-3}
ALK	Total alkalinity	meq m^{-3}
O ₂	Dissolved oxygen	$\text{mmol O}_2 \text{ m}^{-3}$

In addition to the state variables for the 3-D water column, 4 further state variables have been added to represent 2-D pools of organic and biogenic material at the seafloor. These pools permit temporary storage of particulate material before it is returned to dissolved pools, and they represent an extremely crude submodel of the benthic ecosystem. This approach contrasts with that in MEDUSA-1.0 in which all particulate material reaching the seafloor is instantaneously remineralised (or dissolved).

The primary reason for this addition is so that nutrient regeneration is not unrealistically accelerated by simplified model assumptions. This is particularly an issue in the shelf regions of the World Ocean where shallower water columns and strong vertical mixing can quickly return regenerated nutrients to surface waters and unrealistically fuel extra productivity. As in the case of the detritus (slow- and fast-sinking) that fuels

these seafloor pools, iron is rigidly coupled to nitrogen and does not have a separate benthic state variable. In principle, it could alternatively be coupled to carbon, but for parity with MEDUSA-1.0, its fate remains bound to that of nitrogen. The full list of 2-D state variables represented are:

B_N	Benthic organic nitrogen	mmolNm^{-2}
B_C	Benthic organic carbon	mmolNm^{-2}
B_{Si}	Benthic inorganic silicon	mmolSi^{-2}
B_{Ca}	Benthic inorganic CaCO_3	mmolCm^{-2}

The inclusion of the cycles of carbon, alkalinity and oxygen introduces a number of features to MEDUSA-2.0 that are relevant for studies of future climate change or ocean acidification. These include:

- gas exchange of dissolved CO_2 and O_2 with the atmosphere,
- a carbonate chemistry module for calculating properties such as the concentrations of carbonate species (H_2CO_3 , HCO_3^- , CO_3^{2-}), $p\text{CO}_2$ and pH,
- a dynamic lysocline depth calculated from the 3-D saturation state of calcium carbonate (specifically the calcite polymorph).

Alongside these major additions, MEDUSA-2.0 has a number of less significant differences from MEDUSA-1.0 that relate to aspects such as parameterisation and forcing. These differences include:

- forcing field of aeolian iron deposition replaced with that of Mahowald (2005),
- parameterisation of seafloor supply of dissolved iron added,
- phytoplankton growth parameterisation extended to include option of Liebig “law of the minimum” functionality,

A description of MEDUSA-2.0

A. Yool et al.

Title Page

Abstract

Introduction

Conclusions

References

Tables

Figures

◀

▶

◀

▶

Back

Close

Full Screen / Esc

Printer-friendly Version

Interactive Discussion



- Martin et al. (1987) and Henson et al. (2011) parameterisations of the remineralisation of fast-sinking detritus optionally available,
- options to use either fixed or dynamic rain ratios and lysocline depths.

A separate development with bearing on the work described here is the utilisation of surface forcing derived from coupled ocean–atmosphere models. This supplants the observationally-derived reanalysis forcing (DFS4.1; DRAKKAR Group, 2007) used previously with MEDUSA-1.0 (Yool et al., 2011). As well as permitting forecast simulations, adoption of such model-derived forcing permits hindcast simulations of the pre-industrial past prior to the ongoing anthropogenic transient. The specific forcing used here is described in Sect. 3.1.

2.2 Differential equations

The following partial differential equations describe the biogeochemical tendency terms that operate on MEDUSA-2.0’s state variables. Abbreviations used in the bracketed descriptions are: “PP” for primary production; “μzoo” for microzooplankton; “mzoo” for mesozooplankton; “non-lin” for non-linear; “remin” for remineralisation of organic material; “diss” for dissolution of inorganic material (e.g. opal or CaCO₃). The functional forms and parameters used in these equations are expanded upon in Sects. 2.3 and 2.4.

$$\frac{\partial P_n}{\partial t} = + \underbrace{[PP_{P_n} \cdot P_n]}_{\text{non-diatom PP}} - \underbrace{[G\mu_{P_n}]}_{\mu\text{zoo graze}} - \underbrace{[Gm_{P_n}]}_{\text{mzoo graze}} - \underbrace{[M1_{P_n}]}_{\text{linear losses}} - \underbrace{[M2_{P_n}]}_{\text{non-lin losses}} \quad (1)$$

$$\frac{\partial P_d}{\partial t} = + \underbrace{[PP_{P_d} \cdot P_d]}_{\text{diatom PP}} - \underbrace{[Gm_{P_d}]}_{\text{mzoo graze}} - \underbrace{[M1_{P_d}]}_{\text{linear losses}} - \underbrace{[M2_{P_d}]}_{\text{non-lin losses}} \quad (2)$$

$$\frac{\partial \text{Chl}_{Pn}}{\partial t} = \theta_{Pn}^{\text{Chl}} \cdot \xi^{-1} \cdot \left(+ \underbrace{[R_{Pn} \cdot PP_{Pn} \cdot Pn]}_{\text{non-diatom PP}} - \underbrace{[G\mu_{Pn}]}_{\mu\text{zoo graze}} - \underbrace{[Gm_{Pn}]}_{\text{mzoo graze}} - \underbrace{[M1_{Pn}]}_{\text{linear losses}} - \underbrace{[M2_{Pn}]}_{\text{non-lin losses}} \right) \quad (3)$$

$$\frac{\partial \text{Chl}_{Pd}}{\partial t} = \theta_{Pd}^{\text{Chl}} \cdot \xi^{-1} \cdot \left(+ \underbrace{[R_{Pd} \cdot PP_{Pd} \cdot Pd]}_{\text{diatom PP}} - \underbrace{[Gm_{Pd}]}_{\text{mzoo graze}} - \underbrace{[M1_{Pd}]}_{\text{linear losses}} - \underbrace{[M2_{Pd}]}_{\text{non-lin losses}} \right) \quad (4)$$

$$\frac{\partial Pd_{Si}}{\partial t} = + \underbrace{[PP_{PdSi} \cdot Pd_{Si}]}_{\text{diatom PP}} - \underbrace{[Gm_{PdSi}]}_{\text{mzoo graze}} - \underbrace{[M1_{PdSi}]}_{\text{linear losses}} - \underbrace{[M2_{PdSi}]}_{\text{non-lin losses}} - \underbrace{[DS_{PdSi}]}_{\text{dissolution}} \quad (5)$$

$$\frac{\partial Z\mu}{\partial t} = + \underbrace{[F_{Z\mu}]}_{\text{all grazing}} - \underbrace{[Gm_{Z\mu}]}_{\text{mzoo graze}} - \underbrace{[M1_{Z\mu}]}_{\text{linear losses}} - \underbrace{[M2_{Z\mu}]}_{\text{non-lin losses}} \quad (6)$$

$$5 \frac{\partial Zm}{\partial t} = + \underbrace{[F_{Zm}]}_{\text{all grazing}} - \underbrace{[M1_{Zm}]}_{\text{linear losses}} - \underbrace{[M2_{Zm}]}_{\text{non-lin losses}} \quad (7)$$

$$\frac{\partial D}{\partial t} = + \underbrace{[M2_{Pn}]}_{\text{non-diatom losses}} + \underbrace{[M2_{Z\mu}]}_{\mu\text{zoo losses}} + \underbrace{[(1 - D1_{\text{frac}}) \cdot M2_{Pd}]}_{\text{diatom losses}} + \underbrace{[(1 - D2_{\text{frac}}) \cdot M2_{Zm}]}_{\text{mzoo losses}} \quad (8)$$

$$+ \underbrace{[(1 - \beta_N) \cdot IN_{Z\mu}]}_{\mu\text{zoo egestion}} + \underbrace{[(1 - \beta_N) \cdot IN_{Zm}]}_{\text{mzoo egestion}} - \underbrace{[G\mu_D]}_{\mu\text{zoo graze}} - \underbrace{[Gm_D]}_{\text{mzoo graze}} - \underbrace{[M_D]}_{\text{remin}} - \underbrace{[w_g \cdot \frac{\partial D}{\partial z}]}_{\text{sinking}}$$

$$\frac{\partial D_C}{\partial t} = + \underbrace{[\theta_{Pn} \cdot M2_{Pn}]}_{\text{non-diatom losses}} + \underbrace{[\theta_{Z\mu} \cdot M2_{Z\mu}]}_{\mu\text{zoo losses}} + \underbrace{[\theta_{Pd} \cdot (1 - D1_{\text{frac}}) \cdot M2_{Pd}]}_{\text{diatom losses}} \quad (9)$$

Title Page

Abstract

Introduction

Conclusions

References

Tables

Figures

◀

▶

◀

▶

Back

Close

Full Screen / Esc

Printer-friendly Version

Interactive Discussion



Title Page

Abstract

Introduction

Conclusions

References

Tables

Figures

◀

▶

◀

▶

Back

Close

Full Screen / Esc

Printer-friendly Version

Interactive Discussion



$$\begin{aligned}
 & + \underbrace{[\theta_{Zm} \cdot (1 - D2_{frac}) \cdot M2_{Zm}]}_{\text{mzoo losses}} + \underbrace{[(1 - \beta_C) \cdot IC_{Z\mu}]}_{\mu\text{zoo egestion}} + \underbrace{[(1 - \beta_C) \cdot IC_{Zm}]}_{\text{mzoo egestion}} \\
 & - \underbrace{[G\mu_{Dc}]}_{\mu\text{zoo graze}} - \underbrace{[Gm_{Dc}]}_{\text{mzoo graze}} - \underbrace{[M_{Dc}]}_{\text{remin}} - \underbrace{\left[w_g \cdot \frac{\partial D_C}{\partial Z} \right]}_{\text{sinking}}
 \end{aligned}$$

$$\frac{\partial N}{\partial t} = - \underbrace{[PP_{Pn} \cdot Pn]}_{\text{non-diatom PP}} - \underbrace{[PP_{Pd} \cdot Pd]}_{\text{diatom PP}} + \underbrace{[\phi \cdot (G\mu_{Pn} + G\mu_D)]}_{\mu\text{zoo messy feeding}} \quad (10)$$

$$\begin{aligned}
 & + \underbrace{[\phi \cdot (Gm_{Pn} + Gm_{Pd} + Gm_{Z\mu} + Gm_D)]}_{\text{mzoo messy feeding}} + \underbrace{[E_{Z\mu}]}_{\mu\text{zoo excretion}} + \underbrace{[E_{Zm}]}_{\text{mzoo excretion}}
 \end{aligned}$$

$$\begin{aligned}
 & + \underbrace{[M1_{Pn}]}_{\text{non-diatom losses}} + \underbrace{[M1_{Pd}]}_{\text{diatom losses}} + \underbrace{[M1_{Z\mu}]}_{\mu\text{zoo losses}} + \underbrace{[M1_{Zm}]}_{\text{mzoo losses}} + \underbrace{[M_D]}_{\text{remin}} + \underbrace{[LD_N(k)]}_{\text{fast N remin}} + \underbrace{[BF_N]}_{\text{benthic remin}}
 \end{aligned}$$

$$\frac{\partial S}{\partial t} = - \underbrace{[PP_{Pd_{Si}} \cdot Pd_{Si}]}_{\text{diatom PP}} + \underbrace{[M1_{Pd_{Si}}]}_{\text{linear losses}} + \underbrace{[(1 - D1_{frac}) \cdot M2_{Pd_{Si}}]}_{\text{non-lin. losses}} + \underbrace{[DS_{Pd_{Si}}]}_{\text{dissolution}} \quad (11)$$

$$\begin{aligned}
 & + \underbrace{[(1 - D2_{frac}) \cdot Gm_{Pd_{Si}}]}_{\text{mzoo graze}} + \underbrace{[LD_{Si}(k)]}_{\text{fast Si detritus diss}} + \underbrace{[BF_{Si}]}_{\text{benthic diss}}
 \end{aligned}$$

$$\frac{\partial F}{\partial t} = - \underbrace{\left[R_{Fe} \cdot \frac{\partial N}{\partial t} \right]}_{\text{coupled to N}} + \underbrace{[F_{atmos}]}_{\text{aeolian}} + \underbrace{[F_{benth}]}_{\text{sediments}} - \underbrace{[F_{scavenge}]}_{\text{scavenging}} + \underbrace{[BF_{Fe}]}_{\text{benthic remin}} \quad (12)$$

$$\frac{\partial DIC}{\partial t} = - \underbrace{[\theta_{Pn} \cdot PP_{Pn} \cdot Pn]}_{\text{non-diatom PP}} - \underbrace{[\theta_{Pd} \cdot PP_{Pd} \cdot Pd]}_{\text{diatom PP}} + \underbrace{[\phi \cdot \theta_{Pn} \cdot G\mu_{Pn}]}_{\mu\text{zoo messy feeding, Pn}}$$

A description of
MEDUSA-2.0

A. Yool et al.

Title Page

Abstract

Introduction

Conclusions

References

Tables

Figures

◀

▶

◀

▶

Back

Close

Full Screen / Esc

Printer-friendly Version

Interactive Discussion



$$\begin{aligned}
 & + \underbrace{[\phi \cdot G_{\mu_{Dc}}]}_{\mu\text{zoo messy feeding, Dc}} + \underbrace{[\phi \cdot \theta_{Pn} \cdot G_{m_{Pn}}]}_{\text{mzoo messy feeding, Pn}} + \underbrace{[\phi \cdot \theta_{Pd} \cdot G_{m_{Pd}}]}_{\text{mzoo messy feeding, Pd}} + \underbrace{[\phi \cdot \theta_{Z\mu} \cdot G_{m_{Z\mu}}]}_{\text{mzoo messy feeding, Z}\mu} \\
 & + \underbrace{[\phi \cdot G_{m_{Dc}}]}_{\text{mzoo messy feeding, Dc}} + \underbrace{[R_{Z\mu}]}_{\mu\text{zoo respiration}} + \underbrace{[R_{Zm}]}_{\text{mzoo respiration}} + \underbrace{[\theta_{Pn} \cdot M1_{Pn}]}_{\text{non-diatom losses}} + \underbrace{[\theta_{Pd} \cdot M1_{Pd}]}_{\text{diatom losses}} \\
 & + \underbrace{[\theta_{Z\mu} \cdot M1_{Z\mu}]}_{\mu\text{zoolosses}} + \underbrace{[\theta_{Zm} \cdot M1_{Zm}]}_{\text{mzoolosses}} + \underbrace{[M_{Dc}]}_{\text{remin}} + \underbrace{[LD_C(k)]}_{\text{fast C remin}} - \underbrace{[FD_{CaCO_3}]}_{\text{CaCO}_3 \text{ production}} \\
 & + \underbrace{[LD_{CaCO_3}(k)]}_{\text{CaCO}_3 \text{ diss}} + \underbrace{[BF_C]}_{\text{benthic remin}} + \underbrace{[ASF_{CO_2}]}_{\text{air-sea gas exchange}}
 \end{aligned}$$

$$5 \quad \frac{\partial \text{ALK}}{\partial t} = - \underbrace{[2 \cdot FD_{CaCO_3}]}_{\text{CaCO}_3 \text{ production}} + \underbrace{[2 \cdot LD_{CaCO_3}(k)]}_{\text{CaCO}_3 \text{ diss}} + \underbrace{[BF_{CaCO_3}]}_{\text{benthic diss}} \quad (13)$$

$$\frac{\partial O_2}{\partial t} = + \underbrace{[\theta_{nit} \cdot PP_{Pn} \cdot Pn]}_{\text{non-diatom PP}} + \underbrace{[\theta_{nit} \cdot PP_{Pd} \cdot Pd]}_{\text{diatom PP}} - \underbrace{[\theta_{nit} \cdot \phi \cdot G_{\mu_{Pn}}]}_{\mu\text{zoo messy feeding, Pn}} \quad (14)$$

$$\begin{aligned}
 & - \underbrace{[\theta_{nit} \cdot \phi \cdot G_{\mu_{Dc}}]}_{\mu\text{zoo messy feeding, Dc}} - \underbrace{[\theta_{nit} \cdot \phi \cdot G_{m_{Pn}}]}_{\text{mzoo messy feeding, Pn}} - \underbrace{[\theta_{nit} \cdot \phi \cdot G_{m_{Pd}}]}_{\text{mzoo messy feeding, Pd}} - \underbrace{[\theta_{nit} \cdot \phi \cdot G_{m_{Z\mu}}]}_{\text{mzoo messy feeding, Z}\mu} \\
 & - \underbrace{[\theta_{nit} \cdot \phi \cdot G_{m_{Dc}}]}_{\text{mzoo messy feeding, Dc}} - \underbrace{[\theta_{nit} \cdot E_{Z\mu}]}_{\mu\text{zoo excretion}} - \underbrace{[\theta_{nit} \cdot E_{Zm}]}_{\text{mzoo excretion}} - \underbrace{[\theta_{nit} \cdot M1_{Pn}]}_{\text{non-diatom losses}} - \underbrace{[\theta_{nit} \cdot M1_{Pd}]}_{\text{diatom losses}} \\
 & - \underbrace{[\theta_{nit} \cdot M1_{Z\mu}]}_{\mu\text{zoolosses}} - \underbrace{[\theta_{nit} \cdot M1_{Zm}]}_{\text{mzoolosses}} - \underbrace{[\theta_{nit} \cdot M_D]}_{\text{remin}} - \underbrace{[\theta_{nit} \cdot LD_N(k)]}_{\text{fast N remin}} + \underbrace{[\theta_{rem} \cdot \theta_{Pn} \cdot PP_{Pn} \cdot Pn]}_{\text{non-diatom PP}}
 \end{aligned}$$

$$\begin{aligned}
& + \underbrace{[\theta_{\text{rem}} \cdot \theta_{\text{Pd}} \cdot \text{PP}_{\text{Pd}} \cdot \text{Pd}]}_{\text{diatom PP}} - \underbrace{[\theta_{\text{rem}} \cdot \theta_{\text{Pn}} \cdot \phi \cdot \text{G}\mu_{\text{Pn}}]}_{\mu\text{zoo messy feeding, Pn}} - \underbrace{[\theta_{\text{rem}} \cdot \phi \cdot \text{G}\mu_{\text{Dc}}]}_{\mu\text{zoo messy feeding, Dc}} \\
& - \underbrace{[\theta_{\text{rem}} \cdot \theta_{\text{Pn}} \cdot \phi \cdot \text{Gm}_{\text{Pn}}]}_{\text{mzoo messy feeding, Pn}} - \underbrace{[\theta_{\text{rem}} \cdot \theta_{\text{Pd}} \cdot \phi \cdot \text{Gm}_{\text{Pd}}]}_{\text{mzoo messy feeding, Pd}} - \underbrace{[\theta_{\text{rem}} \cdot \theta_{\text{Z}\mu} \cdot \phi \cdot \text{Gm}_{\text{Z}\mu}]}_{\text{mzoo messy feeding, Z}\mu} \\
& - \underbrace{[\theta_{\text{rem}} \cdot \phi \cdot \text{Gm}_{\text{Dc}}]}_{\text{mzoo messy feeding, Dc}} - \underbrace{[\theta_{\text{rem}} \cdot R_{\text{Z}\mu}]}_{\mu\text{zoo respiration}} - \underbrace{[\theta_{\text{rem}} \cdot R_{\text{Zm}}]}_{\text{mzoo respiration}} - \underbrace{[\theta_{\text{rem}} \cdot \theta_{\text{Pn}} \cdot \text{M1}_{\text{Pn}}]}_{\text{non-diatom losses}} \\
& - \underbrace{[\theta_{\text{rem}} \cdot \theta_{\text{Pd}} \cdot \text{M1}_{\text{Pd}}]}_{\text{diatom losses}} - \underbrace{[\theta_{\text{rem}} \cdot \theta_{\text{Z}\mu} \cdot \text{M1}_{\text{Z}\mu}]}_{\mu\text{zoo losses}} - \underbrace{[\theta_{\text{rem}} \cdot \theta_{\text{Zm}} \cdot \text{M1}_{\text{Zm}}]}_{\text{mzoo losses}} - \underbrace{[\theta_{\text{rem}} \cdot \text{M}_{\text{Dc}}]}_{\text{remin}} \\
& - \underbrace{[\theta_{\text{rem}} \cdot \text{LD}_{\text{C}}(k)]}_{\text{fast C remin}} - \underbrace{[\theta_{\text{nit}} \cdot \text{BF}_{\text{N}}]}_{\text{benthic remin}} - \underbrace{[\theta_{\text{rem}} \cdot \text{BF}_{\text{C}}]}_{\text{benthic remin}} + \underbrace{[\text{ASF}_{\text{O}_2}]}_{\text{air-sea gas exchange}}
\end{aligned}$$

The above equations are applied throughout the domain of the physical ocean model, without regard to horizontal or vertical position. This approach is inherited from MEDUSA-1.0 but differs from that of some other models (Popova et al., 2006) where different equations are applied in different volumes of the ocean to account, for instance, for photic and aphotic zones. Note that terms such as air-sea gas exchange, aeolian dust deposition and fluxes from the benthic submodel (see below) obviously only apply in ocean grid cells that are in contact with either the atmosphere or the benthos.

$$\frac{d\text{B}_{\text{N}}}{t} = + \underbrace{\left[w_{\text{g}} \cdot \frac{\partial \text{D}_{\text{N}}}{\partial z} \right]}_{\text{slow N deposit}} + \underbrace{[\text{T}_{\text{N}}(z)]}_{\text{fast N deposit}} - \underbrace{[\lambda_{\text{N}} \cdot \text{B}_{\text{N}}]}_{\text{benthic N remin}} \quad (15)$$

$$\frac{d\text{B}_{\text{Si}}}{t} = + \underbrace{[\text{T}_{\text{Si}}(z)]}_{\text{fast Si deposit}} - \underbrace{[\lambda_{\text{Si}} \cdot \text{B}_{\text{Si}}]}_{\text{benthic Si diss}} \quad (16)$$

Title Page

Abstract

Introduction

Conclusions

References

Tables

Figures

◀

▶

◀

▶

Back

Close

Full Screen / Esc

Printer-friendly Version

Interactive Discussion



$$\frac{dB_C}{t} = + \underbrace{\left[w_g \cdot \frac{\partial D_C}{\partial z} \right]}_{\text{slow C deposit}} + \underbrace{[T_C(z)]}_{\text{fast C deposit}} - \underbrace{[\lambda_C \cdot B_C]}_{\text{benthic C remin}} \quad (17)$$

$$\frac{dB_{Ca}}{t} = + \underbrace{[T_{Ca}(z)]}_{\text{fast deposit}} - \underbrace{[\lambda_{Ca} \cdot B_{Ca}]}_{\text{benthic Ca diss}} \quad (18)$$

Differential equations (15) to (18) describe the storage and release of biogenic material at the base of each water column in the model. Material enters these reservoirs as slow- and fast-sinking detritus, and is remineralised to DIN, iron, silicic acid, DIC and alkalinity. As with the rest of MEDUSA-2.0, iron is coupled via fixed stoichiometry to the nitrogen cycle and so is handled implicitly. Note that there is no horizontal communication between the benthic reservoirs in MEDUSA-2.0. Since release of material from the benthic reservoirs occurs at fixed specific rates, the above equations are complete.

2.3 Interaction functional forms

The following sections expand on the terms that appear above in MEDUSA-2.0's differential equations. Although MEDUSA-2.0 includes a number of new state variables as well as several additional biogeochemical processes, it largely overlaps MEDUSA-1.0 with regard to the form and parameterisation of shared processes. As such, and since this manuscript aims to provide a complete and standalone description of MEDUSA-2.0, there is repetition with the previously published description of MEDUSA-1.0. Parameter definitions and values are listed in Sect. 2.4.

2.3.1 Non-diatom limitation and growth

$$\theta_{Pn}^{Chl} = \frac{Chl_{Pn} \cdot \xi}{Pn} \quad (19)$$

$$\hat{\alpha}_{Pn} = \alpha_{Pn} \cdot \theta_{Pn}^{Chl} \quad (20)$$

GMDD

6, 1259–1365, 2013

A description of MEDUSA-2.0

A. Yool et al.

Title Page

Abstract

Introduction

Conclusions

References

Tables

Figures

◀

▶

◀

▶

Back

Close

Full Screen / Esc

Printer-friendly Version

Interactive Discussion



θ_{Pn}^{Chl} is the scaled chlorophyll to biomass ratio, while $\hat{\alpha}_{Pn}$ scales the initial slope of the photosynthesis–irradiance (P – I) curve, α_{Pn} , by this ratio so that phytoplankton with a high chlorophyll content have an elevated response to irradiance.

$$V_{Pn^T} = V_{Pn} \cdot 1.066^T \quad (21)$$

This term calculates maximum phytoplankton growth rate as an exponential function of temperature, T , and base growth rate at 0 °C (Eppley, 1972).

$$J_{Pn} = \frac{V_{Pn^T} \cdot \hat{\alpha}_{Pn} \cdot I}{(V_{Pn^T}^2 + \hat{\alpha}_{Pn}^2 \cdot I^2)^{1/2}} \quad (22)$$

Given the (chlorophyll-related) initial slope of the P – I curve and (temperature-related) maximum phytoplankton growth rate, this function calculates realised growth rate given local irradiance, I ($W m^{-2}$).

$$Q_{N,Pn} = \frac{N}{k_{N,Pn+N}} \quad (23)$$

$$Q_{Fe,Pn} = \frac{F}{k_{Fe,Pn+F}} \quad (24)$$

Nutrient limitation of phytoplankton growth is specified here via standard, hyperbolic Michaelis–Menten terms that use ambient nutrient concentrations and parameters for the concentration at which phytoplankton growth is half its theoretical maximum.

$$PP_{Pn} = J_{Pn} \cdot Q_{N,Pn} \cdot Q_{Fe,Pn} \quad (25)$$

Light- and nutrient-limitation factors are brought together in a multiplicative term that determines nutrient uptake and, via Redfield coupling, primary production. Yool et al. (2011) investigated the significance of an alternative Liebig law of the minimum scheme for multiple nutrient limitation, and use of this approach is permitted in MEDUSA-2.0 via a switch, `jliebig`.

2.3.2 Diatom limitation and growth

Diatom phytoplankton growth terms are identical to those of non-diatom phytoplankton. However, because of their obligate requirement for silicon, diatom growth is additionally coupled to the availability of this nutrient, and a submodel of silicon uptake and diatom growth is used to represent these processes (Mongin et al., 2006). This places constraints on growth and nutrient uptake based upon the Si : N ratio of the modelled diatom cells, but allows a degree of plasticity in this ratio depending upon ambient growth conditions.

$$\theta_{Pd}^{Chl} = \frac{Chl_{Pd} \cdot \xi}{Pd} \quad (26)$$

$$\hat{\alpha}_{Pd} = \alpha_{Pd} \cdot \theta_{Pd}^{Chl} \quad (27)$$

$$V_{Pd^T} = V_{Pd} \cdot 1.066^T \quad (28)$$

$$J_{Pd} = \frac{V_{Pd^T} \cdot \hat{\alpha}_{Pd} \cdot I}{(V_{Pd^T}^2 + \hat{\alpha}_{Pd}^2 \cdot I^2)^{1/2}} \quad (29)$$

$$Q_{N,Pd} = \frac{N}{k_{N,Pd} + N} \quad (30)$$

$$Q_{Si} = \frac{S}{k_{Si} + S} \quad (31)$$

$$Q_{Fe,Pd} = \frac{F}{k_{Fe,Pd} + F} \quad (32)$$

As noted above, the growth of diatom phytoplankton is additionally limited by the availability of the macronutrient silicic acid.

$$R_{Si:N} = \frac{Pd_{Si}}{Pd} \quad (33)$$

$$R_{N:Si} = \frac{Pd}{Pd_{Si}} \quad (34)$$

Silicon is largely used by diatom phytoplankton in the construction of their cell walls, or frustules, which can vary significantly in their ornamentation (e.g. spines, girdle bands; Martin-Jézéquel et al., 2000) depending upon silicon availability. As a result, model diatoms have a degree of plasticity in their requirement for silicon, necessitating a separate state variable, Pd_{Si} , and centred around the stoichiometric ratios, $R_{Si:N}$ and $R_{N:Si}$.

if $R_{Si:N} \leq R_{Si:N}^0$ then,

$$PP_{Pd} = 0 \quad (35)$$

else if $R_{Si:N}^0 < R_{Si:N} < (3 \cdot R_{Si:N}^0)$ then,

$$PP_{Pd} = (J_{Pd} \cdot Q_{N,Pd} \cdot Q_{Fe,Pd}) \cdot \left(U_{\infty} \cdot \frac{R_{Si:N} - R_{Si:N}^0}{R_{Si:N}} \right) \quad (36)$$

else if $R_{Si:N} \geq (3 \cdot R_{Si:N}^0)$ then,

$$PP_{Pd} = (J_{Pd} \cdot Q_{N,Pd} \cdot Q_{Fe,Pd}) \quad (37)$$

In the above equations, the uptake of nitrogen (and iron) by diatom cells, PP_{Pd} , is governed by the Si : N ratio. If this falls below a critical value, $R_{Si:N}^0$, diatom cells are unable to complete their cell division cycle and growth stops Martin-Jézéquel et al. (2000). At values above this minimum ratio growth is scaled by a factor of the Si : N ratio, and above 3 times this ratio, growth in diatom biomass is unimpeded.

if $R_{Si:N} < (3 \cdot R_{Si:N}^0)^{-1}$ then,

$$PP_{Pd_{Si}} = (J_{Pd} \cdot Q_{Si}) \quad (38)$$

else if $(3 \cdot R_{Si:N}^0)^{-1} \leq R_{Si:N} < (R_{Si:N}^0)^{-1}$ then,

**A description of
MEDUSA-2.0**

A. Yool et al.

Title Page

Abstract

Introduction

Conclusions

References

Tables

Figures

⏪

⏩

◀

▶

Back

Close

Full Screen / Esc

Printer-friendly Version

Interactive Discussion



A description of MEDUSA-2.0

A. Yool et al.

Title Page

Abstract

Introduction

Conclusions

References

Tables

Figures

◀

▶

◀

▶

Back

Close

Full Screen / Esc

Printer-friendly Version

Interactive Discussion



$$PP_{Pd_{Si}} = (J_{Pd} \cdot Q_{Si}) \cdot \left(U_{\infty} \cdot \frac{R_{N:Si} - R_{N:Si}^0}{R_{N:Si}} \right) \quad (39)$$

else if $R_{Si:N} \geq (R_{Si:N}^0)^{-1}$ then,

$$PP_{Pd_{Si}} = 0 \quad (40)$$

Silicon uptake, $PP_{Pd_{Si}}$, occurs at the maximum rate permitted by light and silicon availability whenever the Si : N ratio is below a critical threshold, $(3 \cdot R_{Si:N}^0)^{-1}$. Above this ratio, silicon uptake is linearly decreased to another threshold value, $(R_{Si:N}^0)^{-1}$, above which no silicon is taken up by diatom cells – though diatom biomass, Pd, can still increase (and, of course, alter the Si : N ratio).

2.3.3 Chlorophyll growth scaling factors

As noted already, both phytoplankton groups have separate chlorophyll state variables in addition to those of nitrogen biomass. These allow modelled phytoplankton to alter their chlorophyll content dynamically under different light regimes (e.g. in response to season and depth). The following terms for this processes are taken from Taylor et al. (1997).

$$R_{Pn} = \frac{\theta_{\max, Pn}^{Chl}}{\theta_{Pn}^{Chl}} \cdot \frac{PP_{Pn}}{\hat{a}_{Pn} \cdot I} \quad (41)$$

$$R_{Pd} = \frac{\theta_{\max, Pd}^{Chl}}{\theta_{Pd}^{Chl}} \cdot \frac{PP_{Pd}}{\hat{a}_{Pd} \cdot I} \quad (42)$$

2.3.4 Microzooplankton grazing

As part of the size-structuring of MEDUSA, microzooplankton graze on smaller non-diatom phytoplankton and on particles of slow-sinking detritus. The ingestion function

that balances the availability of these prey items with the preference microzooplankton have for them is drawn from the classic model of Fasham et al. (1990).

$$G\mu_X = \frac{g_\mu \cdot \rho_{\mu X} \cdot X^2 \cdot Z_\mu}{k_\mu^2 + \rho_{\mu Pn} \cdot Pn^2 + \rho_{\mu D} \cdot D^2} \quad (43)$$

where X is Pn or D

The above term is repeated for each separate prey item consumed by microzooplankton. The term is based around a sigmoid function in which the “substrate” is composed of the sum of the prey items scaled by the preference that microzooplankton have for them. It is assumed here that microzooplankton prefer non-diatom phytoplankton over detritus since they represent a higher quality food item.

$$IN_{Z\mu} = (1 - \phi) \cdot (G\mu_{Pn} + G\mu_D) \quad (44)$$

$$IC_{Z\mu} = (1 - \phi) \cdot (\theta_{Pn} \cdot G\mu_{Pn} + \theta_D \cdot G\mu_D) \quad (45)$$

Here, the separate quantities of nitrogen, $IN_{Z\mu}$, and carbon, $IC_{Z\mu}$, ingested by microzooplankton are summed. Parameter ϕ relates to grazing inefficiency, so-called “messy feeding”, that returns a fraction of the grazed material back to dissolved nutrient. For the material actually ingested, the resulting C : N ratio, $\theta_{F\mu}$, can be calculated.

$$\theta_{F\mu} = \frac{IC_{Z\mu}}{IN_{Z\mu}} \quad (46)$$

Since grazed material may have a different C : N ratio than that required for microzooplankton growth, the assimilation and metabolism submodel of Anderson and Pondaven (2003) is incorporated here to balance growth, excretion and respiration. The C : N ratio of ingested food calculated above is then compared to the ideal ratio preferred by microzooplankton, $\theta_{F\mu}^*$. This makes use of the C : N ratio of microzooplankton

Title Page

Abstract

Introduction

Conclusions

References

Tables

Figures

◀

▶

◀

▶

Back

Close

Full Screen / Esc

Printer-friendly Version

Interactive Discussion



biomass, $\theta_{Z\mu}$, the assimilation efficiencies of nitrogen, β_N , and carbon, β_C , as well as the carbon growth efficiency, k_C , of microzooplankton. Unlike in MEDUSA-1.0, where an implicit treatment of carbon required all C : N ratios to be identical, here $\theta_{Z\mu}$ adopts a lower value more consistent with that of zooplankton.

$$5 \quad \theta_{F\mu}^* = \frac{\beta_N \cdot \theta_{Z\mu}}{\beta_C \cdot k_C} \quad (47)$$

Either C or N limits production depending on whether $\theta_{F\mu}$ is greater or lower than $\theta_{F\mu}^*$, with any excess carbon respired, and any excess nitrogen excreted. Growth, $F_{Z\mu}$, respiration, $R_{Z\mu}$, and excretion, $E_{Z\mu}$, are calculated as follows.

10 if $\theta_{F\mu} > \theta_{F\mu}^*$ then N is limiting and ...

$$F_{Z\mu} = \beta_N \cdot I_{N_{Z\mu}} \quad (48)$$

$$E_{Z\mu} = 0 \quad (49)$$

$$R_{Z\mu} = (\beta_C \cdot I_{C_{Z\mu}}) - (\theta_{Z\mu} \cdot F_{Z\mu}) \quad (50)$$

else if $\theta_{F\mu} < \theta_{F\mu}^*$ then C is limiting and ...

$$15 \quad F_{Z\mu} = \frac{\beta_C \cdot k_C \cdot I_{C_{Z\mu}}}{\theta_{Z\mu}} \quad (51)$$

$$E_{Z\mu} = I_{C_{Z\mu}} \cdot \left(\frac{\beta_N}{\theta_{F\mu}} - \frac{\beta_C \cdot k_C}{\theta_{Z\mu}} \right) \quad (52)$$

$$R_{Z\mu} = (\beta_C \cdot I_{C_{Z\mu}}) - (\theta_{Z\mu} \cdot F_{Z\mu}) \quad (53)$$

20 Figure 3 of Yool et al. (2011) shows the relative partitioning of carbon and nitrogen grazed by zooplankton depending upon food C : N ratio. In MEDUSA-1.0, the flux of C produced by zooplankton respiration was simply diagnostic, since the biogeochemical cycle of C was not resolved. Here, the loss of C through respiration is explicitly balanced by an increase in DIC in Eq. (13).

A description of
MEDUSA-2.0

A. Yool et al.

Title Page

Abstract

Introduction

Conclusions

References

Tables

Figures

◀

▶

◀

▶

Back

Close

Full Screen / Esc

Printer-friendly Version

Interactive Discussion



2.3.5 Mesozooplankton grazing

Mesozooplankton grazing follows that of microzooplankton with the exception that mesozooplankton have a broader range of prey items. For simplicity, parameters ϕ , β_N , β_C , and k_C are identical to those used for microzooplankton.

$$5 \quad Gm_X = \frac{g_m \cdot \rho_{mX} \cdot X^2 \cdot Z_m}{k_m^2 + F_m} \quad (54)$$

where X is Pn, Pd, Z μ or D

$$F_m = (\rho_{mPn} \cdot Pn^2) + (\rho_{mPd} \cdot Pd^2) + (\rho_{mZ\mu} \cdot Z\mu^2) + (\rho_{mD} \cdot D^2) \quad (55)$$

$$Gm_{PdSi} = R_{Si} \cdot Gm_{Pd} \quad (56)$$

$$IN_{Zm} = (1 - \phi) \cdot (Gm_{Pd} + Gm_{Pn} + Gm_{Z\mu} + Gm_{Pd}) \quad (57)$$

$$10 \quad IC_{Zm} = (1 - \phi) \cdot ((\theta_{Pd} \cdot Gm_{Pd}) + (\theta_{Pn} \cdot Gm_{Pn}) + (\theta_{Z\mu} \cdot Gm_{Z\mu}) + (\theta_D \cdot Gm_D)) \quad (58)$$

$$\theta_{Fm} = \frac{IC_{Zm}}{IN_{Zm}} \quad (59)$$

$$\theta_{Fm}^* = \frac{\beta_N \cdot \theta_{Zm}}{\beta_C \cdot k_C} \quad (60)$$

if $\theta_{Fm} > \theta_{Fm}^*$ then N is limiting and ... ,

$$F_{Zm} = \beta_N \cdot IN_{Zm} \quad (61)$$

$$15 \quad E_{Zm} = 0 \quad (62)$$

$$R_{Zm} = (\beta_C \cdot IC_{Zm}) - (\theta_{Zm} \cdot F_{Zm}) \quad (63)$$

else if $\theta_{Fm} < \theta_{Fm}^*$ then C is limiting and ... ,

$$F_{Zm} = \frac{\beta_C \cdot k_C \cdot IC_{Zm}}{\theta_{Zm}} \quad (64)$$

$$E_{Zm} = IC_{Zm} \cdot \left(\frac{\beta_N}{\theta_{Fm}} - \frac{\beta_C \cdot k_C}{\theta_{Zm}} \right) \quad (65)$$

$$R_{Zm} = (\beta_C \cdot IC_{Zm}) - (\theta_{Zm} \cdot F_{Zm}) \quad (66)$$

2.3.6 Plankton loss terms

5 In addition to losses to grazing, all four living components of the plankton model incur smaller, secondary losses to other processes.

$$M1_{Pn} = \mu_{1,Pn} \cdot Pn \quad (67)$$

$$M1_{Pd} = \mu_{1,Pd} \cdot Pd \quad (68)$$

$$M1_{Pd_{Si}} = R_{Si} \cdot M1_{Pd} \quad (69)$$

$$10 \quad M1_{Z\mu} = \mu_{1,Z\mu} \cdot Z\mu \quad (70)$$

$$M1_{Zm} = \mu_{1,Zm} \cdot Zm \quad (71)$$

The above functions are density-independent loss terms for processes such as metabolism that occur without reference to abundance.

$$15 \quad M2_{Pn} = \mu_{2,Pn} \cdot \frac{Pn}{k_{Pn} + Pn} \cdot Pn \quad (72)$$

$$M2_{Pd} = \mu_{2,Pd} \cdot \frac{Pd}{k_{Pd} + Pd} \cdot Pd \quad (73)$$

$$M2_{Pd_{Si}} = R_{Si} \cdot M2_{Pd} \quad (74)$$

$$M2_{Z\mu} = \mu_{2,Z\mu} \cdot \frac{Z\mu}{k_{Z\mu} + Z\mu} \cdot Z\mu \quad (75)$$

$$20 \quad M2_{Zm} = \mu_{2,Zm} \cdot \frac{Zm}{k_{Zm} + Zm} \cdot Zm \quad (76)$$

The above functions are density-dependent loss terms for processes such as disease (e.g. viruses) and grazing by implicit higher trophic levels that occur at rates that depend

Title Page

Abstract

Introduction

Conclusions

References

Tables

Figures

◀

▶

◀

▶

Back

Close

Full Screen / Esc

Printer-friendly Version

Interactive Discussion



upon plankton abundance. By default, density-dependent losses are represented using a hyperbolic function of plankton concentration (Fasham, 1993), although switches in the model code (Table 6) permit linear, quadratic and sigmoid functions. As the best choice for mortality function is unclear but can have significant consequences for models (e.g. Steele and Henderson, 1992; Edwards and Yool, 2000; Anderson et al., 2010), Yool et al. (2011) investigated alternative functions for this mortality term. While the simplest form examined – linear mortality – had significant impacts on the behaviour of MEDUSA-1.0, the differences between simulations using quadratic, hyperbolic (as here) and sigmoid forms was much more minor, and MEDUSA-2.0 retains the same default as MEDUSA-1.0.

2.3.7 Miscellaneous losses

As silicic acid occurs at undersaturated concentrations throughout the modern ocean (Yool and Tyrrell, 2003), the silicon component of diatom phytoplankton is additionally vulnerable to dissolution. This is represented here by a simple linear loss rate (Mongin et al., 2006).

$$DS_{Pd_{Si}} = \text{Diss} \cdot Pd_{Si} \quad (77)$$

Remineralisation of slow-sinking detrital particles to dissolved inorganic pools occurs at rates dependent on ambient temperature.

$$M_D = \mu_D \cdot 1.066^T \cdot D \quad (78)$$

$$M_D = \mu_{Dc} \cdot 1.066^T \cdot D_C \quad (79)$$

2.3.8 Iron supply and removal

Following the submodel of Dutkiewicz et al. (2005), iron is added to the ocean by aeolian deposition of iron-carrying dust at the surface, and removed throughout its

Title Page

Abstract

Introduction

Conclusions

References

Tables

Figures

◀

▶

◀

▶

Back

Close

Full Screen / Esc

Printer-friendly Version

Interactive Discussion



volume by scavenging.

$$F_{\text{atmos}} = \text{spatially variable rate} \quad (80)$$

The field of iron desposition used in MEDUSA-1.0 has been updated for MEDUSA-2.0 to take advantage of a newer climatology, and now makes use of the “present-day” field produced by Mahowald (2005). Figure 2 shows a map of annual average iron deposition. However, as with MEDUSA-1.0, aeolian iron solubility was adjusted such that the total addition of dissolved iron to the open ocean by dust was the same as that of Dutkiewicz et al. (2005).

$$F_{\text{benthos}} = \text{spatially variable rate} \quad (81)$$

A further difference with MEDUSA-1.0 lies in the inclusion of a benthic source of dissolved iron. Such a supply route is already known for iron, most noticeably around islands and other areas of shallow water in regions that are otherwise depleted in iron (e.g. the Crozet Archipelago in the Southern Ocean; Pollard et al., 2009), and some existing models already include it (e.g. Moore et al., 2004). Here, a flux of iron is added to ocean cells immediately above the seafloor wherever the water column is shallower than 500 m. There is considerable uncertainty in the addition rate of iron to the ocean by this route (Moore et al., 2004), and here the rate has been chosen such that aeolian and benthic supply routes are of approximately similar magnitude.

$$F_{\text{free}} = F - F_{\text{ligand}} \quad (82)$$

MEDUSA’s iron state variable, F , represents total iron, and this is assumed to occur in two fractions: “free”, F_{free} ; and that bound to organic ligands, F_{ligand} (Gledhill and van den Berg, 1994). In the ocean, it is estimated that more than 97 % of total iron is complexed with ligands (Boye et al., 2003).

$$F_{\text{ligand}} = L_{\text{total}} - L_{\text{free}} \quad (83)$$

$$L_{\text{free}} = 0.5 \cdot \frac{(F_1 + \sqrt{F_2})}{k_{\text{FeL}}} \quad (84)$$

$$F_1 = k_{\text{FeL}} \cdot (L_{\text{total}} - F) - 1 \quad (85)$$

$$F_2 = \max(F_1^2 + (4 \cdot k_{\text{FeL}} \cdot L_{\text{total}}), 0) \quad (86)$$

5 The complexation reactions between iron species and ligands occur rapidly, and it is assumed here that they reach equilibrium in a shorter period than the model time-step (Rose and Waite, 2003). In the equations above, L_{total} is the total ligand concentration of seawater, and is assumed to be globally constant; k_{FeL} is the ligand binding strength. Given these equations and parameters, Fig. 2 illustrates the resulting partition between
10 “free” and bound iron over a range of total iron concentrations.

$$F_{\text{scavenge}} = k_{\text{scav}} \cdot F_{\text{free}} \quad (87)$$

Scavenging of iron occurs at a fixed linear rate, k_{scav} , throughout the full volume of the ocean, but is assumed to only remove “free” iron, F_{free} .

15 2.3.9 Fast detritus production

Sinking detrital material in MEDUSA-2.0 occurs in two forms:

- Small particles that are assumed to sink slowly and are modelled explicitly (as D and D_C); these particles remineralise at a temperature-dependent rate and are a food item of both micro- and mesozooplankton
- Large particles that are assumed to sink quickly and whose attenuation down the water column is modelled implicitly; these particles remineralise exponentially with depth and are not available as a food item

As in MEDUSA-1.0, fast-sinking detrital particles are remineralised down the water column using a variant of the so-called ballasting hypothesis (Armstrong et al., 2002).

**A description of
MEDUSA-2.0**

A. Yool et al.

Title Page

Abstract

Introduction

Conclusions

References

Tables

Figures

⏪

⏩

◀

▶

Back

Close

Full Screen / Esc

Printer-friendly Version

Interactive Discussion



This scheme posits a relationship between organic material and associated – and protective – biominerals. As the description in Yool et al. (2011) includes extensive treatment of the scheme used in MEDUSA-1.0, here we give a summary overview and focus on the differences in MEDUSA-2.0.

In the first instance, the components of fast-sinking detrital particles are produced by a series of ecosystem processes. Organic material (N, Fe, C) is derived from losses from diatoms and mesozooplankton, the larger components of the plankton. Note that, as with other processes, iron is again coupled to nitrogen via a fixed Fe : N ratio.

$$T_N(k+1) = T_N(k) + ((D1_{\text{frac}} \cdot M2_{\text{Pd}}) + (D2_{\text{frac}} \cdot M2_{\text{Zm}})) \cdot \delta z(k) \quad (88)$$

$$T_{\text{Fe}}(k+1) = T_{\text{Fe}}(k) + ((R_{\text{Fe}} \cdot D1_{\text{frac}} \cdot M2_{\text{Pd}}) + (R_{\text{Fe}} \cdot D2_{\text{frac}} \cdot M2_{\text{Zm}})) \cdot \delta z(k) \quad (89)$$

$$T_C(k+1) = T_C(k) + ((\theta_{\text{Pd}} \cdot D1_{\text{frac}} \cdot M2_{\text{Pd}}) + (\theta_{\text{Zm}} \cdot D2_{\text{frac}} \cdot M2_{\text{Zm}})) \cdot \delta z(k) \quad (90)$$

Inorganic biogenic opal (Si) is derived directly (via cell mortality) or indirectly (as a product of mesozooplankton grazing) from diatom phytoplankton. In MEDUSA-1.0, the fraction of grazed opal that became associated with fast-sinking detritus was the same as the fraction of mesozooplankton losses that were similarly channelled, $D2_{\text{frac}}$. Here, a new parameter, $D3_{\text{frac}}$, has been introduced to allow the separate specification of this transfer efficiency.

$$T_{\text{Si}}(k+1) = T_{\text{Si}}(k) + ((D1_{\text{frac}} \cdot M2_{\text{PdSi}}) + (D3_{\text{frac}} \cdot Gm_{\text{PdSi}})) \cdot \delta z(k) \quad (91)$$

Calcium carbonate, CaCO_3 , is also an important biomineral in the ballast hypothesis, but its production is not modelled explicitly in either version of MEDUSA. This decision to omit calcification in MEDUSA stems from the diversity (phylogenetic and trophic) of organisms that manufacture CaCO_3 and the uncertainty in the ecological factors that regulate it, as is evidenced by the wide range of approaches used to model it (e.g. Tyrrell and Taylor, 1996; Moore et al., 2002; Gehlen et al., 2007; Zahariev et al., 2008; Yool et al., 2010). Instead, MEDUSA adopts an empirical approach in which the only calcification explicitly considered is that associated with sinking material; CaCO_3

A description of
MEDUSA-2.0

A. Yool et al.

Title Page

Abstract

Introduction

Conclusions

References

Tables

Figures

◀

▶

◀

▶

Back

Close

Full Screen / Esc

Printer-friendly Version

Interactive Discussion



that is synthesised and dissolved without significant vertical movement is considered tangential.

$$T_{\text{CaCO}_3}(k+1) = T_{\text{CaCO}_3}(k) + ((\theta_{\text{Pd}} \cdot D1_{\text{frac}} \cdot M2_{\text{Pd}}) + (\theta_{\text{Zm}} \cdot D2_{\text{frac}} \cdot M2_{\text{Zm}})) \cdot \delta Z(k) \cdot \text{fo}(\Omega_{\text{calcite}}) \quad (92)$$

Following Dunne et al. (2007), MEDUSA-1.0 used a simple function of latitude, $fc(lat)$, to calculate the relative quantity of CaCO_3 associated with fast-sinking detrital particles, the so-called “rain ratio”. MEDUSA-2.0 retains this functionality as an option, but introduces a further option that instead calculates associated CaCO_3 as a function, $\text{fo}(\Omega_{\text{calcite}})$, of the ambient saturation state of the CaCO_3 polymorph calcite.

$$\text{fo}(\Omega_{\text{calcite}}) = (\Omega_{\text{calcite}} - 1)^\eta \cdot r_0 \quad (93)$$

This is based on the formulation of Ridgwell et al. (2007), and uses the concentrations of calcium (seawater average) and carbonate (calculated from DIC) ions to calculate Ω_{calcite} . Options exist in MEDUSA-2.0 for the rain ratio to be based on Ω_{calcite} at the ocean surface or at the local position within its interior (via switch `jrratio`; see Table 6). Parameter r_0 has been scaled in MEDUSA-2.0 so that total production of CaCO_3 using Eq. (93) approximately matches that in MEDUSA-1.0 (see later). Note that in the real ocean a second polymorph of CaCO_3 is also produced, aragonite, but for simplicity calculations are performed as if all CaCO_3 in MEDUSA-2.0 is the more stable polymorph, calcite (though the saturation state of aragonite, $\Omega_{\text{aragonite}}$, is calculated as a diagnostic variable).

2.3.10 Fast detritus remineralisation

The ballast hypothesis of Armstrong et al. (2002) posits that a fraction of the sinking organic material is quantitatively associated with sinking inorganic material (here calcium carbonate and biogenic silica), and that this provides “protection” for the organic matter, allowing it to penetrate deeper into the water column than might otherwise be

A description of MEDUSA-2.0

A. Yool et al.

Title Page

Abstract

Introduction

Conclusions

References

Tables

Figures

◀

▶

◀

▶

Back

Close

Full Screen / Esc

Printer-friendly Version

Interactive Discussion



expected. Follow-up work by Klaas and Archer (2002) derived a parameterisation of the hypothesis based on a global dataset of sediment trap measurements, and this latter study has subsequently been used as the basis for other work. Its implementation by Dunne et al. (2007) was that adopted by MEDUSA-1.0, and this has been retained by MEDUSA-2.0.

By way of summary, the fast detrital flux of organic carbon is proportioned into “protected”, $TC_{\text{protect}} = (TC_{\text{bSi}} + TC_{\text{bCaCO}_3})$, and “excess”, TC_{excess} , portions as follows.

$$TC_{\text{bSi}} = T_{\text{Si}}(k) \cdot \frac{M_{\text{Si}}}{M_{\text{org}}} \cdot f_{\text{Si}} \quad (94)$$

$$TC_{\text{bCaCO}_3} = T_{\text{CaCO}_3}(k) \cdot \frac{M_{\text{CaCO}_3}}{M_{\text{org}}} \cdot f_{\text{CaCO}_3} \quad (95)$$

$$TC_{\text{protect}} = (TC_{\text{bSi}} + TC_{\text{bCa}}) \quad (96)$$

$$TC_{\text{excess}} = T_C(k) - TC_{\text{protect}} \quad (97)$$

Where M_{Si} and M_{CaCO_3} convert molar silicon and calcium carbonate ballast into mass equivalents that can then be used with mass-based organic carbon protection ratios f_{Si} and f_{CaCO_3} . The “protected” fraction passes through unscathed to the next level down the water column, while the “excess” fraction is attenuated across a particular level, with a corresponding release of inorganic carbon. Not all “excess” carbon is remineralised in a given level, and the surviving portion, TC_{survive} , is calculated as follows.

$$TC_{\text{survive}} = TC_{\text{excess}} \cdot \exp\left(-\frac{\delta z(k)}{d_{\text{excess}}}\right) \quad (98)$$

Leaving aside that added through production (see Eq. 90), the quantity of fast detritus reaching the next model layer, $T_C(k+1)$, is then as follows.

$$T_C(k+1) = TC_{\text{protect}} + TC_{\text{survive}} \quad (99)$$

A description of
MEDUSA-2.0

A. Yool et al.

Title Page

Abstract

Introduction

Conclusions

References

Tables

Figures

◀

▶

◀

▶

Back

Close

Full Screen / Esc

Printer-friendly Version

Interactive Discussion



A description of
MEDUSA-2.0

A. Yool et al.

Title Page

Abstract

Introduction

Conclusions

References

Tables

Figures

◀

▶

◀

▶

Back

Close

Full Screen / Esc

Printer-friendly Version

Interactive Discussion



The flux of remineralised carbon to level k is then simply:

$$LD_C(k) = \frac{TC_{\text{excess}} - TC_{\text{survive}}}{\delta z(k)} \quad (100)$$

The remineralisation fluxes of nitrogen and iron follow that of carbon, with the same fraction of sinking material “protected” by ballasting minerals. By contrast, the sinking fluxes of both biogenic silica, $T_{\text{Si}}(k)$, and calcium carbonate, $T_{\text{CaCO}_3}(k)$, attenuate with depth independently of organic carbon.

In the case of biogenic silica, this attenuation occurs at all depths because it is globally undersaturated with respect to ambient silicic acid concentrations. The equations governing sinking biogenic silic and its dissolution are as follows:

$$T_{\text{Si}}(k+1) = T_{\text{Si}}(k) \cdot \exp\left(-\frac{\delta z(k)}{d_{\text{Si}}}\right) \quad (101)$$

$$LD_{\text{Si}}(k) = \frac{T_{\text{Si}}(k) - T_{\text{Si}}(k+1)}{\delta z(k)} \quad (102)$$

Unlike biogenic silica, CaCO_3 is generally not soluble in surface waters because of supersaturating concentrations of the carbonate ion. However, at depth, specifically below the lysocline, concentrations become undersaturating and dissolution can occur.

if $z(k) < \text{lysocline}(\text{lat}, \text{lon})$

$$T_{\text{CaCO}_3}(k+1) = T_{\text{CaCO}_3}(k) \cdot \exp\left(-\frac{\delta z(k)}{d_{\text{CaCO}_3}}\right) \quad (103)$$

else

$$T_{\text{CaCO}_3}(k+1) = T_{\text{CaCO}_3}(k) \quad (104)$$

In MEDUSA-1.0, the depth of the lysocline, $\text{lysocline}(\text{lat}, \text{lon})$, was precalculated using physical and biogeochemical fields from the World Ocean Atlas and GLODAP climatologies (Locarnini et al., 2010; Antonov et al., 2010; Key et al., 2004). Here, the

inclusion of DIC and alkalinity, as well as a carbonate chemistry submodel, allows MEDUSA-2.0 to calculate the saturation state of CO_3^{2-} at all depths, and to use this to determine the point in each water column at which biogenic CaCO_3 will begin to dissolve. The dissolution flux calcium carbonate is then simply:

$$LD_{\text{CaCO}_3}(k) = \frac{T_{\text{CaCO}_3}(k) - T_{\text{CaCO}_3}(k+1)}{\delta z(k)} \quad (105)$$

Figure 3 shows a comparison of the observationally-based lysocline of MEDUSA-1.0 with that simulated by MEDUSA-2.0 for the 1990s (which corresponds to GLODAP's "present-day"). While the two maps agree well in regions such as the Atlantic, they also differ, most noticeably in the Pacific, where there are both shallower and deeper areas. The largest regional discrepancy lies in the Southern Ocean, where MEDUSA-2.0 has an average CCD depth of 3393 m compared to 2934 m. However, at the global scale, MEDUSA-1.0 has an average CCD depth of 2734 m, and MEDUSA-2.0 is slightly deeper at 2779 m.

Separate from the ballast model, MEDUSA-2.0 includes a code switch, `jexport`, to permit the use of two alternative remineralisation schemes for the organic components of fast-sinking detritus: the classic Martin et al. (1987) curve; and the variant developed by Henson et al. (2012). Both models attenuate organic material using the same power relationship shown below:

$$F_C(z) = F_C(100) \cdot \left(\frac{z}{100}\right)^b \quad (106)$$

Parameterised using the limited data that was available at the time, the Martin et al. (1987) curve uses a fixed value of -0.858 for parameter b in Eq. (106). Using a more modern dataset of thorium-derived POC export, Henson et al. (2012) developed a variant scheme in which parameter b is instead a function of local surface temperature:

$$b = -1.06 + (0.024 \cdot T) \quad (107)$$

Title Page

Abstract

Introduction

Conclusions

References

Tables

Figures

◀

▶

◀

▶

Back

Close

Full Screen / Esc

Printer-friendly Version

Interactive Discussion



In the work described here, only the ballast scheme is formally used, though the significance of these (and, potentially, other) schemes will be the subject of future work.

2.3.11 Air–sea gas exchange

MEDUSA-2.0 includes gas exchange for two modelled constituents, O₂ and CO₂. In the case of O₂, the scheme developed by Najjar and Orr (1999) for the OCMIP–2 project is used. In this, the saturation concentration of O₂ is calculated based on local temperature and salinity, and this is used in conjunction with ocean surface O₂ concentration and wind speed (via standard gas transfer calculations) to calculate air–sea exchange.

The case of CO₂ is complicated by the intricacies of carbonate chemistry, which necessitates the iterative calculation of surface ocean pH to determine surface H₂CO₃ concentration. As with O₂, this is then combined with atmospheric *p*CO₂ and wind speed to calculate the air–sea exchange of CO₂. The numerical scheme used here is that published by Blackford et al. (2007) (and utilised in Artoli et al., 2012). Alongside air–sea exchange, this scheme calculates other carbonate chemistry properties that are utilised by MEDUSA-2.0, such as Ω_{calcite} . It also permits the calculation of all these properties at arbitrary depths down the water column, and is used in MEDUSA-2.0 to determine the location of the CCD.

Surface gas exchange calculations are performed at every model timestep. Carbonate chemistry calculations are only performed for the full water column on a monthly timescale to reduce computational burden.

2.3.12 Miscellaneous

In MEDUSA-1.0, the same Redfield C : N ratio of 6.625 was assumed for both phytoplankton and zooplankton so that the pool of detritus was fed C and N at the same ratio regardless of the source. With the inclusion of a separate detrital carbon pool, D_C, these ratios no longer need to be identical, and both micro- and mesozooplankton are assumed to have a lower C : N ratio, 5.625 (Anderson and Pondaven, 2003).

A description of MEDUSA-2.0

A. Yool et al.

Title Page

Abstract

Introduction

Conclusions

References

Tables

Figures

◀

▶

◀

▶

Back

Close

Full Screen / Esc

Printer-friendly Version

Interactive Discussion



shallower remineralisation and near-surface nutrient retention. Reflecting the addition of the carbon cycle, the assimilation efficiencies of both zooplankton types are now specified separately for the nitrogen (0.77) and carbon (0.64) ingested during grazing (from MEDUSA-1.0's common value of 0.69; Anderson and Pondaven, 2003). New parameters include a separate remineralisation rate for detrital carbon, a series of oxygen stoichiometry parameters, a minimum concentration for dissolved oxygen consumption, and a series of remineralisation/dissolution rate parameters for the benthic reservoirs.

In addition to the parameters above, MEDUSA-2.0 includes a number of control parameters that allow the model to switch between different functional forms for a small number of processes. These appear in `namelist.trc.sms` and are listed in Table 6. As noted above, the control parameters available in MEDUSA-1.0 have been augmented by several new options including export submodel, `jexport`, rain ratio calculation, `jrratio` and CCD calculation, `jocalccd`.

3 Default simulation

The following section describes a simulation and evaluation of MEDUSA-2.0 using the default equations, functional forms and parameter values described previously. Evaluation is performed against observational data, but also with MEDUSA-1.0 itself.

Both NEMO and MEDUSA-2.0 were initialised at the time-point of midnight on the 1st of January 1860. This is a standard point in HadGEM2-ES simulations for CMIP5. The model was then run out to the 30th of December 2005. Note that this is the final day of the year in the 360 day calendar of the atmospheric forcing used here.

3.1 Physical model

The underlying physical model used in this simulation is version 3.2 of NEMO (Madec, 2008). This is comprised of an ocean general circulation model, OPA9 (Madec et al., 1998; Madec, 2008), coupled with a sea-ice model, Louvain-la-Neuve Ice Model ver-

A description of MEDUSA-2.0

A. Yool et al.

Title Page

Abstract

Introduction

Conclusions

References

Tables

Figures

◀

▶

◀

▶

Back

Close

Full Screen / Esc

Printer-friendly Version

Interactive Discussion



A description of MEDUSA-2.0

A. Yool et al.

Title Page

Abstract

Introduction

Conclusions

References

Tables

Figures

◀

▶

◀

▶

Back

Close

Full Screen / Esc

Printer-friendly Version

Interactive Discussion



sion 2 (LIM2; Timmermann et al., 2005). This physical framework is configured at approximately $1^\circ \times 1^\circ$ horizontal resolution (292×362 grid points), with a focusing of resolution around the equator to improve the representation of equatorial upwelling. Vertical space is divided into 64 levels, which increase in thickness with depth, from approximately 6 m at the surface to 250 m at 6000 m. To improve the representation of deep water circulation, partial level thicknesses are used in the specification of bottom topography. Vertical mixing is parameterised using the turbulent kinetic energy (TKE) scheme of Gaspar et al. (1990), with modifications by Madec (2008).

The sea-ice submodel used here, LIM2, is based upon viscous-plastic ice rheology (Hibler, 1979) and three layer (two layers of sea-ice, one layer of snow) thermodynamics (Semtner, 1976), with a number of updated physical processes (see Timmermann et al., 2005; and references therein). Model sea-ice is coupled to the ocean every 5 ocean timesteps through the non-linear quadratic drag law of the shear between sea-ice and ocean surface velocity (Timmermann et al., 2005). Freshwater exchange between the ocean and sea-ice is calculated from precipitation and ice formation/melting (Fichefet and Morales Maqueda, 1997), where sea-ice salinity is assumed to be 4 psu and rain/snow are assumed fresh. The heat flux between the sea-ice and ocean is proportional to the departure in temperature from salinity-dependent freezing point and the friction velocity at the ice-ocean interface. Solar radiation can penetrate sea-ice not covered by snow, and is dissipated by brine pockets within the ice where it increases latent heat storage (Fichefet and Morales Maqueda, 1997).

In Yool et al. (2011), NEMO was forced at the ocean surface for the period 1966–2005 using DFS4.1 fields developed by the European DRAKKAR collaboration (DRAKKAR Group, 2007). As MEDUSA-2.0 includes the ocean’s carbon cycle, and since this is currently undergoing secular change driven by increasing atmospheric concentrations of CO_2 , simulations running over a longer period of time are necessary. There are a number of approaches to achieve this including, for instance, the use of a climatological average or “normal year” (e.g. Najjar et al., 2007), or the repeated cycling of historical forcing (e.g. Yool et al., 2010). These have the advantage of using

A description of MEDUSA-2.0

A. Yool et al.

Title Page

Abstract

Introduction

Conclusions

References

Tables

Figures

◀

▶

◀

▶

Back

Close

Full Screen / Esc

Printer-friendly Version

Interactive Discussion



actual observationally-derived forcing, but also assume that the recent past from which they are derived is representative of earlier periods of time (in spite of ongoing climate change). An alternative approach is to utilise forcing derived from either atmospheric models or coupled ocean–atmosphere models. These are routinely run in long duration simulations that span pre-industrial or pre–20th century periods when there was comparatively little change in climate or the carbon cycle. They also offer the opportunity to forecast biogeochemical cycles into the future with a significantly different climate from that of the present-day.

Here, NEMO is forced following this latter approach, using output from a simulation of the HadGEM2-ES Earth system model run by the UK Meteorological Office (UKMO). HadGEM2-ES is a development of the physical climate model, HadGEM1 (Johns et al., 2006), that includes representations of the terrestrial and oceanic carbon cycles, atmospheric chemistry and aerosols (Collins et al., 2011). The HadGEM2-ES simulation used here, identifier AJKKH, was performed as part of the UKMO’s input Jones et al. (2011) to the Coupled Model Intercomparison Project 5 (CMIP5) and Assessment Report 5 (AR5) of the Intergovernmental Panel on Climate Change (IPCC). Operationally, HadGEM2-ES output was processed into the same forcing fields as that provided by the DFS4.1 forcing previously used with MEDUSA-1.0. The frequency of the output fields also matched that of DFS4.1, namely monthly for precipitation (rain, snow, runoff), daily for radiation (downwelling short- and long-wave) and 6-hourly for the turbulent variables (air temperature, humidity and wind velocities). Note that the reference height of forcing in HadGEM2-ES differs from that of DFS4.1, but that NEMO’s bulk formulae allow this height to readily be changed to accommodate HadGEM2-ES.

For maximum congruence with the surface forcing, temperature and salinity fields are initialised here using output from HadGEM2-ES valid for the same time as the forcing. To prevent excessive drift, sea surface salinity (SSS) is relaxed towards that derived from HadGEM2-ES. Unlike simulations under DFS4.1, where an invariant monthly mean climatology of SSS values is used, here the SSS target consists of a monthly time-series running across the forcing period. The relaxation timescale is approxi-

mately 30 days for the open ocean, and 12 days under sea-ice. The freshwater budget is also monitored for imbalances between integrated downward and upward fluxes, and a correction term applied between years (i.e. an imbalance in year X is corrected for in year X + 1).

Further details concerning physical model configuration can be found in Barnier et al. (2006), Penduff et al. (2007) and Penduff et al. (2010), but note that these describe higher resolution instances of NEMO.

3.2 Biogeochemistry

MEDUSA-2.0's fields of DIN, silicic acid and oxygen were initialised using January values from the World Ocean Atlas 2009 (Garcia et al., 2010a,b). Similarly to MEDUSA-1.0, total iron was initialised using an iron field derived from a long-duration simulation of a lower resolution GCM (Parekh et al., 2005; Dutkiewicz et al., 2005). DIC and alkalinity were initialised using a modified form of the GLODAP climatology (Key et al., 2004). It was assumed that GLODAP's pre-industrial DIC field is approximately valid for the 1860 start of this simulation, though this approach has known issues concerning the ocean's anthropogenic CO₂ inventory in 1860 (e.g. Yool et al., 2010).

The GLODAP fields used here required modification to account for large regional lacunae including the Arctic Ocean, the Caribbean Sea, the Mediterranean Sea and the Malay Archipelago. These were filled through an approach utilising multiple linear regression (MLR) together with the more complete WOA 2009 fields of temperature (Locarnini et al., 2010), salinity (Antonov et al., 2010), DIN, phosphate, silicic acid and oxygen. For each missing region, values of these tracers in immediately adjacent areas were used to construct a unique MLR. The calculated MLR was then used to fill the lacuna using field values from the WOA 2009. As biogeochemical tracers frequently show strong vertical gradients, separate MLRs were constructed for a series of intervals down the water column (0–50, 50–100, 100–200, 200–500, 500–1000, 1000–2000, below 2000 m). This procedure was used first with alkalinity, and then the resulting alkalinity field was added to the list of input fields for the construction of MLRs to fill

A description of MEDUSA-2.0

A. Yool et al.

Title Page

Abstract

Introduction

Conclusions

References

Tables

Figures

◀

▶

◀

▶

Back

Close

Full Screen / Esc

Printer-friendly Version

Interactive Discussion



DIC lacunae. While extrapolating in this fashion is likely to introduce some spurious values, particularly where WOA 2009 fields are already uncertain (e.g. the Arctic Ocean), it resulted in fields of DIC and alkalinity that appeared more credible than extrapolation by simple floodfilling was able to achieve.

All other model tracers (plankton and detritus) were initialised to arbitrary small values. Benthic reservoirs of nutrients, carbon and CaCO_3 were set to zero. Note that, unlike in MEDUSA-1.0, no coastal relaxation fluxes were applied to nutrients (N, Si) in MEDUSA-2.0. This change reflects both the switch to forcing periods outside the “present day”, and the finding in Yool et al. (2011) that this relaxation scheme did not universally emulate the riverine addition of nutrients as originally intended.

3.3 Results

In this section, a selection of model results are presented with the aim of providing an overview of MEDUSA-2.0’s performance. In the first instance, model outputs that can be compared to observational fields are presented. These are followed by Taylor diagrams that aim to provide a quantitative evaluation of performance (cf. space and time). Next, model fields of interesting but unmeasured (or unmeasurable) properties are shown to illuminate notable aspects of MEDUSA-2.0. Finally, some plots of the time-evolution of MEDUSA-2.0 are shown to illustrate the model’s stability and drift. This format of presentation and analysis is repetitive of that for MEDUSA-1.0 as described in Yool et al. (2011). However, since the simulation of MEDUSA-2.0 here is of considerably longer duration than than analysed for MEDUSA-1.0 (146 yr versus 41 yr), the results are of particular interest because they permit evaluation of the model’s longer-term behaviour and stability.

Observational fields used in comparison with MEDUSA-2.0 are comprised of WOA 2009 nutrients (Garcia et al., 2010b), SeaWiFS chlorophyll (O’Reilly et al., 1998), estimated primary production (Behrenfeld and Falkowski, 1997; Carr et al., 2006; Westberry et al., 2008), GLODAP carbon and alkalinity (Key et al., 2004) and air–sea CO_2 exchange (Takahashi et al., 2009). Because of its biogeochemical importance, and the

A description of MEDUSA-2.0

A. Yool et al.

Title Page

Abstract

Introduction

Conclusions

References

Tables

Figures

◀

▶

◀

▶

Back

Close

Full Screen / Esc

Printer-friendly Version

Interactive Discussion



diversity in estimates of it, observational primary production is drawn here from three empirical models: VGPM (Behrenfeld and Falkowski, 1997); Eppley-VGPM (Carr et al., 2006); and CbPM (Westberry et al., 2008). The observational fields of chlorophyll and productivity used here represent averages over the same 5 yr period from 2000 to 2004 inclusive, and this same period is used throughout the following analysis as a standard interval except where noted.

In passing, note that where geographical plots are shown, the Mollweide equal area projection has been used in order that ocean regions are presented without undue emphasis.

Figures 4 and 5 compare MEDUSA-2.0's performance in representing, respectively, surface concentrations of the macronutrients DIN and silicic acid. In the case of DIN, MEDUSA-2.0 shows generally good agreement in the Northern Hemisphere, but with noticeably higher concentrations in both equatorial upwelling regions and in the Southern Ocean. A similarly strong Southern Ocean bias was found with MEDUSA-1.0, though equatorial waters there showed a slight bias in the opposite direction. Silicic acid concentrations are very similar between both MEDUSA versions, and show very the same patterns of bias. Most noticeably, markedly elevated Southern Ocean concentrations, uniformly too-low equatorial concentrations, and concentrations in the Northern Pacific lower than those observed in this HNLC region. Figures 6 and 7 show corresponding, basin-averaged Hovmöller diagrams of DIN and silicic acid for the Atlantic and Pacific Oceans.

Focusing on the deep ocean, Figs. 8 and 9 show zonally averaged sections of DIN and silicic acid down the Atlantic and Pacific basins (the Atlantic includes the Arctic Ocean; both basin sections include the Southern Ocean). In both cases, most large-scale structure has persisted in MEDUSA-2.0 across the run duration. However, there are some important differences, of which the Southern Ocean is the most extreme. In this region, excessive ventilation acts to homogenise horizontal and vertical gradients, most noticeably those of silicic acid. A similar problem in the Southern Ocean was

A description of MEDUSA-2.0

A. Yool et al.

Title Page

Abstract

Introduction

Conclusions

References

Tables

Figures

◀

▶

◀

▶

Back

Close

Full Screen / Esc

Printer-friendly Version

Interactive Discussion



noted by Yool et al. (2011) and ascribed to a deficiency in NEMO, but the problem here is somewhat worse and that this may stem from the change in surface forcing.

An examination of the large-scale circulation of the run finds that the Antarctic Circumpolar Current (ACC) is significantly stronger (220 Sv) in this simulation compared to that used with MEDUSA-1.0 (160 Sv), and toward the high end of other models (CMIP5 range of 90–264 Sv; Meijers et al., 2012). This is associated with stronger Antarctic Bottom Water (AABW) formation around Antarctica, and leads to enhanced ventilation of the deep Atlantic and Pacific basins. In turn, this tends to erode deep gradients in nutrients that can be seen in the WOA (2009) panels of Figs. 8 and 9 but which are much weaker in the corresponding MEDUSA-2.0 panels. This enhanced ventilation is even clearer in the case of dissolved oxygen, Fig. 10, where strong vertical gradients in the Southern Ocean are strongly eroded in MEDUSA-2.0 (similarly for DIC and alkalinity; results not shown). However, as noted above, much of the zonal structure in the rest of the World Ocean is maintained, even in the case of dissolved oxygen. So while an improved circulation state would certainly be preferred, the impacts for MEDUSA-2.0 of NEMO’s “robust” Southern Ocean ventilation are somewhat restricted.

Returning to the surface ocean, Figs. 11 and 12 compare MEDUSA-2.0’s simulated total chlorophyll (non-diatom plus diatom) to corresponding SeaWiFS fields (note that a logarithmic colour scale is used to best represent the large range in ocean colour). Not uncommonly for ocean models, and similarly to MEDUSA-1.0, the representation of chlorophyll exhibits significant discrepancies with observations. MEDUSA-2.0 shows much less pronounced seasonality, particularly at higher latitudes in the Northern Hemisphere, and spatial boundaries that are significantly more sharply defined and consistently lower “background” chlorophyll concentrations in the ocean gyres. While the latter regions are not productive areas of the ocean, they represent a significant fraction of its total area. This was also noted with MEDUSA-1.0, and speculatively attributed to the assumption of geographically invariant nutrient kinetics. This prevents model phytoplankton from adapting to oligotrophic conditions when, in the real world, nutrient uptake kinetics are more plastic (e.g. Smith et al., 2009). However, given the

A description of
MEDUSA-2.0

A. Yool et al.

Title Page

Abstract

Introduction

Conclusions

References

Tables

Figures

◀

▶

◀

▶

Back

Close

Full Screen / Esc

Printer-friendly Version

Interactive Discussion



globally-uniform parameterisation of ecosystem actors in MEDUSA, it may be difficult to resolve this deficiency without more fundamental changes to the model framework. For instance, the addition of further phytoplankton types with parameter values more “at home” in oligotroph conditions.

5 Figures 13 and 14 compare MEDUSA’s simulated total primary production (non-diatom plus diatom) to a simplified average of the estimates of the VGPM, Eppley-VGPM and CbPM models. The average estimated production has been used here both to simplify intercomparison and because the separate estimates disagree significantly with one another (despite sharing inputs). In broad terms, MEDUSA-2.0 captures some of the spatial and seasonal patterns in productivity, though it does show significant systematic differences as well. These include: consistently low subtropical gyre productivity; elevated productivity in iron-limited regions including the Southern Ocean, equatorial Pacific and (seasonally) North Pacific; and a weaker bloom across the North Atlantic. In terms of total oceanic primary production, MEDUSA-2.0 predicts 10 41.6 GtCyr⁻¹, a value slightly below the bottom of the broad range of the observational estimates, 58.8, 60.4 and 46.3 GtCyr⁻¹ respectively (and below that of MEDUSA-1.0; 15 45.3 GtCyr⁻¹).

Figures 15 to 18 show the corresponding model-observation comparisons using Taylor diagrams. These illustrate both the correlation between (circumference axis) and relative variability (radial axis) of model and observations. For each comparison two plots are shown. The first uses annually average fields, but separates the analysis between major ocean regions; the second uses globally average fields, but separates the analysis between months. In all cases, model-observation is greater the closer plotted data are to the red/black bullseye on the horizontal axis.

25 Similarly to MEDUSA-1.0, the best agreement occurs with nutrient fields, particularly DIN. While there remains significant scatter, MEDUSA-2.0 generally shows good correlation with World Ocean Atlas 2009 fields, and comparable magnitudes of variability. In the case of surface silicic acid, there is considerable variability between basins with the Pacific performing very poorly, and the Indian exhibiting significantly elevated

A description of MEDUSA-2.0

A. Yool et al.

Title Page

Abstract

Introduction

Conclusions

References

Tables

Figures

◀

▶

◀

▶

Back

Close

Full Screen / Esc

Printer-friendly Version

Interactive Discussion



**A description of
MEDUSA-2.0**

A. Yool et al.

[Title Page](#)[Abstract](#)[Introduction](#)[Conclusions](#)[References](#)[Tables](#)[Figures](#)[◀](#)[▶](#)[◀](#)[▶](#)[Back](#)[Close](#)[Full Screen / Esc](#)[Printer-friendly Version](#)[Interactive Discussion](#)

variability. Much as with MEDUSA-1.0, agreement is still very weak in the case of chlorophyll, where the model both correlates poorly and shows much less variability than the observed SeaWiFS fields. Although estimated productivity is based on the same SeaWiFS chlorophyll fields, MEDUSA-2.0's agreement with the three productivity models is actually much greater, particularly the VGPM and CbPM models (results not shown), although correlations are still relatively weak.

Extending beyond MEDUSA-1.0, Figs. 19 to 22 compare MEDUSA-2.0 to observationally-derived fields of $\Delta p\text{CO}_2$ and air–sea CO_2 flux for year 2000 (Takahashi et al., 2009). The former is simply the localised difference between surface ocean $p\text{CO}_2$ and that of the atmosphere (assumed a globally uniform but time-varying quantity in the model). The latter is an estimate of the actual net exchange of CO_2 between the ocean and the atmosphere (where +ve values indicate net air-to-sea flux), based on $\Delta p\text{CO}_2$, air pressure, piston velocity and sea-ice concentration.

With $\Delta p\text{CO}_2$, MEDUSA-2.0 generally shows similar geographical patterns of excess or deficit. MEDUSA-2.0 tends to show somewhat exaggerated patterns with regions such as the northwest Pacific showing a stronger winter deficit, and others such as the Pacific upwelling showing a much stronger year-round excess. In contrast, and as Fig. 20 more clearly shows, MEDUSA-2.0 shows much weaker seasonality in the Southern Ocean, where estimated summer deficits and winter excesses are not well represented. Switching to Figs. 21 and 22, and the actual air–sea exchange of CO_2 , the situation is somewhat improved with MEDUSA-2.0's flux magnitudes more in agreement with those estimated. There are still, however, problems in the Southern Ocean, where the model misses periods of strong in- and out-gassing at the most southerly latitudes. Globally-integrated, MEDUSA-2.0 estimates a net air–sea flux of 1.35 GtCyr^{-1} compared to Takahashi et al. (2009)'s estimate of 1.42 GtCyr^{-1} . Note that Takahashi et al. (2009) believe that this direct estimate is probably an underestimate because of undersampling (which they suggest would increase it to 1.6 GtCyr^{-1}).

Switching to ecosystem properties for which observations are less synoptic, Figs. 23 to 30 show seasonal and geographical plots for a range of model fields.

A description of MEDUSA-2.0

A. Yool et al.

Title Page

Abstract

Introduction

Conclusions

References

Tables

Figures

◀

▶

◀

▶

Back

Close

Full Screen / Esc

Printer-friendly Version

Interactive Discussion



Figures 23 and 24 respectively show the split between surface biomass and integrated production for MEDUSA-2.0's two phytoplankton groups (shown on the same colour scales to facilitate intercomparison). Much as with MEDUSA-1.0, non-diatoms are dominant across most of the World Ocean, and particularly in the oligotrophic gyres, where diatom abundance and productivity is extremely low. However, diatom biomass can seasonally exceed that of the non-diatoms in regions such as the North Atlantic, and they still contribute modestly to total primary production (15.9%; 17.0% in terms of total nitrogen biomass). Observational estimates of this fraction at the global scale are rare. While a survey by Mann (1999) suggested 40–45%, this is much greater than that estimated by either MEDUSA-2.0 or localised observations (13–34%; Nelson and Brzezinski, 1997; Blain et al., 1997; Brzezinski et al., 1998).

The left panels of Fig. 25 show the fraction (0–1) of total primary production that MEDUSA-2.0 predicts for the upper mixed layer (the remainder occurring deeper in the water column). In general, this fraction is lower in the summer, when nutrients are more limiting than light, and higher in the winter, when light limits production more. Patterns are less clear in the tropics and upwelling regions where the interplay of nutrient and light availability is more complex. In the case of northern latitudes, the ratio generally shifts between 0.5–1.0, but in the Southern Ocean the seasonal range is 0.7–1.0, reflecting this basin's all-year macronutrient availability. Integrating to the global scale, slightly more than two-thirds (67.3%) of production occurs in the mixed layer in MEDUSA-2.0, and while there is geographical variation in this fraction between basins, the Southern Ocean is the most different at 85.8%.

The right panels of Fig. 25 instead show ocean productivity from the perspective of the benthic communities that ultimately rely on them. The panels are shown on a log scale because the geographical variability of export production is compounded exponentially by variability in the seafloor depth that sinking material needs to reach. Generally, the seafloor supply of organic material mirrors that of its source, primary production. It shows strong seasonality at high latitudes and low seasonality in the tropics, with the actual magnitude of supply to the benthos strongly tied to seafloor

depth (e.g. compare North Sea and Patagonian Shelf regions with adjacent deep water regions).

Following up on ocean productivity, Fig. 26 shows the patterns of limitation by nutrients for both modelled phytoplankton groups. The leftmost panels show overall phytoplankton growth limitation by nutrients (separate from light), while the rightmost panels indicate which nutrient provides the strongest limitation. In the case of diatoms, nitrogen and iron limitation are joined by silicon limitation. In broad outline, nitrogen is most limiting for both phytoplankton groups in oligotrophic gyres, while iron plays a more significant role in high latitude regions, particularly the Southern Ocean, and the equatorial Pacific. Note that, although iron is indicated as most-limiting in both the north Atlantic and Pacific, its impact is greater in the Pacific, particularly in the eastern region. For diatoms, the boundaries between regions of N- and Fe-limitation are typically where Si-limitation occurs, though in the North Atlantic in particular, the scarcity of silicon almost completely displaces iron stress. The geographical patterns in MEDUSA-2.0 generally parallel those of MEDUSA-1.0 (and other models; Moore et al., 2004), though the change in dust deposition forcing means that the equatorial Pacific experiences a greater degree of iron limitation.

Switching from the production of organic material, Fig. 27 shows the seasonal production of the biominerals opal and CaCO_3 . As with the preceding plots, production of both is highly seasonal at high latitudes, and more constant at low latitudes. Because of the differential availability of silicic acid, opal production is highest in the North Pacific and Southern Ocean, higher even than that in the tropics, though the latter's annual constancy leads to greater overall production. Patterns of CaCO_3 production – technically its export in MEDUSA-2.0 – are similarly seasonal, though the northern Atlantic and Pacific basins swap from the patterns shown with opal. However, within the northern reaches of both basins, opal and CaCO_3 production show different, non-overlapping geographical patterns. Global total opal production in MEDUSA-2.0 is $194 \text{ Tmol Si yr}^{-1}$, around 20 % lower than that estimated by Tréguer et al. (1995) (and

A description of
MEDUSA-2.0

A. Yool et al.

Title Page

Abstract

Introduction

Conclusions

References

Tables

Figures

◀

▶

◀

▶

Back

Close

Full Screen / Esc

Printer-friendly Version

Interactive Discussion



A description of MEDUSA-2.0

A. Yool et al.

Title Page

Abstract

Introduction

Conclusions

References

Tables

Figures

◀

▶

◀

▶

Back

Close

Full Screen / Esc

Printer-friendly Version

Interactive Discussion



lower than that in MEDUSA-1.0). Total CaCO_3 export in MEDUSA-2.0 is 0.41 GtCyr^{-1} , at the bottom end of the broad $0.4\text{--}1.8 \text{ GtCyr}^{-1}$ range estimated by Doney et al. (2009).

Switching again, this time to the consumption of organic material, Fig. 28 shows the seasonal distributions of surface concentrations of both zooplankton groups. Unsurprisingly, both show the same strong seasonality at high latitudes already seen. Though they have slower maximum growth and are less efficient at lower prey concentration, the wider range of available prey types provides a wider base for mesozooplankton and, coupled with their role as predator, makes them dominant in terms of biomass over microzooplankton.

Figures 29 and 30 show the production of the two size classes of detritus in MEDUSA-2.0, and the export of this material to the deep ocean. As with MEDUSA-1.0, the production of small particles dominates in the surface ocean (70.6%), but this dominance declines down the water column as these particles are quickly remineralised, such that, by 100 m, small particles are the minority component of the export flux (38.8%). By 1000 m, small particles are of almost no importance to abyssopelagic or benthic communities (2.2%). Note that, since large, fast-sinking particles have a tighter, less expansive distribution of production than do slow-sinking particles (per Fig. 29), deep water benthic communities in MEDUSA-2.0 experience greater variability in supply than do shallow water communities.

To illustrate longer-term trends in the performance of MEDUSA-2.0, Figs. 31 to 33 show basin-average vertical profiles of several of the model's major nutrient elements. Since the model is being simulated for a period during which climate change is comparatively limited (though anthropogenic CO_2 is increasing), and since these directly influence the behaviour of MEDUSA-2.0's ecological actors (unlike DIC, alkalinity and oxygen; results not shown), they illustrate the degree to which the model has equilibrated.

In the case of nitrogen, per Fig. 31, while globally there is a steady rise in near-surface concentrations – and a steady decrease in deep (2000–5000 m) concentrations – this is largely driven by changes in the Pacific Ocean, with the other basins

A description of MEDUSA-2.0

A. Yool et al.

Title Page

Abstract

Introduction

Conclusions

References

Tables

Figures

◀

▶

◀

▶

Back

Close

Full Screen / Esc

Printer-friendly Version

Interactive Discussion



showing much weaker trends. The pattern of Pacific dominance in the global signal continues with silicon, per Fig. 32, but surface changes are broadly much less significant. Both elements show rapid and significant changes in the Southern Ocean that are consistent with the circulation and watermass changes described earlier. Figure 33 shows the corresponding situation for iron, where the situation is complicated by large removal (scavenging) and addition (aeolian/benthic) fluxes. Here, changes are greatest at depth, where continual scavenging removes deep iron, but there is also a slight general decrease in the surface ocean. An exception lies with the Indian Ocean, which shows almost static surface concentrations.

Complementing these profiles, Fig. 34 shows annual time series of surface nitrogen, silicon and chlorophyll, and integrated primary production for the duration of the simulation. Note that the vertical scales have been focused to emphasise change across the simulation. Consistent with the profile plots above, both surface DIN and silicic acid show an increase during the simulation, but while DIN continues to gradually rise throughout its duration, silicic acid saturates relatively quickly (by 1880). In the case of DIN, this global trend generally reflects that at the surface of the Pacific Ocean, but for silicic acid the global trend is driven by the large increase in surface concentrations in the Southern Ocean. The lower two panels show trends in biological variables that are similar to that of DIN, and this similarity extends to its source, with, again, changes in the Pacific Ocean driving the wider global trend. In the case of primary production, almost all of the increase during the simulation (5 GtCyr^{-1}) is driven by the corresponding increase in the Pacific.

Finally, Tables 7 and 8 intercompare MEDUSA-1.0 and MEDUSA-2.0 for a range of common properties on a basin average basis. Table 7 focuses on the surface concentrations of major model components, plankton and nutrients. Generally, the two models show very similar patterns, though this is unsurprising given the relatively minor differences between their core nutrient dynamics. However, there are several notable differences in nutrient concentrations. For instance, surface nitrogen (+9.1%), silicon (+5.2%) and iron (+5.8%) are elevated globally in MEDUSA-2.0, but there are strong

regional biases. In the case of the Pacific Ocean, nitrogen increases by +74.4 %, while iron falls by -25.8 %. And some of the largest differences between the models occur in the Arctic Ocean (increased N, decreased Si). In part, the longer duration of MEDUSA-2.0's simulation (146 yr versus 40 yr) appears responsible for these differences, but the change in iron deposition forcing, especially in the Pacific, also appears a key factor in the change between the otherwise very similar models.

In terms of major biogeochemical fluxes, Table 8 shows, again, much congruence between the two versions of the model. As mentioned previously, the simulation of MEDUSA-2.0 exhibits lower productivity (-8.1 %), with knock-on consequences in phytoplankton biomass (-5.3 %) and opal production (-12.3 %). CaCO₃ production is more substantially impacted (-31.3 %), reflecting the compounded declines in both organic production and rain ratio in MEDUSA-2.0. Via the ballast submodel, decline in the production of both opal and CaCO₃ has a further impact on export production: in MEDUSA-1.0, 5.3 % of the 100 m flux of organic matter reached 1000 m, while in MEDUSA-2.0, only 4.4 % did.

4 Discussion

Despite the ever-increasing size of supercomputers, incorporating marine ecosystem models into global GCMs is a computationally expensive business when it comes to undertaking climate simulations, especially if high resolution is desired and/or the ocean is coupled to an atmospheric model. MEDUSA-1.0, the precursor to the version of the model described herein, was explicitly developed with this consideration in mind as an "intermediate complexity" plankton ecosystem model for global biogeochemical modelling. It simulates primary production, grazing and export of detritus to the deep ocean, the sinking particles containing both organic and inorganic C with the latter via a latitudinally-dependent "rain ratio". The base currency of MEDUSA-1.0 is nitrogen, the selection of a nutrient element (N or P) for this purpose being a necessity given the role of nutrients in limiting primary production in the ocean. Although MEDUSA-1.0

A description of MEDUSA-2.0

A. Yool et al.

Title Page

Abstract

Introduction

Conclusions

References

Tables

Figures

⏪

⏩

◀

▶

Back

Close

Full Screen / Esc

Printer-friendly Version

Interactive Discussion



A description of MEDUSA-2.0

A. Yool et al.

Title Page

Abstract

Introduction

Conclusions

References

Tables

Figures

◀

▶

◀

▶

Back

Close

Full Screen / Esc

Printer-friendly Version

Interactive Discussion



predicts the fluxes and cycling of organic carbon, simulating the full carbon cycle in the ocean, including ventilation of CO₂ with the atmosphere and the resulting impact of ocean acidification on marine ecosystems, requires additional tracers. Here, we describe MEDUSA-2.0, an expanded successor model which includes dissolved inorganic carbon, alkalinity, dissolved oxygen and detrital carbon as additional state variables, as well as a simple representation of the benthos.

In principle, the two versions of the model ought to give similar predictions given that phytoplankton, at the base of the food chain, are not limited by C, at least in the model (but see Riebesell et al., 2007). Differences do occur, however, for several reasons. Principally, the simulation described here used forcing from output of the HadGEM2-ES coupled model and was run for 145 yr (1860–2005), rather than observationally-derived DFS4.1 forcing and a simulation length of only 40 yr (1966–2005) as used with MEDUSA-1.0 (Yool et al., 2011). There were also minor parameter tweaks to adjust near-surface nutrients, as well as parameter changes and additions to accommodate the carbon and oxygen cycles. However, in general, the performance of the two models is very similar, in both cases successfully reproducing major features such as the oligotrophic gyres and the seasonal progression of plankton blooms at high latitudes. At the global scale, predicted primary production of 45.3 and 41.6 GtCyr⁻¹ for MEDUSA versions 1.0 and 2.0 respectively, are in line with, although slightly below, observationally-derived estimates of 46.3–60.4 GtCyr⁻¹ (Behrenfeld and Falkowski, 1997; Carr et al., 2006; Westberry et al., 2008). The lower primary production in MEDUSA-2.0 is in part a consequence of changes to productivity in the Pacific that result from the switch in MEDUSA-2.0 to a more modern aeolian deposition field (Mahowald, 2005). The resulting deficiency of iron additionally leads to excess DIN in the surface waters of the equatorial Pacific. Both models do a reasonable job at capturing the spatial and seasonal patterns of productivity, although various discrepancies with observations are seen including lower primary production in the subtropical gyres and elevated productivity in iron limited high-nutrient-low-chlorophyll (HNLC) regions including the Southern Ocean, equatorial Pacific and subarctic North Pacific. Predicted concentrations of DIN

and, especially, silicic acid are too high in the Southern Ocean, a result of excessive ventilation in this basin which acts to homogenise horizontal and vertical gradients. The problem is somewhat worse in MEDUSA-2.0 because ocean circulation in this region is strong under the HadGEM2-ES forcing used here. Note, however, that the longer duration of the MEDUSA-2.0 simulation allows for any deficiencies in either physics or biogeochemistry to more obviously manifest themselves.

A new feature of MEDUSA-2.0 is the inclusion of a simple benthic model. This serves as a series of four reservoirs for detrital material (slow- and fast-sinking) that reaches the seafloor – nitrogen, silicon, organic carbon, CaCO_3 ; but not iron, which is coupled to nitrogen. In MEDUSA-1.0 such material was instantaneously remineralised (or dissolved) upon reaching the seafloor. While this latter, simplistic approach has limited consequences in the deep ocean where the recycled dissolved inorganic nutrients cannot be consumed by phytoplankton growth, in shallower regions such as the shelves it has the potential to unrealistically enhance production. Patterns in the supply of organic matter to the seafloor closely mirror those of primary production in the surface ocean in the model. This supply thus shows strong seasonality at high latitudes and low sensitivity in the tropics. However, given the turnover of sinking particles as they descend through the water column, the magnitude of benthic supply is closely tied to seafloor depth.

As was the case with MEDUSA-1.0, the modelling of iron is still problematic. Aeolian deposition balances uneasily with scavenging, with the result that iron distributions diverge from those of the initial condition (admittedly model-derived; Dutkiewicz et al., 2005) at both the surface and, especially, at depth. The latter discrepancy has limited impact on the simulations here and in Yool et al. (2011) but it does illuminate gaps in understanding of this elemental cycle. While understanding of iron in the ocean has progressed in recent years (e.g. Boyd and Ellwood, 2010; Breitbarth et al., 2010), accurately representing iron in ecosystem models remains difficult for a number of reasons. For instance, accurate estimation of the iron supply to the ocean is hampered by our ignorance of both dust supply and dust solubility once in the ocean (Schulz et al.,

GMDD

6, 1259–1365, 2013

A description of MEDUSA-2.0

A. Yool et al.

Title Page

Abstract

Introduction

Conclusions

References

Tables

Figures

⏪

⏩

◀

▶

Back

Close

Full Screen / Esc

Printer-friendly Version

Interactive Discussion



A description of MEDUSA-2.0

A. Yool et al.

Title Page

Abstract

Introduction

Conclusions

References

Tables

Figures

◀

▶

◀

▶

Back

Close

Full Screen / Esc

Printer-friendly Version

Interactive Discussion



2012). Furthermore, even once in the ocean, iron's bioavailability is influenced by its various speciation and redox states, biological cycling and the various uptake strategies of phytoplankton and bacteria. And though increasingly complex representations of iron are being developed and incorporated into ecosystem models (e.g. Weber et al., 2007; Ye et al., 2009), the current generation of ocean biogeochemical GCMs typically only include a single iron pool and so cannot account for the roles of ligand complexation and nonbiological processes (light and temperature) in controlling bioavailable Fe and therefore the extent of phytoplankton limitation (Tagliabue et al., 2009).

Moving on to the carbon cycle, predicted patterns of $p\text{CO}_2$ and air–sea CO_2 exchange throughout the world ocean generally compare favourably to maps based on observations (Takahashi et al., 2009). Some areas, such as the northeast Pacific, show exaggerated patterns whereas in others, such as the Southern Ocean, seasonality in MEDUSA-2.0 is not as pronounced as that observed. Integrating to net CO_2 flux finds MEDUSA-2.0 in relatively close agreement with Takahashi et al. (2009). However, while the surface carbon cycle in MEDUSA-2.0 performs well, the duration of the simulation here is extremely restricted relative to overturning timescales (Ostlund and Stiver, 1980), and deep waters will not be equilibrated with the modelled circulation or biogeochemistry (compounded by unavoidable gaps and resulting interpolation in the GLODAP dataset used to initialise MEDUSA-2.0; Key et al., 2004). This is a common issue in ocean modelling, one that has traditionally been solved by brute force and long duration equilibrium simulations (e.g. Orr et al., 2005), but for which techniques are being developed (Khatiwala, 2007).

A significant consideration in MEDUSA-2.0 has been how to model calcification given the ongoing acidification of the ocean in response to increasing atmospheric CO_2 (Caldeira and Wickett, 2003). The physico-chemical factors controlling calcification in marine organisms are poorly understood, leading to a diverse range of approaches in models (e.g. Tyrrell and Taylor, 1996; Moore et al., 2002; Gehlen et al., 2007; Ridgwell et al., 2007; Zahariev et al., 2008; Yool et al., 2010). Anderson (2005) used calcifiers as an example of how difficult it is to reliably parameterise complex mod-

els for use in forecast projections. For example, the ecology of coccolithophores is poorly understood including the relative roles of bottom-up (via different nutrients) and top-down (grazing, viral lysis) controls on their dynamics. Further, calcifiers are a diverse group of organisms, including hundreds of species of coccolithophores, as well as foraminifera and pteropods. Grouping them into a single model state variable and then parameterising based on, for example, the well-known species *Emiliana huxleyi* is a potentially hazardous strategy. Ecosystem models used in global biogeochemical modelling studies have therefore adopted relatively simple approaches to the representation of calcification.

In MEDUSA-1.0, where nutrient cycles were of greater concern, the rain ratio of $\text{CaCO}_3 : \text{C}_{\text{org}}$ was made a simple empirical function of latitude (following Dunne et al., 2007). This approach captured some of the first order features of the rain ratio (e.g. equator–pole gradients) but prevented any sensitivity to physico-chemical changes (though changes in productivity would still impact the absolute quantity of calcification). For MEDUSA-2.0, the parameterisation of calcification was therefore improved to permit dynamic change under the influence ambient marine chemistry (Riebesell et al., 2000; Zondervan et al., 2001). As noted above, there are good reasons why a representation of a CaCO_3 production via a dedicated state variable (“coccolithophorid phytoplankton”, “pteropod zooplankton”) may be problematic. To this end, MEDUSA-2.0 adopts a calcification parameterisation which straightforwardly replaces that in MEDUSA-1.0, and which was developed for, and optimised to, the global scale (Ridgwell et al., 2007). Though developed within the framework of a low resolution Earth System Model, GENIE, and coupled to a simple “nutrient-restoring” biogeochemical framework, this parameterisation serves the same purpose there as in MEDUSA-2.0 – the production of exported CaCO_3 . Of course, the relationship that it assumes between Ω_{calcite} and CaCO_3 export is known to be diverse (e.g. Buitenhuis et al., 1999; Iglesias-Rodriguez et al., 2008; Langer et al., 2006), but it serves here as an obvious stepping stone in complexity for MEDUSA-2.0, and the potential impacts of adopting it are explored in a separate study (Yool et al., 2013).

A description of MEDUSA-2.0

A. Yool et al.

Title Page

Abstract

Introduction

Conclusions

References

Tables

Figures

⏪

⏩

◀

▶

Back

Close

Full Screen / Esc

Printer-friendly Version

Interactive Discussion



A description of MEDUSA-2.0

A. Yool et al.

Title Page

Abstract

Introduction

Conclusions

References

Tables

Figures

◀

▶

◀

▶

Back

Close

Full Screen / Esc

Printer-friendly Version

Interactive Discussion



In terms of future developments for MEDUSA-2.0, a number of avenues suggest themselves. The performance of the chlorophyll submodel remains somewhat problematic, with the model failing to simulate spring bloom concentrations as high as those observed, while having much lower concentrations in the unproductive oligotrophic gyres. The literature contains more sophisticated treatments of phytoplankton physiology than that used here (up to long-standing submodels such as Flynn, 2001) and the adoption of such a submodel may improve this aspect of MEDUSA-2.0. With the inclusion of the oxygen cycle, and the simulation of suboxic regions, MEDUSA-2.0's omission of denitrification could also be addressed (Deutsch et al., 2007). At the other end of the nitrogen cycle, the factors regulating the distribution of nitrogen fixation are increasingly well-understood (e.g. Moore and Doney, 2007; Monteiro and Follows, 2012), and this process both interacts with denitrification (Deutsch et al., 2007; Fernandez et al., 2011) and is expected to change into the future (Levitan et al., 2007; Barcelos e Ramos et al., 2007). Though much has been made above of MEDUSA-2.0's more sophisticated treatment of CaCO_3 , it is clear that this remains just one "solution" for this aspect of the ocean's carbon (and alkalinity) cycle. The broad range of ongoing research into the impacts of ocean acidification on calcifiers will continue to inform the modelling of CaCO_3 , and will hopefully provide a more "universal" understanding and formulation – for instance, a consensus on the ecophysiological factors that govern calcifier abundance. On a related point, the role played by CaCO_3 in the export of organic material to the deep ocean has been questioned (Passow and De La Rocha, 2006; Wilson et al., 2012), and MEDUSA-2.0's utilisation of the ballast hypothesis may require revisiting. And there are further omissions of MEDUSA-2.0, less immediately pressing, that could be considered. For example, CO_2 -enhanced carbon fixation (Riebesell et al., 2007) or DOM production (Engel, 2002), a more thorough treatment of elemental ratios (Burkhardt et al., 1999), the importance of food quality in grazing interactions (Mitra and Flynn, 2005) or phytoplankton mixotrophy (Hartmann et al., 2012).

However, notwithstanding the considerable room for improvement – or expansion – outlined above, the further development of MEDUSA-2.0 runs counter to the stated

intention that the model occupies the “intermediate complexity” niche of biogeochemical modelling. Furthermore, while potentially extending the reach – and utility – of MEDUSA-2.0 on several fronts, they present no method for expanding the model in a systematic or quasi-objective fashion. Piecemeal additions to model complexity, however warranted and justifiable, run the risk of creating a succession of “specialist models”, that while individually useful may not sit within a consistent heirarchy of complexity. As such, it may be difficult to fine-tune the biogeochemical complexity to suit a particular task (with particular resources) to hand.

Nonetheless, despite the limitations outlined above, MEDUSA-2.0 still represents an efficiently-sized tool for realistically simulating the ocean’s major biogeochemical cycles.

5 Conclusions

- MEDUSA-2.0 builds traceably on MEDUSA-1.0 by adding carbon, alkalinity and oxygen cycles, a simple benthos submodel and options for CaCO_3 production and export remineralisation
- Calcification submodel permits dynamic response to ambient seawater chemistry allowing investigation of ocean acidification feedbacks at an appropriate level of additional complexity
- MEDUSA-2.0 performace evaluated at the global scale using observational nutrient, chlorophyll and carbon cycle fields following a century-scale simulation (1860–2005)
- Similarly to predecessor model, MEDUSA-2.0 has excessive nutrient concentrations in Southern Ocean and low productivity in oligotrophic gyres; changes to aeolian iron deposition decrease Pacific productivity and increase excess surface DIN

A description of MEDUSA-2.0

A. Yool et al.

Title Page

Abstract

Introduction

Conclusions

References

Tables

Figures

◀

▶

◀

▶

Back

Close

Full Screen / Esc

Printer-friendly Version

Interactive Discussion



- MEDUSA-2.0 performance very similar to MEDUSA-1.0, though productivity slightly lower; generally good agreement on surface carbon cycle properties ($\Delta p\text{CO}_2$ and air–sea flux) and CaCO_3 production within observational range

Appendix A

5 MEDUSA-2.0 code

The following provides a structural outline of the computer code that accompanies this description of MEDUSA-2.0. As in Yool et al. (2011), this code does not encompass the entire NEMO model, but includes those modules that either include MEDUSA-2.0's calculations, or those in which MEDUSA-2.0 makes an appearance for operational reasons.

The MEDUSA-2.0 model is organised almost identically to MEDUSA-1.0, and in a similar manner to other passive tracer modules in the NEMO model. The majority of the code directly associated with MEDUSA-2.0 is located within the `NEMO/TOP_SRC/MEDUSA` directory. The actual model code is distributed across 11 separate routines as follows. Nine of these are common with MEDUSA-1.0, but the last two are new additions for MEDUSA-2.0 that deal primarily with air–sea gas exchange.

- `par_medusa.F90`
this routine declares the tracer and diagnostic arrays required for MEDUSA-2.0
- `sms_medusa.F90`
this routine declares the parameters required for MEDUSA-2.0
- `trcctl_medusa.F90`
this routine checks that the correct number of passive tracers is specified

GMDD

6, 1259–1365, 2013

A description of MEDUSA-2.0

A. Yool et al.

Title Page

Abstract

Introduction

Conclusions

References

Tables

Figures

◀

▶

◀

▶

Back

Close

Full Screen / Esc

Printer-friendly Version

Interactive Discussion



A description of MEDUSA-2.0

A. Yool et al.

Title Page

Abstract

Introduction

Conclusions

References

Tables

Figures

◀

▶

◀

▶

Back

Close

Full Screen / Esc

Printer-friendly Version

Interactive Discussion



- `trcini_medusa.F90`
this routine initialises the passive tracers to default values unless they are provided by a restart file
- `trclsm_medusa.F90`
5 this routine initialises the parameters to the values specified in `namelist.trc.sms`
- `trcsms_medusa.F90`
this routine is called by the NEMO model during a simulation and in turn calls the MEDUSA-2.0 routines that calculate biogeochemical sources and sinks
- `trcopt_medusa.F90`
10 this routine calculates the submarine light field
- `trcbio_medusa.F90`
this is the main model routine and includes (almost) all of the ecosystem equations used for the biogeochemical sources and sinks for tracers
- `trcsed_medusa.F90`
15 this routine both initialises the aeolian iron deposition and Ω_{calcite} CCD fields (if required) and (for historical reasons) calculates the sinking of the slow detritus tracer
- `trcco2_medusa.F90`
20 this routine is called by `trcbio_medusa.F90` to perform calculations associated with carbonate chemistry and air–sea CO_2 flux; while modified to interface with MEDUSA-2.0, it is derived from Blackford et al. (2007)
- `trcoxy_medusa.F90`
25 this routine is called by `trcbio_medusa.F90` to perform calculations associated with saturation concentration and air–sea O_2 flux; while modified to interface with MEDUSA-2.0, it is derived from Najjar and Orr (1999)

As with MEDUSA-1.0, the above routines are included in the supplementary material that accompanies this article.

Acknowledgements. The authors gratefully acknowledge the financial support of the Natural Environmental Research Council (NERC). This work was performed as part of the Regional Ocean Modelling project (ROAM; grant number NE/H017372/1) of the NERC UK Ocean Acidification research programme (UKOA).

The authors are additionally grateful to the NEMO development team at NOC for their technical support throughout this work. In particular, the assistance of Beverly de Cuevas and Steven Alderson has been invaluable in the development and simulation of MEDUSA-2.0.

The HadGEM2-ES atmospheric forcing was produced by the UKMO and made available for use by NEMO by Dan Bernie (UKMO). Work to perform HadGEM2-ES simulations was supported by the EU-FP7 COMBINE project (grant number 226520). The carbonate chemistry scheme utilised by MEDUSA-2.0 to calculate, among other things, air-sea CO₂ flux was generously supplied by Jerry Blackford (PML). The simple benthic reservoir scheme used here is based on a similar scheme developed, and supplied, by Momme Butenschön (PML).

The development of MEDUSA-2.0 greatly benefitted from discussions with a number of local and nonlocal colleagues, including: John Hemmings, Stephanie Henson, Adrian Martin and Ian Totterdell. The authors would also like to acknowledge suggestions from their fellow participants in the UKOA programme.

References

- Anderson, T. R.: Plankton functional type modelling: running before we can walk?, *J. Plankton Res.*, 27, 1073–1081, doi:10.1093/plankt/fbi076, 2005. 1263, 1306
- Anderson, T. R. and Pondaven, P.: Non-redfield carbon and nitrogen cycling in the Sargasso Sea: pelagic imbalances and export flux, *Deep-Sea Res. Pt. I*, 50, 573–591, 2003. 1276, 1288, 1290
- Anderson, T. R., Gentleman, W. C., and Sinha, B.: Influence of grazing formulations on the emergent properties of a complex ecosystem model in a global ocean general circulation model, *Prog. Oceanogr.*, 87, 201–213, doi:10.1016/j.pocean.2010.06.003, 2010. 1280

GMDD

6, 1259–1365, 2013

A description of MEDUSA-2.0

A. Yool et al.

Title Page

Abstract

Introduction

Conclusions

References

Tables

Figures

◀

▶

◀

▶

Back

Close

Full Screen / Esc

Printer-friendly Version

Interactive Discussion



A description of
MEDUSA-2.0

A. Yool et al.

Title Page

Abstract

Introduction

Conclusions

References

Tables

Figures

◀

▶

◀

▶

Back

Close

Full Screen / Esc

Printer-friendly Version

Interactive Discussion



- Antonov, J. I., Seidov, D., Boyer, T. P., Locarnini, R. A., Mishonov, A. V., Garcia, H. E., Baranova, O. K., Zweng, M. M., and Johnson, D. R.: World ocean atlas 2009, volume 2: salinity, in: NOAA Atlas NESDIS 69, edited by: Levitus, S., US Government Printing Office, Washington, DC, USA, 184 pp., 2010. 1286, 1293
- 5 Archer, D.: Modeling the calcite lysocline, *J. Geophys. Res.*, 96, 17037–17050, 1991. 1262
- Armstrong, R. A., Lee, C., Hedges, J. I., Honjo, S., and Wakeham, S. G.: A new, mechanistic model for organic carbon fluxes in the ocean: based on the quantitative association of POC with ballast minerals, *Deep-Sea Res. Pt. II*, 49, 219–236, 2002. 1262, 1282, 1284
- Artoili, Y., Blackford, J. C., Butenschon, M., Holt, J. T., Wakelin, S. L., Thomas, H., Borges, A. V., and Allen, J. I.: The carbonate system of the North Sea: sensitivity and model validation, *J. Marine Syst.*, 102, 1–13, 2012. 1288
- 10 Barcelos e Ramos, J., Biswas, H., Schulz, K. G., LaRoche, J., and Riebesell, U.: Effect of rising atmospheric carbon dioxide on the marine nitrogen fixer *Trichodesmium*, *Global Biogeochem. Cy.*, 21, GB2028, doi:10.1029/2006GB002898, 2007. 1308
- 15 Barnier, B., Madec, G., Penduff, T., Molines, J.-M., Treguier, A.-M., Le Sommer, J., Beckmann, A., Boning, C., Dengg, J., Derval, C., Durand, E., Gulev, S., Remy, E., Talandier, C., Theerren, S., Maltrud, M., McClean, J., and de Cuevas, B.: Impact of partial steps and momentum advection schemes in a global ocean circulation model at eddy-permitting resolution, *Ocean Dynam.*, 56, 543–567, doi:10.1007/s10236-006-0082-1, 2006. 1293
- 20 Behrenfeld, M. J. and Falkowski, P. G.: Photosynthetic rates derived from satellite-based chlorophyll concentration, *Limnol. Oceanogr.*, 42, 1–20, 1997. 1294, 1295, 1304
- Behrenfeld, M. J., Olley, R. T., Siegel, D. A., McClain, C. R., Sarmiento, J. L., Feldman, G. C., Milligan, A. J., Falkowski, P. G., Letelier, R. M., and Boss, E. S.: Climate-driven trends in contemporary ocean productivity, *Nature*, 444, 752–755, 2006. 1261
- 25 Blackford, J. C. and Gilbert, F. J.: pH variability and CO₂ induced acidification in the North Sea, *J. Marine Syst.*, 64, 229–241, doi:10.1016/j.jmarsys.2006.03.016, 2007. 1288, 1311
- Blain, S., Leynaert, A., Tréguer, P., Chretiennot-Dinet, M. C., and Rodier, M.: Biomass, growth rates and limitation of equatorial Pacific diatoms, *Deep-Sea Res. Pt. I*, 44, 1255–1275, 1997. 1299
- 30 Bopp, L., Monfray, P., Aumont, O., Dufresne, J.-L., Le Treut, H., Madec, G., Terray, L. and Orr, J. C.: Potential impact of climate change on marine export production, *Global Biogeochem. Cy.*, 15, 81–99, doi:10.1029/1999GB001256, 2001. 1261

A description of MEDUSA-2.0

A. Yool et al.

Title Page

Abstract

Introduction

Conclusions

References

Tables

Figures

◀

▶

◀

▶

Back

Close

Full Screen / Esc

Printer-friendly Version

Interactive Discussion



- Boyd, P. W. and Ellwood, M. J.: The biogeochemical cycle of iron in the ocean, *Nat. Geosci.*, 3, 675–682, 2010. 1305
- Boye, M., Aldrich, A. P., van den Berg, C. M. G., de Jong, J. T. M., Veldhuis, M., and de Baar, H. J. W.: Horizontal gradient of the chemical speciation of iron in surface waters of the northeast Atlantic Ocean, *Mar. Chem.*, 80, 129–143, 2003. 1281
- Breitbarth, E., Achterberg, E. P., Ardelan, M. V., Baker, A. R., Bucciarelli, E., Chever, F., Croot, P. L., Duggen, S., Gledhill, M., Hassellöv, M., Hassler, C., Hoffmann, L. J., Hunter, K. A., Hutchins, D. A., Ingri, J., Jickells, T., Lohan, M. C., Nielsdóttir, M. C., Sarthou, G., Schoemann, V., Trapp, J. M., Turner, D. R., and Ye, Y.: Iron biogeochemistry across marine systems – progress from the past decade, *Biogeosciences*, 7, 1075–1097, doi:10.5194/bg-7-1075-2010, 2010. 1305
- Brzezinski, M. A., Villareal, T. A., and Lipschultz, F.: Silica production and the contribution of diatoms to new and primary production in the central North Pacific, *Mar. Ecol.-Prog. Ser.*, 167, 89–104, 1998. 1299
- Buitenhuis, E. T., de Baar, H. J. W., and Veldhuis, M. J. W.: Photosynthesis and calcification by *Emiliania huxleyi* (Prymnesiophyceae) as a function of inorganic carbon species, *J. Phycol.*, 35, 949–959, doi:10.1046/j.1529-8817.1999.3550949.x, 1999. 1307
- Burkhardt, S., Riebesell, U., and Zondervan, I.: Effects of CO₂ concentration on C : N:P ratio in marine phytoplankton: a species comparison, *Limnol. Oceanogr.*, 44, 683–690, 1999. 1308
- Caldeira, K. and Wickett, M. E.: Anthropogenic carbon and ocean pH, *Nature*, 425, 365–365, doi:10.1038/425365a, 2003. 1306
- Carr, M.-E., Friedrichs, M. A. M., Schmeltz, M., Aita, M. N., Antoine, D., Arrigo, K. R., Asanuma, I., Aumont, O., Barber, R., Behrenfeld, M., Bidigare, R., Buitenhuis, E. T., Campbell, J., Ciotti, A., Dierssen, H., Dowell, M., Dunne, J., Esaias, W., Gentili, B., Gregg, W., Groom, S., Hoepffner, N., Ishizaka, J., Kameda, T., Le Quéré, C., Lohrenz, S., Marra, J., Mélin, F., Moore, K., Morel, A., Reddy, T. E., Ryan, J., Scardi, M., Smyth, T., Turpie, K., Tilstone, G., Waters, K., and Yamanaka, Y.: A comparison of global estimates of marine primary production from ocean color, *Deep-Sea Res. Pt. II*, 53, 741–770, 2006. 1294, 1295, 1304
- Collins, W. J., Bellouin, N., Doutriaux-Boucher, M., Gedney, N., Halloran, P., Hinton, T., Hughes, J., Jones, C. D., Joshi, M., Liddicoat, S., Martin, G., O'Connor, F., Rae, J., Senior, C., Sitch, S., Totterdell, I., Wiltshire, A., and Woodward, S.: Development and evaluation of an Earth-System model – HadGEM2, *Geosci. Model Dev.*, 4, 1051–1075, doi:10.5194/gmd-4-1051-2011, 2011. 1292

A description of MEDUSA-2.0

A. Yool et al.

Title Page

Abstract

Introduction

Conclusions

References

Tables

Figures

◀

▶

◀

▶

Back

Close

Full Screen / Esc

Printer-friendly Version

Interactive Discussion



- Deutsch, C., Sarmiento, J. L., Sigman, D. M., Gruber, N., and Dunne, J. P.: Spatial coupling of nitrogen inputs and losses in the ocean, *Nature*, 445, 163–167, doi:10.1038/nature05392, 2007. 1308
- Doney, S. C., Fabry, V. J., Feely, R. A., and Kleypas, J. A.: Ocean acidification: the other CO₂ problem, *Annu. Rev. Mar. Sci.*, 1, 169–192, 2009. 1261, 1301
- Doney, S. C., Ruckelshaus, M., Duffy, J. E., Barry, J. P., Chan, F., English, C. A., Galindo, H. M., Grebmeier, J. M., Hollowed, A. B., Knowlton, N., Polovina, J., Rabalais, N. N., Sydeman, W. J., and Talley, L. D.: Climate change impacts on marine ecosystems, *Annu. Rev. Mar. Sci.*, 4, 11–37, 2012. 1261
- DRAKKAR Group: Eddy-permitting ocean circulation hindcasts of past decades, *CLIVAR Exchang.*, 42, 8–10, 2007. 1266, 1291
- Dunne, J. P., Sarmiento, J. L., and Gnanadesikan, A.: A synthesis of global particle export from the surface ocean and cycling through the ocean interior and on the seafloor, *Global Biogeochem. Cy.*, 21, GB4006, doi:10.1029/2006GB002907, 2007. 1284, 1285, 1307
- Dutkiewicz, S., Follows, M. J., and Parekh, P.: Interactions of the iron and phosphorus cycles: a three-dimensional model study, *Global Biogeochem. Cy.*, 19, GB1021, doi:10.1029/2004GB002342, 2005. 1280, 1281, 1293, 1305
- Edwards, A. M. and Yool, A.: The role of higher predation in plankton population models, *J. Plankton Res.*, 22, 1085–1112, 2000. 1280
- Engel, A.: Direct relationship between CO₂-uptake and transparent exopolymer particles (TEP) production in natural phytoplankton, *J. Plankton Res.*, 24, 49–53, 2002. 1308
- Eppley, R. W.: Temperature and phytoplankton growth in the sea, *Fish. Bull. Nat. Ocean Atmos. Adm.*, 70, 1063–1085, 1972. 1272
- Fabry, V. J., Seibel, B. A., Feely, R. A., and Orr, J. C.: Impacts of ocean acidification on marine fauna and ecosystem processes, *ICESJ. Mar. Sci.* 65, 414–432, 2008. 1261
- Fasham, M. J. R.: Modelling the marine biota, in: *The Global Carbon Cycle*, edited by: Heimann, M., Springer-Verlag, New York, USA, 457–504, 1993. 1280
- Fasham, M. J. R., Ducklow, H. W., and McKelvie, S. M.: A nitrogen-based model of plankton dynamics in the oceanic mixed layer, *J. Mar. Res.*, 48, 591–639, 1990. 1276
- Fasham, M. J. R., Flynn, K. J., Pondaven, P., Anderson, T. R., and Boyd, P. W.: Development of a robust marine ecosystem model to predict the role of iron in biogeochemical cycles: a comparison of results for iron-replete and iron-limited areas, and the SOIREE iron-enrichment experiment, *Deep-Sea Res. Pt. I*, 53, 333–366, doi:10.1016/j.dsr.2005.09.011, 2006. 1289

A description of MEDUSA-2.0

A. Yool et al.

Title Page

Abstract

Introduction

Conclusions

References

Tables

Figures

◀

▶

◀

▶

Back

Close

Full Screen / Esc

Printer-friendly Version

Interactive Discussion



- Fernandez, C., Farías, L., and Ulloa, O.: Nitrogen fixation in denitrified marine waters, *PLoS ONE*, 6, e20539, doi:10.1371/journal.pone.0020539, 2011. 1308
- Fichefet, T. and Morales Maqueda, M. A.: Sensitivity of a global sea ice model to the treatment of ice thermodynamics and dynamics, *J. Geophys. Res.*, 102, 12609–12646, 1997. 1291
- 5 Flynn, K. J.: A mechanistic model for describing dynamic multi-nutrient, light, temperature interactions in phytoplankton, *J. Plankton Res.*, 23, 977–997, 2001. 1308
- Frankignoulle, M., Canon, C., and Gattuso, J.-P.: Marine calcification as a source of carbon dioxide: Positive feedback of increasing atmospheric CO₂, *Limnol. Oceanogr.*, 39, 458–462, 1994. 1261
- 10 Gangstø, R., Joos, F., and Gehlen, M.: Sensitivity of pelagic calcification to ocean acidification, *Biogeosciences*, 8, 433–458, doi:10.5194/bg-8-433-2011, 2011. 1261
- Garcia, H. E., Locarnini, R. A., Boyer, T. P., Antonov, J. I., Baranova, O. K., Zweng, M. M., and Johnson, D. R.: World ocean atlas 2009, volume 3: dissolved oxygen, apparent oxygen utilization, and oxygen saturation, in: NOAA Atlas NESDIS 70, edited by: Levitus, S., US Government Printing Office, Washington, DC, 344 pp., 2010a. 1293
- 15 Garcia, H. E., Locarnini, R. A., Boyer, T. P., Antonov, J. I., Zweng, M. M., Baranova, O. K., and Johnson, D. R., World ocean atlas 2009, volume 4: nutrients (phosphate, nitrate, silicate), in: NOAA Atlas NESDIS 71, edited by: Levitus, S., US Government Printing Office, Washington, DC, 398 pp., 2010b. 1293, 1294
- 20 Gaspar, P., Grégoris, Y., and Lefevre, J.-M.: A simple eddy kinetic energy model for simulations of the oceanic vertical mixing tests at station papa and long-term upper ocean study site, *J. Geophys. Res.*, 95, 16179–16193, 1990. 1291
- Gehlen, M., Gangstø, R., Schneider, B., Bopp, L., Aumont, O., and Ethe, C.: The fate of pelagic CaCO₃ production in a high CO₂ ocean: a model study, *Biogeosciences*, 4, 505–519, doi:10.5194/bg-4-505-2007, 2007. 1283, 1306
- 25 Gledhill, M. and van den Berg, C.: Determination of complexation of iron (III) with natural organic complexing ligands in seawater using cathodic stripping voltammetry, *Mar. Chem.*, 47, 41–54, 1994. 1281
- Hartmann, M., Grob, C., Tarran, G. A., Martin, A. P., Burkhill, P. H., Scanlan, D. J., and Zubkov, M. V.: Mixotrophic basis of Atlantic oligotrophic ecosystems, *P. Natl. Acad. Sci. USA*, 109, 5756–5760, doi:10.1073/pnas.1118179109, 2012. 1308
- 30 Heinze, C.: Simulating oceanic CaCO₃ export production in the greenhouse, *Geophys. Res. Lett.*, 31, L16308, doi:10.1029/2004gl020613, 2004. 1262

A description of MEDUSA-2.0

A. Yool et al.

Title Page

Abstract

Introduction

Conclusions

References

Tables

Figures

◀

▶

◀

▶

Back

Close

Full Screen / Esc

Printer-friendly Version

Interactive Discussion



Henson, S. A., Sanders, R., Madsen, E., Morris, P. J., Le Moigne, F., and Quartly, G. D.: A reduced estimate of the strength of the ocean's biological carbon pump, *Geophys. Res. Lett.*, 38, L04606, doi:10.1029/2011GL046735, 2011. 1266, 1329

Henson, S. A., Sanders, R., and Madsen, E.: Global patterns in efficiency of particulate organic carbon export and transfer to the deep ocean, *Global Biogeochem. Cy.*, 26, GB1028, doi:10.1029/2011GB004099, 2012. 1287

Hibler, W. D.: A dynamic thermodynamic sea ice model, *J. Phys. Oceanogr.*, 9, 815–846, 1979. 1291

Houghton, J. T. Ding, Y., Griggs, D. J., Noguer, M., van der Linden, P. J., Dai, X., Maskell, K. and Johnson, C. A. (Eds.): Intergovernmental Panel on Climate Change 2001: the Scientific Basis, Cambridge University Press, Cambridge, UK, 881 pp., 2001. 1260

Iglesias-Rodriguez, M. D., Halloran, P. R., Rickaby, R. E. M., Hall, I. R., Colmenero-Hidalgo, E., Gittins, J. R., Green, D. R. H., Tyrrell, T., Gibbs, S. J., von Dassow, P., Rehm, E., Armbrust, E. V., and Boessenkool, K. P.: Phytoplankton calcification in a high-CO₂ world, *Science*, 320, 336–340, doi:10.1126/science.1154122, 2008. 1307

Johns, T. C., Durman, C. F., Banks, H. T., Roberts, M. J., McLaren, A. J., Ridley, J. K., Senior, C. A., Williams, K. D., Jones, A., Rickard, G. J., Cusack, S., Ingram, W. J., Crucifix, M., Sexton, D. M. H., Joshi, M. M., Dong, D.-W., Spencer, H., Hill, R. S. R., Gregory, J. M., Keen, A. B., Pardaens, A. K., Lowe, J. A., Bodas-Salcedo, A., Stark, S., and Searl, Y.: The new Hadley Centre Climate Model (HadGEM1): evaluation of coupled simulations, *J. Climate*, 19, 1327–1353, 2006. 1292

Jones, C. D., Hughes, J. K., Bellouin, N., Hardiman, S. C., Jones, G. S., Knight, J., Lid-dicoat, S., O'Connor, F. M., Andres, R. J., Bell, C., Boo, K.-O., Bozzo, A., Butchart, N., Cadule, P., Corbin, K. D., Doutriaux-Boucher, M., Friedlingstein, P., Gornall, J., Gray, L., Halloran, P. R., Hurtt, G., Ingram, W. J., Lamarque, J.-F., Law, R. M., Meinshausen, M., Osprey, S., Palin, E. J., Parsons Chini, L., Raddatz, T., Sanderson, M. G., Sellar, A. A., Schurer, A., Valdes, P., Wood, N., Woodward, S., Yoshioka, M., and Zerroukat, M.: The HadGEM2-ES implementation of CMIP5 centennial simulations, *Geosci. Model Dev.*, 4, 543–570, doi:10.5194/gmd-4-543-2011, 2011. 1292

Key, R. M., Kozyr, A., Sabine, C. L., Lee, K., Wanninkhof, R., Bullister, J. L., Feely, R. A., Millero, F. J., Mordy, C., and Peng, T.-H.: A global ocean carbon climatology: results from Global Data Analysis Project (GLODAP), *Global Biogeochem. Cy.*, 18, GB4031, doi:10.1029/2004GB002247, 2004. 1286, 1293, 1294, 1306

- Khatiwala, S.: A computational framework for simulation of biogeochemical tracers in the ocean, *Global Biogeochem. Cy.*, 21, GB3001, doi:10.1029/2007GB002923, 2007. 1306
- Klaas, C., and Archer, D.: Association of sinking organic matter with various types of mineral ballast in the deep sea: implications for the rain ratio, *Global Biogeochem. Cy.*, 16, 1116, doi:10.1029/2001GB001765, 2002. 1262, 1285
- Langer, G., Geisen, M., Baumann, K. H., Kläs, J., Riebesell, U., Thoms, S., and Young, J. R.: Species-specific responses of calcifying algae to changing seawater carbonate chemistry, *Geochem. Geophys. Geos.*, 7, Q09006, doi:10.1029/2005GC001227, 2006. 1307
- Levitan, O., Rosenberg, G., Setlik, I., Setlikova, E., Grigel, J., Klepetar, J., Prasil, O., and Berman-Frank, I.: Elevated CO₂ enhances nitrogen fixation and growth in the marine cyanobacterium *Trichodesmium*, *Global Change Biol.*, 13, 531–538, 2007. 1308
- Locarnini, R. A., Mishonov, A. V., Antonov, J. I., Boyer, T. P., Garcia, H. E., Baranova, O. K., Zweng, M. M., and Johnson, D. R.: *World ocean atlas 2009, volume 1: temperature*, in: NOAA Atlas NESDIS 68, edited by: Levitus, S., US Government Printing Office, Washington, DC, USA, 184 pp., 2010. 1286, 1293
- Madec, G.: NEMO Reference Manual, Ocean Dynamic Component: NEMO-OPA, Note du Pole de modélisation, Technical Report 27, Note du Pole de Modélisation, Institut Pierre Simon Laplace, Paris, France, No. 27, ISSN 1288–1619, 2008. 1290, 1291
- Madec, G., Delecluse, P., Imbard, M., and Lévy, C.: OPA 8.1 Ocean General Circulation Model Reference Manual, Technical Report 11, Note du Pole de Modélisation, Institut Pierre Simon Laplace, Paris, France, 91 pp., 1998. 1290
- Mahowald, N. M., Baker, A. R., Bergametti, G., Brooks, N., Duce, R. A., Jickells, T. D., Kubilay, N., Prospero, J. M., and Tegen, I.: Atmospheric global dust cycle and iron inputs to the ocean, *Global Biogeochem. Cy.*, 19, GB4025, doi:10.1029/2004GB002402, 2005. 1265, 1281, 1304
- Mann, D. G.: The species concept in diatoms, *Phycologia*, 38, 437–495, 1999. 1299
- Martin, J. H., Knauer, G. A., Karl, D. M., and Broenkow, W. W.: VERTEX: carbon cycling in the northeastern Pacific, *Deep-Sea Res. Pt. I*, 34, 267–285, 1987. 1266, 1287, 1329
- Martin-Jézéquel, V., Hildebrand, M., and Brzezinski, M. A.: Silicon metabolism in diatoms: implications for growth, *J. Phycol.*, 36, 821–840, 2000. 1274
- Meijers, A. J. S., Shuckburgh, E., Bruneau, N., Sallee, J.-B., Bracegirdle, T. J., and Wang, Z.: Representation of the Antarctic circumpolar current in the CMIP5 climate

GMDD

6, 1259–1365, 2013

A description of MEDUSA-2.0

A. Yool et al.

Title Page

Abstract

Introduction

Conclusions

References

Tables

Figures

◀

▶

◀

▶

Back

Close

Full Screen / Esc

Printer-friendly Version

Interactive Discussion



A description of MEDUSA-2.0

A. Yool et al.

Title Page

Abstract

Introduction

Conclusions

References

Tables

Figures

◀

▶

◀

▶

Back

Close

Full Screen / Esc

Printer-friendly Version

Interactive Discussion



models and future changes under warming scenarios, *J. Geophys. Res.*, 117, C12008, doi:10.1029/2012JC008412, 2012. 1296

Mitra, A. and Flynn, K. J.: Predator-prey interactions: is “ecological stoichiometry” sufficient when good food goes bad?, *J. Plankton Res.*, 27, 393–399, doi:10.1093/plankt/fbi022, 2005. 1308

Mongin, M., Nelson, D. M., Pondaven, P., and Tréguer, P.: Simulation of upper-ocean biogeochemistry with a flexible-composition phytoplankton model: C, N and Si cycling and Fe limitation in the Southern Ocean, *Deep-Sea Res. Pt. II*, 53, 601–619, 2006. 1273, 1280

Monteiro, F. M. and Follows, M. J.: On nitrogen fixation and preferential remineralization of phosphorus, *Geophys. Res. Lett.*, 39, L06607, doi:10.1029/2012GL050897, 2012. 1308

Moore, J. K. and Doney, S. C.: Iron availability limits the ocean nitrogen inventory stabilizing feedbacks between marine denitrification and nitrogen fixation, *Global Biogeochem. Cy.*, 21, GB2001, doi:10.1029/2006GB002762, 2007. 1308

Moore, J. K., Doney, S. C., Kleypas, J. A., Glover, D. M., and Fung, I. Y.: An intermediate complexity marine ecosystem model for the global domain, *Deep-Sea Res. Pt. II*, 49, 403–462, 2002. 1283, 1306

Moore, J. K., Doney, S. C., and Lindsay, K.: Upper ocean ecosystem dynamics and iron cycling in a global three-dimensional model, *Global Biogeochem. Cy.*, 18, GB4028, doi:10.1029/2004GB002220, 2004. 1281, 1300

Najjar, R. G. and Orr, J. C.: Biotic-HOWTO, OCMIP-2 Project, 15 pp., online available at: <http://ocmip5.ipsl.jussieu.fr/OCMIP/phase2/simulations/Biotic/HOWTO-Biotic.html>, accessed 18 February 2013, 1999. 1288, 1289, 1311

Najjar, R. G., Jin, X., Louanchi, F., Aumont, O., Caldeira, K., Doney, S. C., Dutay, J.–C., Follows, M., Gruber, N., Joos, F., Lindsay, K., Maier–Reimer, E., Matear, R. J., Matsumoto, K., Monfray, P., Mouchet, A., Orr, J. C., Plattner, G.–K., Sarmiento, J. L., Schlitzer, R., Slater, R. D., Weirig, M.–F., Yamanaka, Y., and Yool, A.: Impact of circulation on export production, dissolved organic matter, and dissolved oxygen in the ocean: results from phase II of the Ocean Carbon-cycle Model Intercomparison Project (OCMIP-2), *Global Biogeochem. Cy.*, 21, GB3007, doi:10.1029/2006GB002857, 2007. 1291

Nelson, D. M. and Brzezinski, M. A.: Diatom growth and productivity in an oligotrophic mid-ocean gyre: a 3-year record from the Sargasso Sea near Bermuda, *Limnol. Oceanogr.*, 42, 473–486, 1997. 1299

A description of MEDUSA-2.0

A. Yool et al.

Title Page

Abstract

Introduction

Conclusions

References

Tables

Figures

◀

▶

◀

▶

Back

Close

Full Screen / Esc

Printer-friendly Version

Interactive Discussion



- O'Reilly, J. E., Maritorena, S., Mitchell, B. G., Siegal, D. A., Carder, K. L., Garver, S. A., Kahru, M., and McClain, C.: Ocean color chlorophyll algorithms for SeaWiFS, *J. Geophys. Res.*, 103, 24937–24953, 1998. 1294
- Orr, J. C., Fabry, V. J., Aumont, O., Bopp, L., Doney, S. C., Feely, R. A., Gnanadesikan, A., Gruber, N., Ishida, A., Joos, F., Key, R. M., Lindsay, K., Maier-Reimer, E., Matear, R., Monfray, P., Mouchet, A., Najjar, R. G., Plattner, G.-K., Rodgers, K. B., Sabine, C. L., Sarmiento, J. L., Schlitzer, R., Slater, R. D., Totterdell, I. J., Weirig, M.-F., Yamanaka, Y., and Yool, A.: Anthropogenic ocean acidification over the twenty-first century and its impact on calcifying organisms, *Nature*, 437, 681–686, 2005. 1261, 1306
- Östlund, G. and Stuiver, M.: GEOSECS Pacific radiocarbon, *Radiocarbon*, 22, 25–53, 1980. 1306
- Parekh, P., Follows, M. J., and Boyle, E. A.: Decoupling of iron and phosphate in the global ocean, *Global Biogeochem. Cy.*, 19, GB2020, doi:10.1029/2004GB002280, 2005. 1293
- Passow, U. and De La Rocha, C. L.: Accumulation of mineral ballast on organic aggregates, *Global Biogeochem. Cy.*, 20, GB1013, doi:10.1029/2005GB002579, 2006. 1308
- Penduff, T., Le Sommer, J., Barnier, B., Treguier, A.-M., Molines, J.-M., and Madec, G.: Influence of numerical schemes on current-topography interactions in 1/4° global ocean simulations, *Ocean Sci.*, 3, 509–524, doi:10.5194/os-3-509-2007, 2007. 1293
- Penduff, T., Juza, M., Brodeau, L., Smith, G. C., Barnier, B., Molines, J.-M., Treguier, A.-M., and Madec, G.: Impact of global ocean model resolution on sea-level variability with emphasis on interannual time scales, *Ocean Sci.*, 6, 269–284, doi:10.5194/os-6-269-2010, 2010. 1293
- Pollard, R. T., Salter, I., Sanders, R. J., Lucas, M. I., Moore, M., Mills, R. A., Statham, P. J., Allen, J. T., Baker, A. R., Bakker, D. C. E., Charette, M. A., Fielding, S., Fones, G. R., French, M., Hickman, A. E., Holland, R. J., Hughes, J. A., Jickells, T. D., Lampitt, R. S., Morris, P. J., Nédélec, F. H., Nielsdóttir, M., Planquette, H., Popova, E. E., Poulton, A. J., Read, J. F., Seeyave, S., Smith, T., Stinchcombe, M., Taylor, S., Thomalla, S., Venables, H. J., Williamson, R., and Zubkov, M. V.: Southern Ocean deep-water carbon export enhanced by natural iron fertilization, *Nature*, 457, 577–580, doi:10.1038/nature07716, 2009. 1281
- Popova, E. E., Coward, A. C., Nurser, G. A., de Cuevas, B., Fasham, M. J. R., and Anderson, T. R.: Mechanisms controlling primary and new production in a global ecosystem model – Part I: Validation of the biological simulation, *Ocean Sci.*, 2, 249–266, doi:10.5194/os-2-249-2006, 2006. 1270

A description of MEDUSA-2.0

A. Yool et al.

Title Page

Abstract

Introduction

Conclusions

References

Tables

Figures

◀

▶

◀

▶

Back

Close

Full Screen / Esc

Printer-friendly Version

Interactive Discussion



- Ridgwell, A., Zondervan, I., Hargreaves, J. C., Bijma, J., and Lenton, T. M.: Assessing the potential long-term increase of oceanic fossil fuel CO₂ uptake due to CO₂-calcification feedback, *Biogeosciences*, 4, 481–492, doi:10.5194/bg-4-481-2007, 2007. 1284, 1306, 1307, 1328
- Riebesell, U., Zondervan, I., Rost, B., Tortell, P. D., Zeebe, R. E., and Morel, F. M. M.: Reduced calcification of marine plankton in response to increased atmospheric CO₂, *Nature*, 407, 364–367, doi:10.1038/35030078, 2000. 1307
- Riebesell, U., Schulz, K. G., Bellerby, R. G. J., Botros, M., Fritsche, P., Meyerhöfer, M., Neill, C., Nondal, G., Oschlies, A., Wohlers, J., and Zöllner, E.: Enhanced biological carbon consumption in a high CO₂ ocean, *Nature*, 450, 545–548, doi:10.1038/nature06267, 2007. 1304, 1308
- Rose, A. L. and Waite, T. D.: Kinetics of iron complexation by dissolved natural organic matter in coastal waters, *Mar. Chem.*, 84, 85–103, 2003. 1282
- Sabine, C. L., Feely, R. A., Gruber, N., Key, R. M., Lee, K., Bullister, J. L., Wanninkhof, R., Wong, C. S., Wallace, D. W. R., Tilbrook, B., Millero, F. J., Peng, T. H., Kozyr, A., Ono, T., and Rios, A. F.: The oceanic sink for anthropogenic CO₂, *Science*, 305, 367–71, 2004. 1261
- Schulz, M., Prospero, J. M., Baker, A. R., Dentener, F., Ickes, L., Liss, P. S., Mahowald, N. M., Nickovic, S., García-Pando, C. P., Rodríguez, S., Sarin, M., Tegen, I., and Duce, R. A.: Atmospheric transport and deposition of mineral dust to the ocean: implications for research needs, *Environ. Sci. Technol.*, 46, 10390–10404, doi:10.1021/es300073u, 2012. 1305
- Semtner, A. J.: A model for the thermodynamic growth of sea ice in numerical investigation of climate, *J. Phys. Oceanogr.*, 6, 376–389, 1976. 1291
- Smith, S. L., Yamanaka, Y., Pahlow, M., and Oschlies, A.: Optimal uptake kinetics: physiological acclimation explains the pattern of nitrate uptake by phytoplankton in the ocean, *Mar. Ecol.-Prog. Ser.*, 384, 1–12, doi:10.3354/meps08022, 2009. 1296
- Steele, J. H. and Henderson, E. W.: The role of predation in plankton models, *J. Plankton Res.*, 14, 157–172, 1992. 1280
- Steinacher, M., Joos, F., Frölicher, T. L., Bopp, L., Cadule, P., Cocco, V., Doney, S. C., Gehlen, M., Lindsay, K., Moore, J. K., Schneider, B., and Segschneider, J.: Projected 21st century decrease in marine productivity: a multi-model analysis, *Biogeosciences*, 7, 979–1005, doi:10.5194/bg-7-979-2010, 2010. 1261
- Tagliabue, A., Bopp, L., Aumont, O., and Arrigo, K. R.: Influence of light and temperature on the marine iron cycle: from theoretical to global modeling, *Global Biogeochem. Cy.*, 23, GB2017, doi:10.1029/2008GB003214, 2009. 1306

A description of MEDUSA-2.0

A. Yool et al.

Title Page

Abstract

Introduction

Conclusions

References

Tables

Figures

◀

▶

◀

▶

Back

Close

Full Screen / Esc

Printer-friendly Version

Interactive Discussion



- Takahashi, T., Sutherland, S. C., Wanninkhof, R., Sweeney, C., Feely, R. A., Chipman, D. W., Hales, B., Friederich, G., Chavez, F., Sabine, C., Watson, A., Bakker, D. C. E., Schuster, U., Metzl, N., Yoshikawa–Inoue, H., Ishii, M., Midorikawa, T., Nojiri, Y., Kortzinger, A., Steinhoff, T., Hoppema, M., Olafsson, J., Arnarson, T. S., Tillbrook, B., Johannessen, T., Olsen, A., Bellerby, R., Wong, C. S., Delille, B., Bates, N. R., and de Baar, H. J. W.: Climatological mean and decade change in surface ocean $p\text{CO}_2$, and net sea–air CO_2 flux over the global oceans, *Deep-Sea Res. Pt. II*, 56, 554–577, doi:10.1016/j.dsr2.2008.12.009, 2009. 1294, 1298, 1306, 1350, 1351, 1352, 1353
- 5 Taylor, A. H., Geider, R. J., and Gilbert, F. J. H.: Seasonal and latitudinal dependencies of phytoplankton carbon-to-chlorophyll *a* ratios: results of a modelling study, *Mar. Ecol.-Prog. Ser.*, 152, 51–66, 1997. 1275
- Timmermann, R., Goosse, H., Madec, G., Fichefet, T., Etche, C., and Duliere, V.: On the representation of high latitude processes in the ORCA-LIM global coupled sea ice-ocean model, *Ocean Model.*, 8, 175–201, doi:10.1016/j.ocemod.2003.12.009, 2005. 1291
- 15 Tréguer, P., Nelson, D. M., Van Bennekom, A. J., DeMaster, D. J., Leynaert, A., and Quéguiner, B.: The silica balance in the world ocean: a reestimate, *Science*, 268, 375–379, 1995. 1300
- Tyrrell, T. and Taylor, A. H.: A modelling study of *Emiliania huxleyi* in the NE Atlantic, *J. Marine Syst.*, 9, 83–112, 1996. 1283, 1306
- 20 Volk, T. and Hoffert, M. I.: Ocean carbon pumps: analysis of relative strengths and efficiencies in ocean-driven atmospheric CO_2 changes, *Geoph. Monog. Series*, 32, 99–110, doi:10.1029/GM032p0099, 1985. 1261
- Weber, L., Völker, C., Oschlies, A., and Burchard, H.: Iron profiles and speciation of the upper water column at the Bermuda Atlantic Time-series Study site: a model based sensitivity study, *Biogeosciences*, 4, 689–706, doi:10.5194/bg-4-689-2007, 2007. 1306
- 25 Westberry, T., Behrenfeld, M. J., Siegel, D. A., and Boss, E.: Carbon-based primary productivity modeling with vertically resolved photoacclimation, *Global Biogeochem. Cy.*, 22, GB2024, doi:10.1029/2007GB003078, 2008. 1294, 1295, 1304
- Wilson, J. D., Barker, S., and Ridgwell, A.: Assessment of the spatial variability in particulate organic matter and mineral sinking fluxes in the ocean interior: Implications for the ballast hypothesis, *Global Biogeochem. Cy.*, 26, GB4011, doi:10.1029/2012GB004398, 2012. 1308
- 30

A description of MEDUSA-2.0

A. Yool et al.

Title Page

Abstract

Introduction

Conclusions

References

Tables

Figures

◀

▶

◀

▶

Back

Close

Full Screen / Esc

Printer-friendly Version

Interactive Discussion



Ye, Y., Völker, C., and Wolf-Gladrow, D. A.: A model of Fe speciation and biogeochemistry at the Tropical Eastern North Atlantic Time-Series Observatory site, *Biogeosciences*, 6, 2041–2061, doi:10.5194/bg-6-2041-2009, 2009. 1306

Yool, A. and Tyrrell, T.: The role of diatoms in regulating the ocean's silicon cycle, *Global Biogeochem. Cy.*, 17, 1103, doi:10.1029/2002GB002018, 2003. 1280

Yool, A., Oschlies, A., Nurser, A. J. G., and Gruber, N.: A model-based assessment of the TrOCA approach for estimating anthropogenic carbon in the ocean, *Biogeosciences*, 7, 723–751, doi:10.5194/bg-7-723-2010, 2010. 1283, 1291, 1293, 1306

Yool, A., Popova, E. E., and Anderson, T. R.: Medusa-1.0: a new intermediate complexity plankton ecosystem model for the global domain, *Geosci. Model Dev.*, 4, 381–417, doi:10.5194/gmd-4-381-2011, 2011. 1260, 1262, 1266, 1272, 1277, 1280, 1283, 1291, 1294, 1296, 1304, 1305, 1310

Yool, A., Popova, E. E., Coward, A. C., Bernie, D., and Anderson, T. R.: Climate change and ocean acidification impacts on lower trophic levels and the export of organic carbon to the deep ocean, *Biogeosciences Discuss.*, in press, 2013. 1307

Zahariev, K., Christian, J. R., and Denman, K. L.: Preindustrial, historical, and fertilization simulations using a global ocean carbon model with new parameterizations of iron limitation, calcification, and N₂ fixation, *Prog. Oceanogr.*, 77, 56–82, 2008. 1283, 1306

Zondervan, I., Zeebe, R. E., Rost, B., and Rieblesell, U.: Decreasing marine biogenic calcification: a negative feedback on rising atmospheric CO₂, *Global Biogeochem. Cy.*, 15, 507–516, doi:10.1029/2000GB001321, 2001. 1307

A description of
MEDUSA-2.0

A. Yool et al.

Title Page

Abstract

Introduction

Conclusions

References

Tables

Figures

I◀

▶I

◀

▶

Back

Close

Full Screen / Esc

Printer-friendly Version

Interactive Discussion

**Table 1.** Phytoplankton growth parameters.

ξ	Chl : N conversion factor (Redfield ratio of 6.625) g chl (mol N) ⁻¹	0.01257
α_{Pn}, α_{Pd}	chl-specific initial slope of $P-I$ curve g C (g chl) ⁻¹ (W m ⁻²) ⁻¹ d ⁻¹	15.0, 11.25
V_{Pn}, V_{Pd}	maximum phytoplankton growth rate d ⁻¹	0.53, 0.50
$\theta_{\max, Pn}^{\text{Chl}}, \theta_{\max, Pd}^{\text{Chl}}$	maximum chl : C ratio g chl (g C) ⁻¹	0.05, 0.05
$R_{\text{Si:N}}^0$	minimum diatom Si : N ratio mol Si (mol N) ⁻¹	0.2
$R_{\text{N:Si}}^0$	minimum diatom N : Si ratio mol N (mol Si) ⁻¹	0.2
U_{∞}	hypothetical growth ratio at ∞ Si : N ratio –	1.5
$k_{N, Pn}, k_{N, Pd}$	N nutrient uptake half-saturation constants mmol N m ⁻³	0.50, 0.75
k_{Si}	Si nutrient uptake half-saturation constant mmol Si m ⁻³	3.00
$k_{\text{Fe}, Pn}, k_{\text{Fe}, Pd}$	Fe nutrient uptake half-saturation constants $\mu\text{mol Fe m}^{-3}$	0.33, 0.67

A description of
MEDUSA-2.0

A. Yool et al.

Title Page

Abstract

Introduction

Conclusions

References

Tables

Figures

I◀

▶I

◀

▶

Back

Close

Full Screen / Esc

Printer-friendly Version

Interactive Discussion

**Table 2.** Zooplankton grazing parameters.

g_{μ}, g_m	maximum zooplankton grazing rate d^{-1}	2.0, 0.5
k_{μ}, k_m	zooplankton grazing half-saturation constants mmol N m^{-3}	0.8, 0.3
ϕ	zooplankton grazing inefficiency	0.20
	–	
β_N	zooplankton N assimilation efficiency	0.77
	–	
β_C	zooplankton C assimilation efficiency	0.64
	–	
k_C	zooplankton net C growth efficiency	0.80
	–	
$\rho_{\mu Pn}, \rho_{\mu D}$	microzooplankton grazing preferences	0.75, 0.25
	–	
$\rho_{mPn}, \rho_{mPd},$ $\rho_{mZ\mu}, \rho_{mD}$	mesozooplankton grazing preferences	0.15, 0.35, 0.35, 0.15
	–	

A description of
MEDUSA-2.0

A. Yool et al.

Title Page

Abstract

Introduction

Conclusions

References

Tables

Figures

I ◀

▶ I

◀

▶

Back

Close

Full Screen / Esc

Printer-friendly Version

Interactive Discussion

**Table 3.** Plankton and detritus loss parameters.

$\mu_{1,Pn}, \mu_{1,Pd}$	phytoplankton loss rates d^{-1}	0.02, 0.02
$\mu_{1,Z\mu}, \mu_{1,Zm}$	zooplankton loss rates d^{-1}	0.02, 0.02
$\mu_{2,Pn}, \mu_{2,Pd}$	phytoplankton maximum loss rates d^{-1}	0.1, 0.1
$k_{Z\mu}, k_{Zm}$	phytoplankton loss half-saturation constants $mmol\ N\ m^{-3}$	0.5, 0.5
$\mu_{2,Z\mu}, \mu_{2,Zm}$	zooplankton maximum loss rates d^{-1}	0.1, 0.2
$k_{Z\mu}, k_{Zm}$	zooplankton loss half-saturation constants $mmol\ N\ m^{-3}$	0.5, 0.75
μ_D	detrital N remineralisation rate d^{-1}	0.0158
μ_D	detrital C remineralisation rate d^{-1}	0.0127

Table 4. Miscellaneous parameters.

θ_{Pn}, θ_{Pd}	phytoplankton C : N ratio mol C (mol N) ⁻¹	6.625
$\theta_{Z\mu}, \theta_{Zm}$	zooplankton C : N ratio mol C (mol N) ⁻¹	5.625
θ_D	detritus C : N ratio mol C (mol N) ⁻¹	6.625
R_{Fe}	phytoplankton Fe : N uptake ratio $\mu\text{mol Fe (mol N)}^{-1} \text{ m}$	30.0
L_{total}	total ligand concentration $\mu\text{mol m}^{-3}$	1.0
k_{FeL}	dissociation constant for (Fe + ligand)	100.0
k_{scav}	scavenging rate of “free” Fe d^{-1}	0.001
Diss	diatom frustule dissolution rate d^{-1}	0.006
w_g	detrital sinking rate m d^{-1}	2.5
θ_{phy}	phytoplankton O ₂ : N ratio mol O ₂ (mol N) ⁻¹	9.4375
θ_{zoo}	zooplankton O ₂ : N ratio mol O ₂ (mol N) ⁻¹	8.3149
θ_{nit}	O ₂ consumption by N remineralisation mol O ₂ (mol N) ⁻¹	2.0
θ_{rem}	O ₂ consumption by C remineralisation mol O ₂ (mol C) ⁻¹	1.1226
O_{min}	minimum O ₂ concentration mmol O ₂ m ⁻³	4.0

A description of MEDUSA-2.0

A. Yool et al.

Title Page

Abstract

Introduction

Conclusions

References

Tables

Figures

◀

▶

◀

▶

Back

Close

Full Screen / Esc

Printer-friendly Version

Interactive Discussion



Table 5. Fast detritus submodel parameters.

$D1_{frac}$	fast detritus fraction of diatom losses –	0.33
$D2_{frac}$	fast detritus fraction of mesozooplankton losses –	1.00
$D3_{frac}$	fast detritus fraction of mesozooplankton grazing –	0.80
r_0	Ridgwell et al. (2007) $CaCO_3$: POC: export rain ratio scalar –	0.026
η	Ridgwell et al. (2007) thermodynamic calcification rate power –	0.81
M_{org}	organic carbon mass : mole ratio, C $g (mol C)^{-1}$	12.011
M_{CaCO_3}	calcium carbonate mass : mole ratio, $CaCO_3$ $g (mol C)^{-1}$	100.086
M_{Si}	biogenic Si mass : mole ratio, SiO_2 $g (mol Si)^{-1}$	60.084
f_{CaCO_3}	calcium carbonate protection ratio $g C (g C)^{-1}$	0.070
f_{Si}	biogenic Si protection ratio $g C (g Si)^{-1}$	0.026
d_{excess}	excess organic carbon dissolution length scale m	188
d_{CaCO_3}	calcium carbonate dissolution length scale m	3500
d_{Si}	biogenic Si dissolution length scale m	2000
λ_N	benthic N remineralisation rate d^{-1}	0.05
λ_{Si}	benthic Si dissolution rate d^{-1}	0.01
λ_C	benthic C remineralisation rate d^{-1}	0.05
λ_{Ca}	benthic $CaCO_3$ dissolution rate d^{-1}	0.01

A description of
MEDUSA-2.0

A. Yool et al.

Title Page

Abstract

Introduction

Conclusions

References

Tables

Figures

I◀

▶I

◀

▶

Back

Close

Full Screen / Esc

Printer-friendly Version

Interactive Discussion

**Table 6.** MEDUSA-2.0 switches.

jphy	switches phytoplankton maximum growth between temperature independence (= 0) and dependence (= 1); the default is $j_{phy} = 1$
jmpn	switches non-diatom phytoplankton density-dependent mortality between linear (= 1), quadratic (= 2), hyperbolic (= 3) and sigmoid (= 4) forms; the default is $jmpn = 3$
jmpd	as $jmpn$ but for diatom phytoplankton
jmzmi	as $jmpn$ but for microzooplankton
jmzme	as $jmpn$ but for mesozooplankton
jmd	as $jphy$ but for detrital remineralisation; the default is $jmd = 1$
jliebig	switches between multiplicative (= 0) and Liebig (= 1) phytoplankton nutrient limitation; the default is $jliebig = 0$
jexport	switches between ballast (= 1), Martin et al. (1987) (= 2) and Henson et al. (2011) (= 3) export submodels; the default is $jexport = 1$
jrratio	switches between MEDUSA-1.0 (= 0), surface $\Omega_{calcite}$ (= 1) and local $\Omega_{calcite}$ (= 2) $CaCO_3$ production; the default is $jrratio = 2$
jocalccd	switches between specified lysocline (= 0; MEDUSA-1.0) and one calculated from $\Omega_{calcite}$ (= 1); the default is $jocalccd = 1$

A description of
MEDUSA-2.0

A. Yool et al.

Title Page

Abstract

Introduction

Conclusions

References

Tables

Figures

◀

▶

◀

▶

Back

Close

Full Screen / Esc

Printer-friendly Version

Interactive Discussion



Table 7. Mean annual (2000–2004) surface concentrations of MEDUSA-1.0 (**upper row**) and MEDUSA-2.0 (**lower row**) tracers for. All concentrations are in mmol m^{-3} , except Fe which is in $\mu\text{mol m}^{-3}$.

Field	World	Atlantic	Pacific	Indian	Southern	Arctic
Pn	0.2589	0.2449	0.2821	0.2796	0.2228	0.1363
	0.2484	0.1931	0.3024	0.2061	0.2403	0.1632
Pd	0.1100	0.1076	0.1027	0.1276	0.1261	0.0646
	0.1017	0.0886	0.1051	0.0780	0.1346	0.1104
Z μ	0.1391	0.1269	0.1523	0.1567	0.1170	0.0767
	0.1361	0.0929	0.1715	0.1064	0.1372	0.1069
Zm	0.1643	0.1575	0.1928	0.1869	0.0984	0.0440
	0.1691	0.1320	0.2233	0.1108	0.1461	0.1082
DIN	6.0084	2.0798	2.3835	2.3214	26.4194	2.3620
	6.5577	1.7054	4.1569	1.5622	25.8858	4.3875
Si	10.6727	1.3420	1.8965	2.2839	57.4320	9.5829
	11.2299	2.5587	1.3104	2.6514	62.0107	2.8387
Fe	0.5059	0.7179	0.3759	0.6497	0.3732	0.7301
	0.5354	0.9454	0.2791	0.7427	0.3599	0.9050

A description of
MEDUSA-2.0

A. Yool et al.

Table 8. Mean annual (2000–2004) biogeochemical properties in MEDUSA-1.0 (**upper row**) and MEDUSA-2.0 (**lower row**). Units indicated for each property.

Field	World	Atlantic	Pacific	Indian	Southern	Arctic
(Pn + Pd) Gt C	0.8413 0.7968	0.1909 0.1636	0.3402 0.3472	0.1619 0.1311	0.1397 0.1444	0.0085 0.0104
TPP GtCyr ⁻¹	45.3024 41.6278	9.8854 7.9429	20.6498 21.0785	9.1584 5.9938	5.2567 6.0846	0.3521 0.5235
Pd fraction %	16.2971 15.8900	16.7576 18.7965	14.1766 13.0309	16.4800 14.4124	23.1119 22.5187	21.2283 26.9237
ML fraction %	73.4297 67.3252	66.8833 58.7899	74.4158 67.9296	69.6741 58.2734	89.6516 85.8437	54.8974 60.8860
Opal Tmol Si yr ⁻³	221.1951 193.9731	39.7958 34.3463	76.6536 66.7915	42.5510 24.3439	59.6807 67.0384	2.5142 1.4530
CaCO ₃ GtCyr ⁻¹	0.5952 0.4092	0.1222 0.0860	0.3032 0.2248	0.1269 0.0553	0.0411 0.0399	0.0018 0.0031
Rain ratio %	7.5702 6.4065	7.0905 6.5353	8.1046 6.6294	8.1189 7.5332	5.2348 4.6307	3.6604 3.7528
D, 100 m GtCyr ⁻¹	8.1505 8.1274	1.7183 1.5883	3.6140 3.9629	1.5491 1.0937	1.2007 1.3828	0.0683 0.0996
D, 1000 m GtCyr ⁻¹	0.4312 0.3575	0.0739 0.0676	0.2075 0.1754	0.0909 0.0492	0.0580 0.0638	0.0008 0.0014

Title Page

Abstract

Introduction

Conclusions

References

Tables

Figures

I◀

▶I

◀

▶

Back

Close

Full Screen / Esc

Printer-friendly Version

Interactive Discussion



A description of MEDUSA-2.0

A. Yool et al.

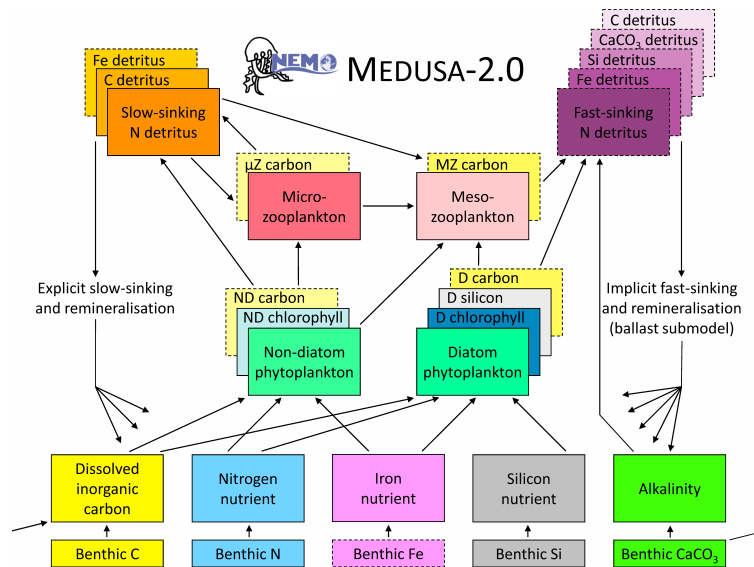


Fig. 1. Schematic diagram of the components and interactions in the MEDUSA-2.0 model. Boxes with solid borders indicate explicitly modelled state variables, while boxes with dashed borders indicate implicitly modelled components. Overlapping boxes indicate components for which multiple currencies are modelled (e.g. different elements, chlorophyll). The smaller boxes at the bottom of the diagram refer to benthic reservoirs of model currencies that are fed by sinking detrital material (slow- and fast-sinking). For reasons of diagrammatic clarity, dissolved oxygen and its connections to other state variables are omitted here. Note that the dissolution of benthic CaCO_3 releases both DIC and alkalinity.

A description of
MEDUSA-2.0

A. Yool et al.

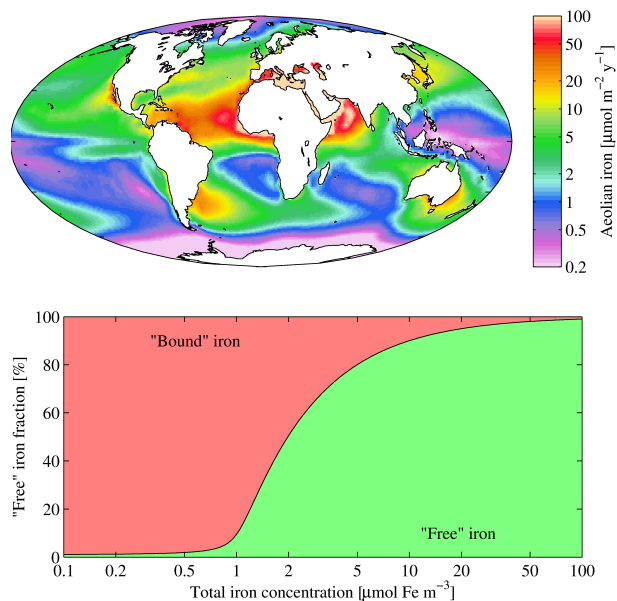


Fig. 2. The top panel shows mean annual aeolian iron input to the ocean (i.e. the quantity of iron that dissolves into seawater from deposited dust). The input is shown on a logarithmic scale in units of $\mu\text{mol m}^{-2} \text{yr}^{-1}$, and integrated input is $2.564 \text{ Gmol Fe yr}^{-1}$. The bottom panel shows the fractionation of total iron between “free” and ligand-bound forms across a logarithmic range of total iron concentrations.

[Title Page](#)[Abstract](#)[Introduction](#)[Conclusions](#)[References](#)[Tables](#)[Figures](#)[◀](#)[▶](#)[◀](#)[▶](#)[Back](#)[Close](#)[Full Screen / Esc](#)[Printer-friendly Version](#)[Interactive Discussion](#)

A description of
MEDUSA-2.0

A. Yool et al.

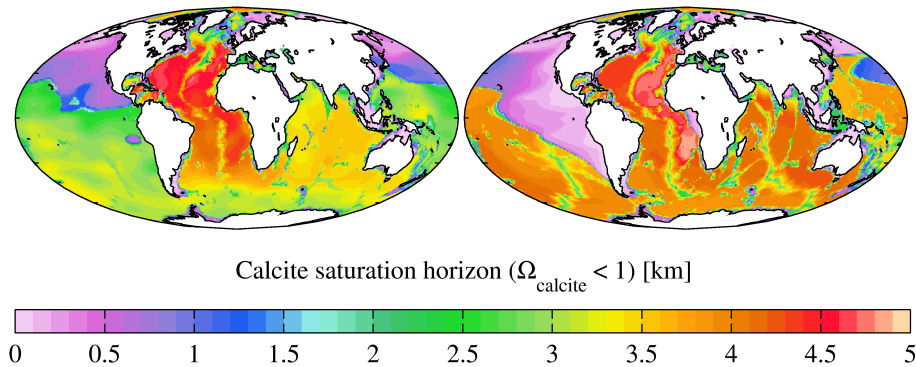


Fig. 3. Calcite compensation depth (CCD) in MEDUSA-1.0 (observationally-derived; left) and MEDUSA-2.0 (simulated; right). CCD is defined here as the depth at which carbonate ion concentration falls below the local saturation concentration, that is, where Ω_{calcite} falls below a value of 1.

[Title Page](#)[Abstract](#)[Introduction](#)[Conclusions](#)[References](#)[Tables](#)[Figures](#)[I◀](#)[▶I](#)[◀](#)[▶](#)[Back](#)[Close](#)[Full Screen / Esc](#)[Printer-friendly Version](#)[Interactive Discussion](#)

A description of
MEDUSA-2.0

A. Yool et al.

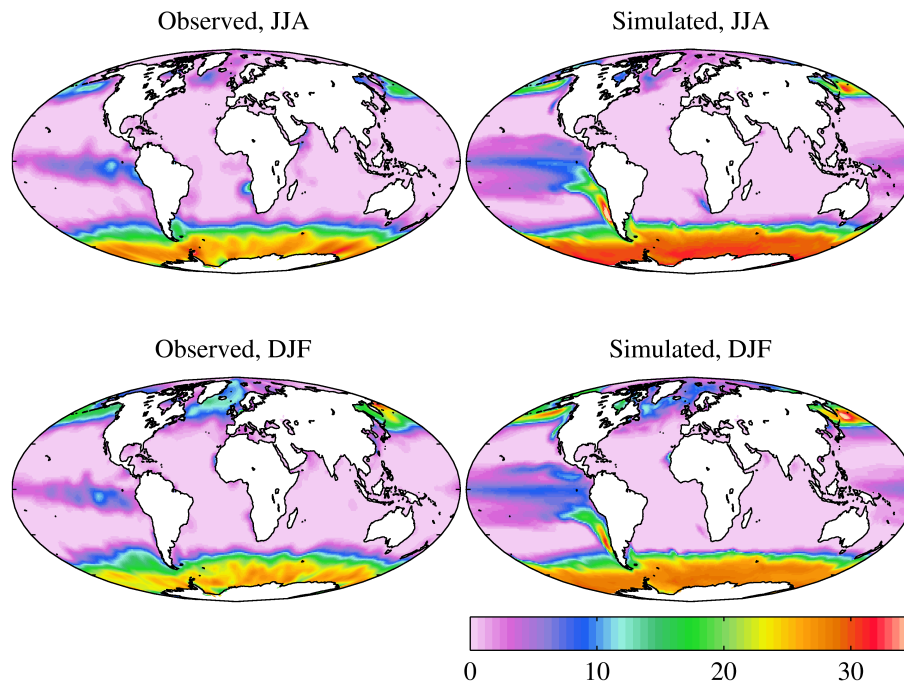


Fig. 4. Observational (World Ocean Atlas, 2009; left) and simulated (right) surface dissolved inorganic nitrogen for northern summer (June–July–August; top) and northern winter (December–January–February; bottom). Concentrations in mmol m^{-3} .

Title Page

Abstract

Introduction

Conclusions

References

Tables

Figures

◀

▶

◀

▶

Back

Close

Full Screen / Esc

Printer-friendly Version

Interactive Discussion



A description of
MEDUSA-2.0

A. Yool et al.

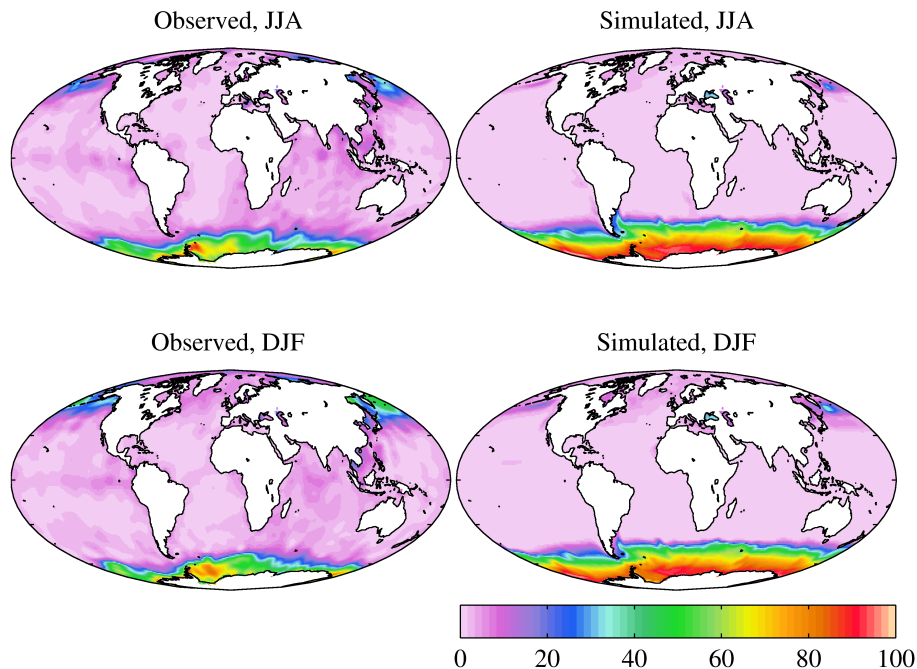


Fig. 5. Observational (World Ocean Atlas, 2009; left) and simulated (right) surface silicic acid for northern summer (June–July–August; top) and northern winter (December–January–February; bottom). Concentrations in mmol m^{-3} .

[Title Page](#)[Abstract](#)[Introduction](#)[Conclusions](#)[References](#)[Tables](#)[Figures](#)[◀](#)[▶](#)[◀](#)[▶](#)[Back](#)[Close](#)[Full Screen / Esc](#)[Printer-friendly Version](#)[Interactive Discussion](#)

A description of MEDUSA-2.0

A. Yool et al.

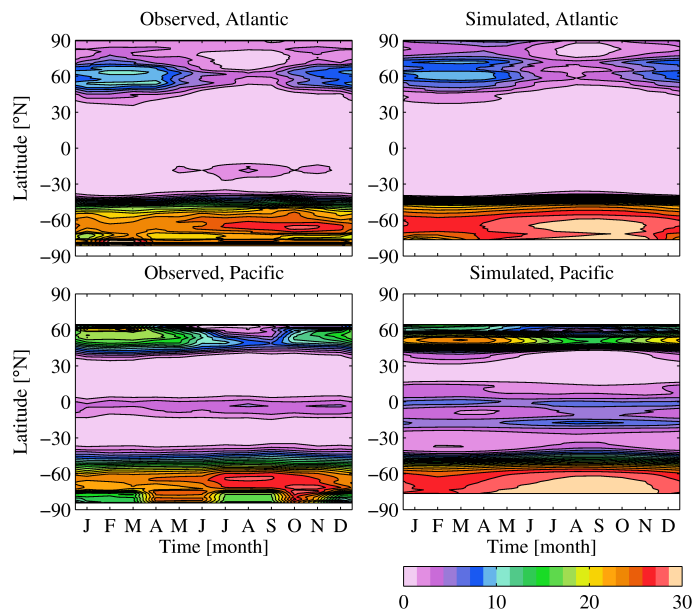


Fig. 6. Hovmöller diagrams of observational (World Ocean Atlas, 2009; left) and simulated (right) monthly surface dissolved inorganic nitrogen, averaged zonally for the Atlantic (top) and Pacific (bottom) basins. Concentrations in mmol N m^{-3} .

Title Page

Abstract

Introduction

Conclusions

References

Tables

Figures

◀

▶

◀

▶

Back

Close

Full Screen / Esc

Printer-friendly Version

Interactive Discussion



A description of
MEDUSA-2.0

A. Yool et al.

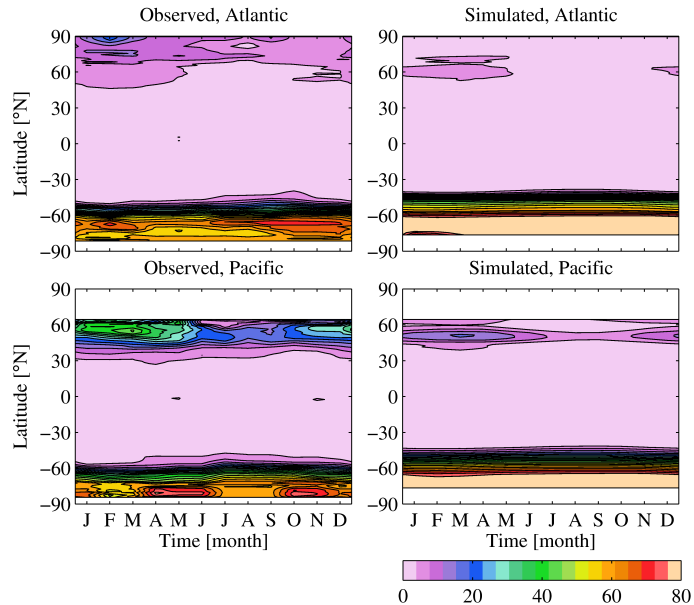


Fig. 7. Hovmöller diagrams of observational (World Ocean Atlas, 2009; left) and simulated (right) monthly surface silicic acid, averaged zonally for the Atlantic (top) and Pacific (bottom) basins. Concentrations in mmol Si m^{-3} .

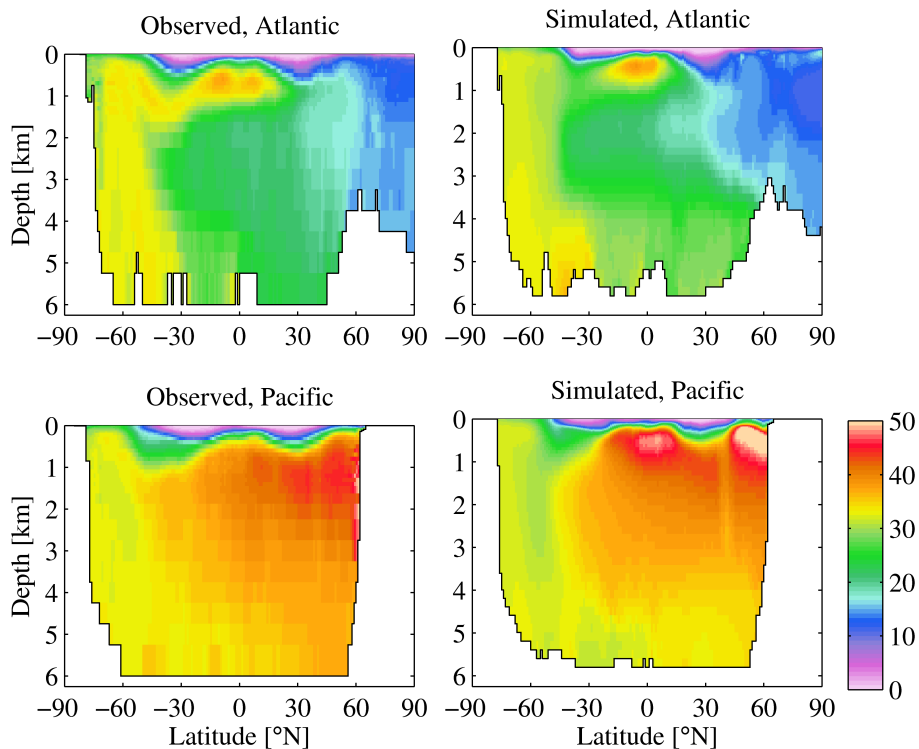


Fig. 8. Intercomparison of observational (left) and model (right) fields of zonally averaged dissolved inorganic nitrogen for the Atlantic (top) and Pacific (bottom) basins. Concentrations in mmolN m^{-3} .

A description of
MEDUSA-2.0

A. Yool et al.

Title Page

Abstract

Introduction

Conclusions

References

Tables

Figures

◀

▶

◀

▶

Back

Close

Full Screen / Esc

Printer-friendly Version

Interactive Discussion

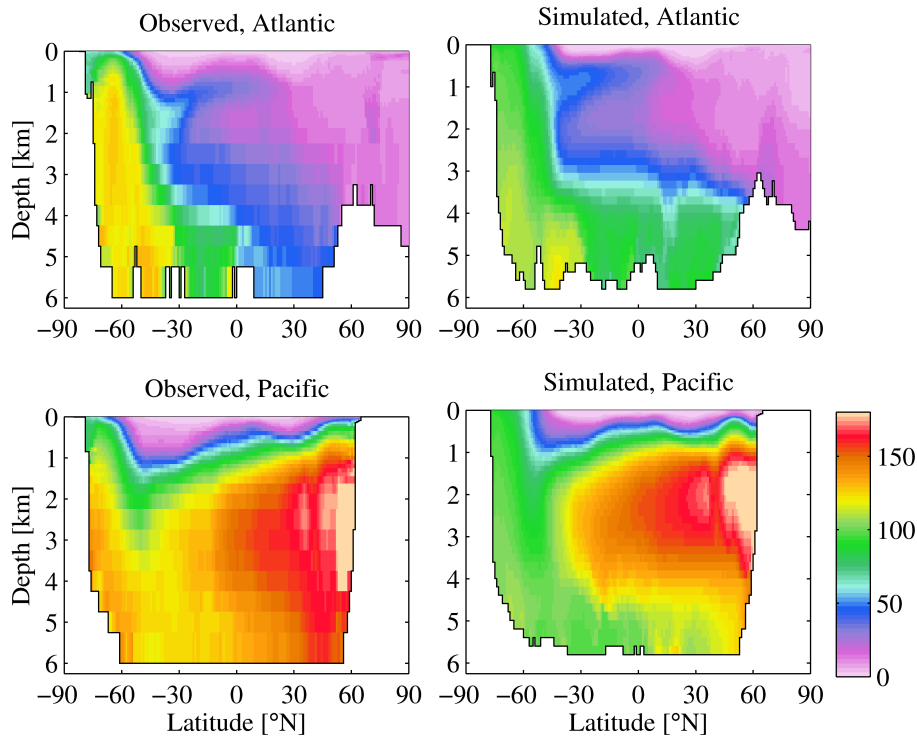


Fig. 9. Intercomparison of observational (left) and model (right) fields of zonally averaged silicic acid for the Atlantic (top) and Pacific (bottom) basins. Concentrations in mmol Sim^{-3} .

A description of
MEDUSA-2.0

A. Yool et al.

Title Page

Abstract

Introduction

Conclusions

References

Tables

Figures

◀

▶

◀

▶

Back

Close

Full Screen / Esc

Printer-friendly Version

Interactive Discussion

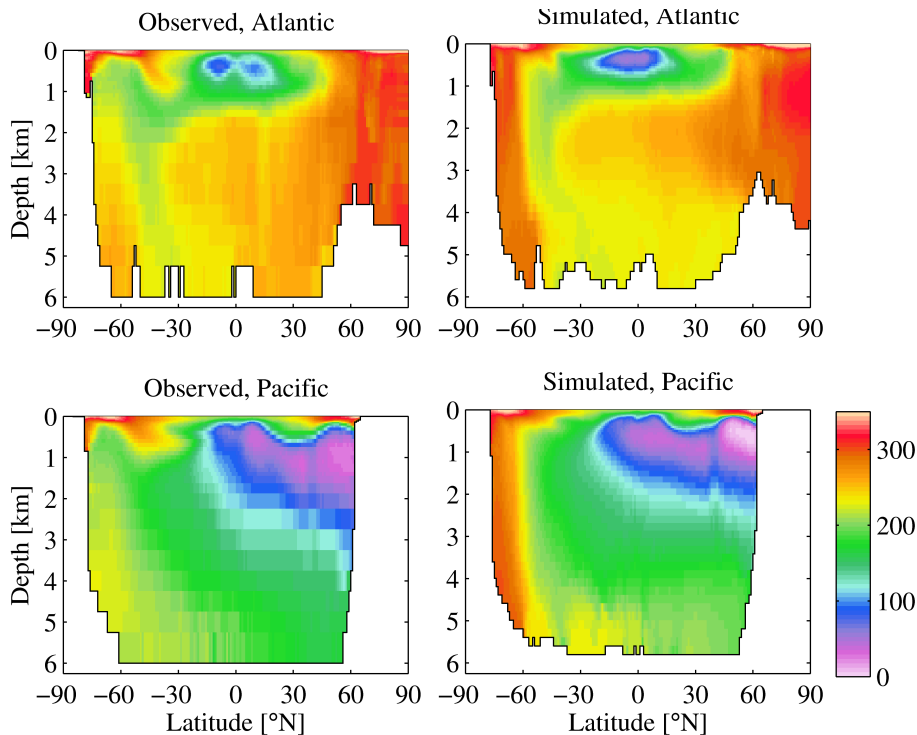


Fig. 10. Intercomparison of observational (left) and model (right) fields of zonally averaged dissolved oxygen for the Atlantic (top) and Pacific (bottom) basins. Concentrations in $\text{mmol O}_2 \text{m}^{-3}$.

A description of
MEDUSA-2.0

A. Yool et al.

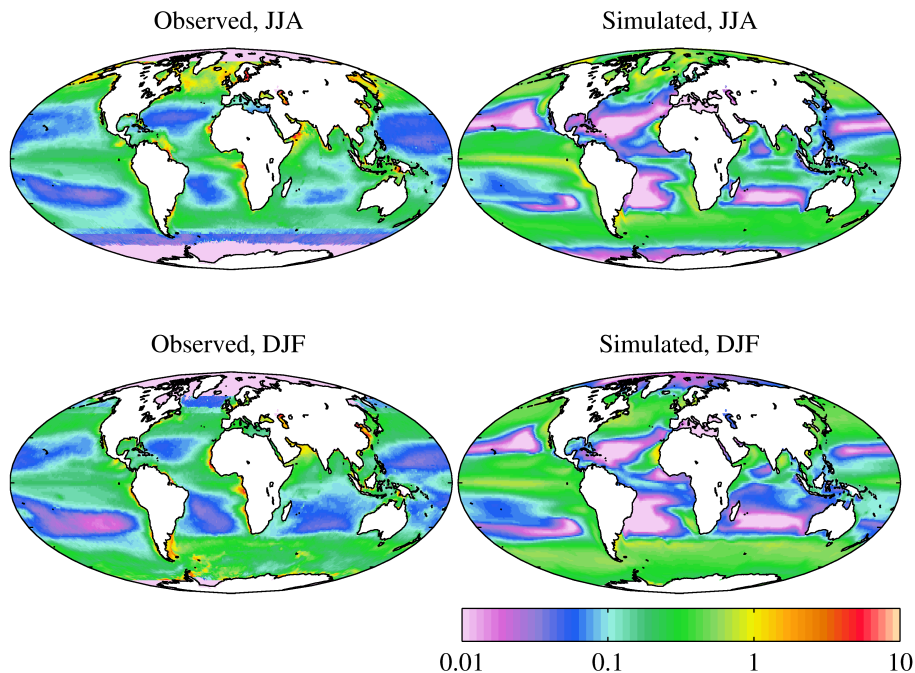


Fig. 11. Observational (SeaWiFS; left) and simulated (right) surface chlorophyll for northern summer (June–July–August; top) and northern winter (December–January–February; bottom). Concentrations in mg chl m^{-3} .

[Title Page](#)[Abstract](#)[Introduction](#)[Conclusions](#)[References](#)[Tables](#)[Figures](#)[◀](#)[▶](#)[◀](#)[▶](#)[Back](#)[Close](#)[Full Screen / Esc](#)[Printer-friendly Version](#)[Interactive Discussion](#)

A description of MEDUSA-2.0

A. Yool et al.

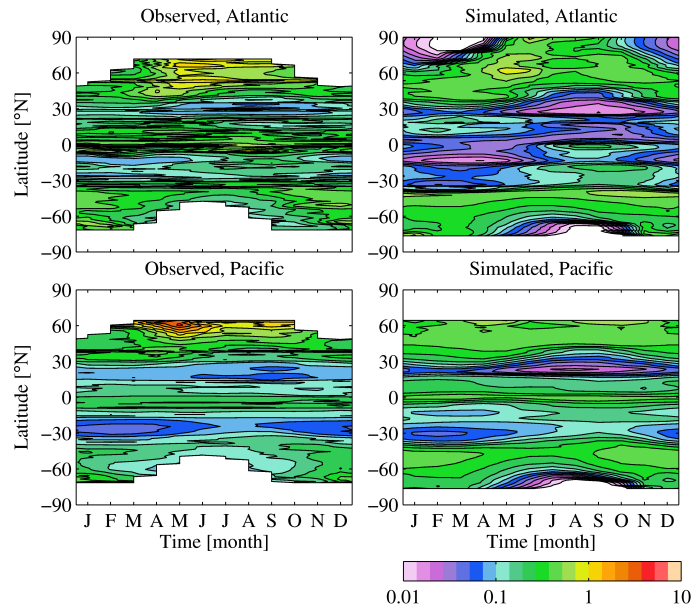


Fig. 12. Hovmöller diagrams of observational (SeaWiFS; left) and simulated (right) monthly surface chlorophyll, averaged zonally for the Atlantic (top) and Pacific (bottom) basins. Concentrations in mg chl m^{-3} .

[Title Page](#)
[Abstract](#)
[Introduction](#)
[Conclusions](#)
[References](#)
[Tables](#)
[Figures](#)
[⏪](#)
[⏩](#)
[◀](#)
[▶](#)
[Back](#)
[Close](#)
[Full Screen / Esc](#)
[Printer-friendly Version](#)
[Interactive Discussion](#)


**A description of
MEDUSA-2.0**

A. Yool et al.

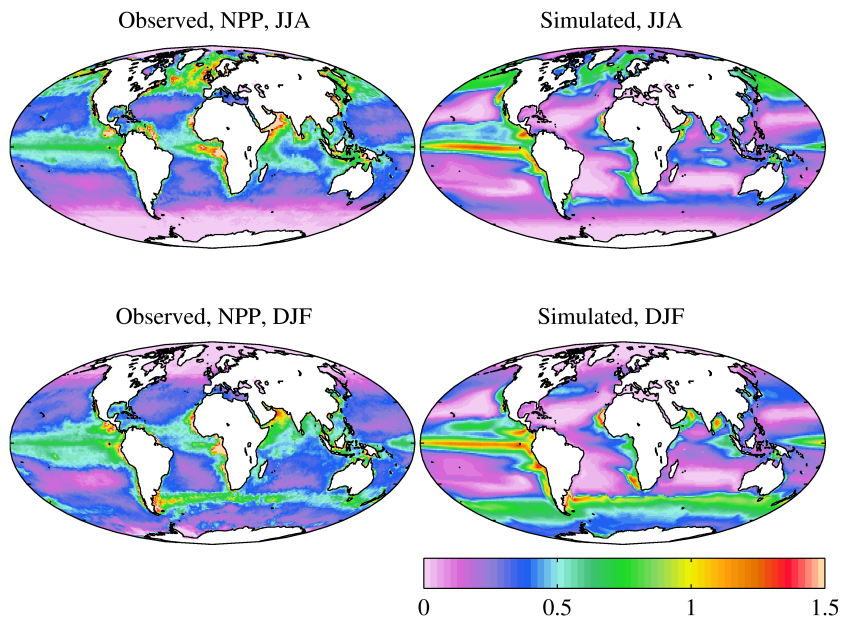


Fig. 13. Observational (left) and simulated (right) integrated primary production for northern summer (June–July–August; top) and northern winter (December–January–February; bottom). The observational field shown here is an average of the VGPM, Eppley-VGPM and CbPM estimates. Production in $\text{g C m}^{-2} \text{d}^{-1}$.

[Title Page](#)[Abstract](#)[Introduction](#)[Conclusions](#)[References](#)[Tables](#)[Figures](#)[◀](#)[▶](#)[◀](#)[▶](#)[Back](#)[Close](#)[Full Screen / Esc](#)[Printer-friendly Version](#)[Interactive Discussion](#)

**A description of
MEDUSA-2.0**

A. Yool et al.

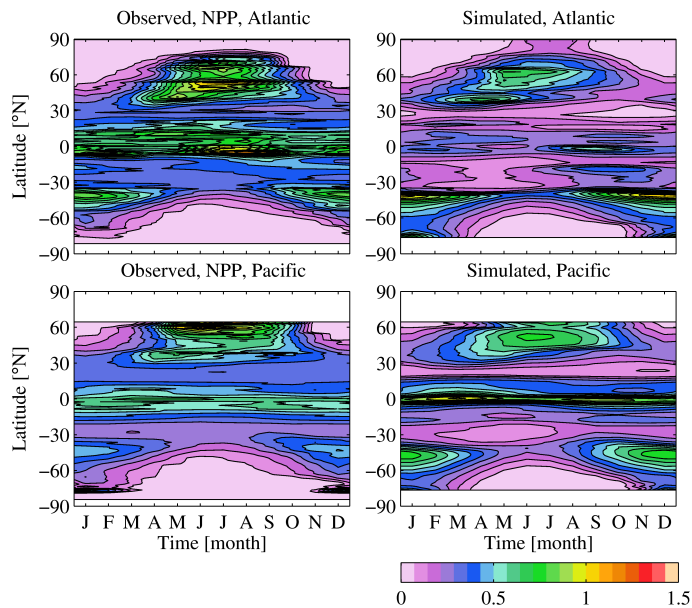


Fig. 14. Hovmöller diagrams of observational (left) and simulated (right) monthly integrated primary production, averaged zonally for the Atlantic (top) and Pacific (bottom) basins. Production in $\text{gC m}^{-2} \text{d}^{-1}$.

[Title Page](#)[Abstract](#)[Introduction](#)[Conclusions](#)[References](#)[Tables](#)[Figures](#)[◀](#)[▶](#)[◀](#)[▶](#)[Back](#)[Close](#)[Full Screen / Esc](#)[Printer-friendly Version](#)[Interactive Discussion](#)

A description of
MEDUSA-2.0

A. Yool et al.

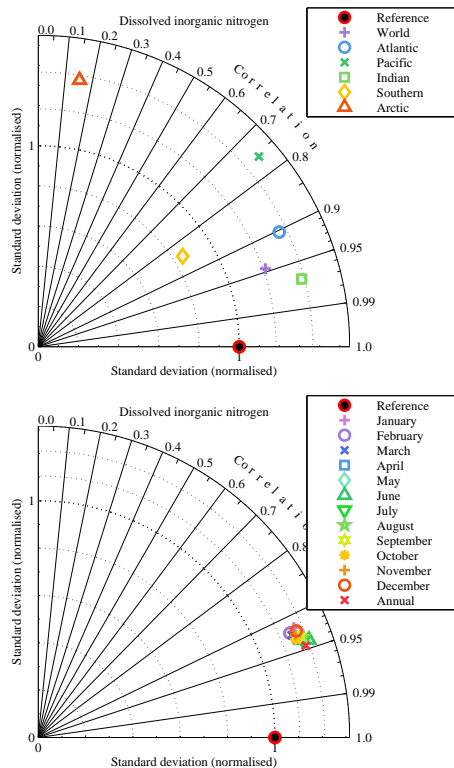


Fig. 15. Taylor diagrams of spatial (top) and temporal (bottom) model-observation comparisons for surface dissolved inorganic nitrogen. In the upper panel, simulated annual means for different regions are compared to corresponding observational fields. In the lower panel, simulated global average means for different months are compared to corresponding observational fields.

A description of
MEDUSA-2.0

A. Yool et al.

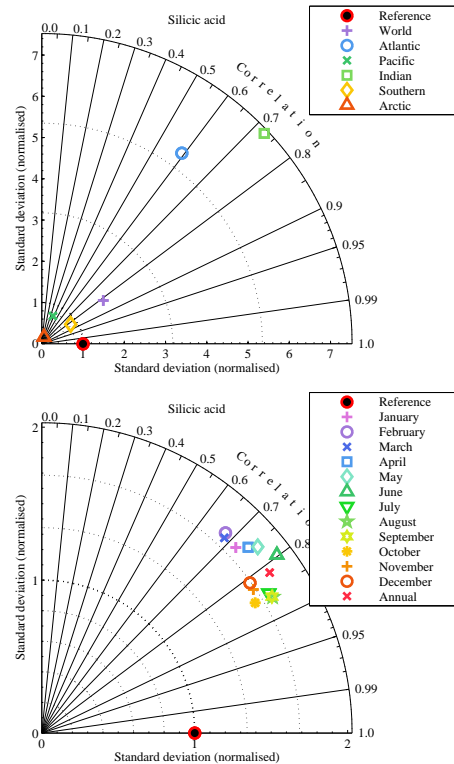


Fig. 16. Taylor diagrams of spatial (top) and temporal (bottom) model-observation comparisons for surface silicic acid. In the upper panel, simulated annual means for different regions are compared to corresponding observational fields. In the lower panel, simulated global average means for different months are compared to corresponding observational fields.

A description of
MEDUSA-2.0

A. Yool et al.

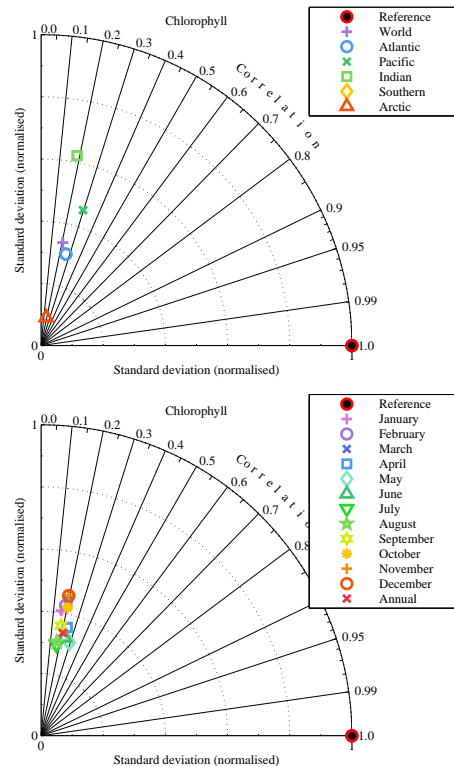


Fig. 17. Taylor diagrams of spatial (top) and temporal (bottom) model-observation comparisons for surface chlorophyll. In the upper panel, simulated annual means for different regions are compared to corresponding observational fields. In the lower panel, simulated global average means for different months are compared to corresponding observational fields.

A description of
MEDUSA-2.0

A. Yool et al.

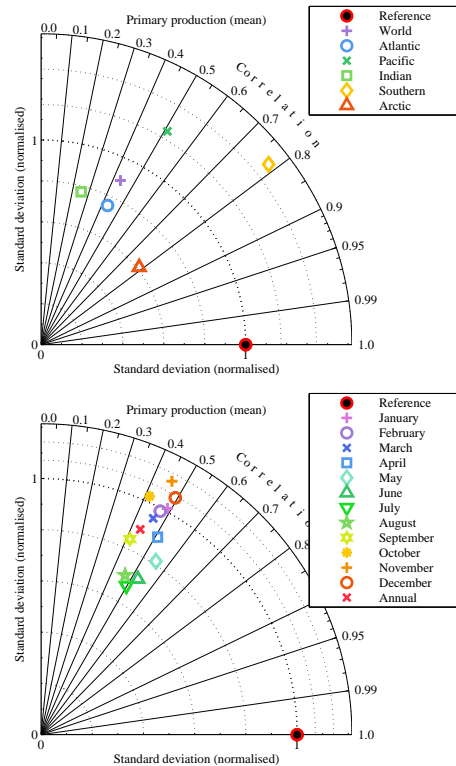


Fig. 18. Taylor diagrams of spatial (top) and temporal (bottom) model-observation comparisons for integrated primary production (VGPM estimated). In the upper panel, simulated annual means for different regions are compared to corresponding observational fields. In the lower panel, simulated global average means for different months are compared to corresponding observational fields.

A description of
MEDUSA-2.0

A. Yool et al.

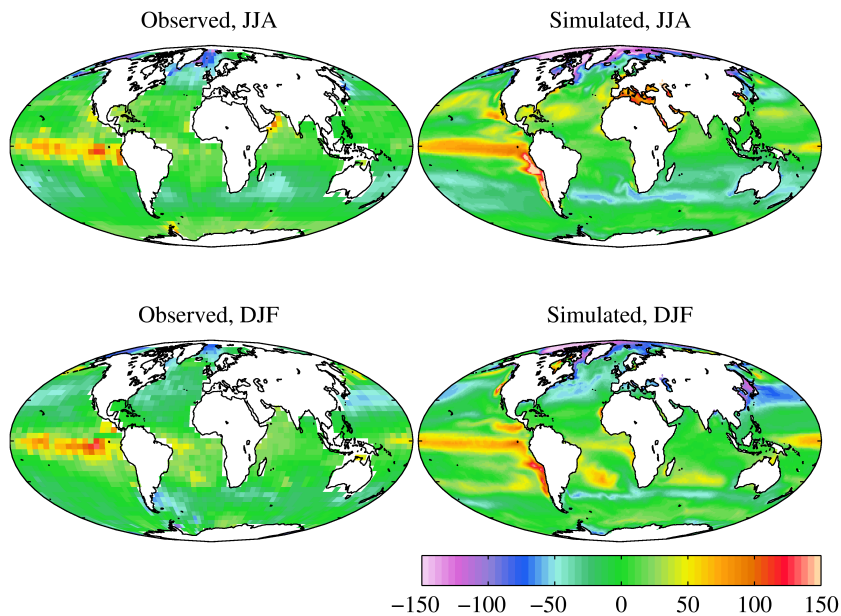


Fig. 19. Observational (Takahashi et al., 2009; left) and simulated (right) surface $\Delta p\text{CO}_2$ for northern summer (June-July-August; top) and northern winter (December-January-February; bottom). $\Delta p\text{CO}_2$ in ppm.

[Title Page](#)[Abstract](#)[Introduction](#)[Conclusions](#)[References](#)[Tables](#)[Figures](#)[◀](#)[▶](#)[◀](#)[▶](#)[Back](#)[Close](#)[Full Screen / Esc](#)[Printer-friendly Version](#)[Interactive Discussion](#)

A description of
MEDUSA-2.0

A. Yool et al.

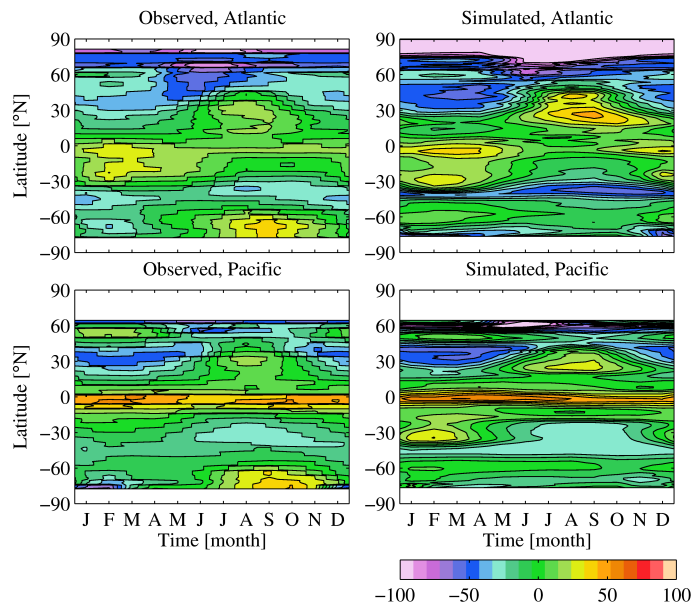


Fig. 20. Hovmöller diagrams of observational (Takahashi et al., 2009; left) and simulated (right) monthly $\Delta p\text{CO}_2$, averaged zonally for the Atlantic (top) and Pacific (bottom) basins. $\Delta p\text{CO}_2$ in ppm.

[Title Page](#)[Abstract](#)[Introduction](#)[Conclusions](#)[References](#)[Tables](#)[Figures](#)[◀](#)[▶](#)[◀](#)[▶](#)[Back](#)[Close](#)[Full Screen / Esc](#)[Printer-friendly Version](#)[Interactive Discussion](#)

A description of
MEDUSA-2.0

A. Yool et al.

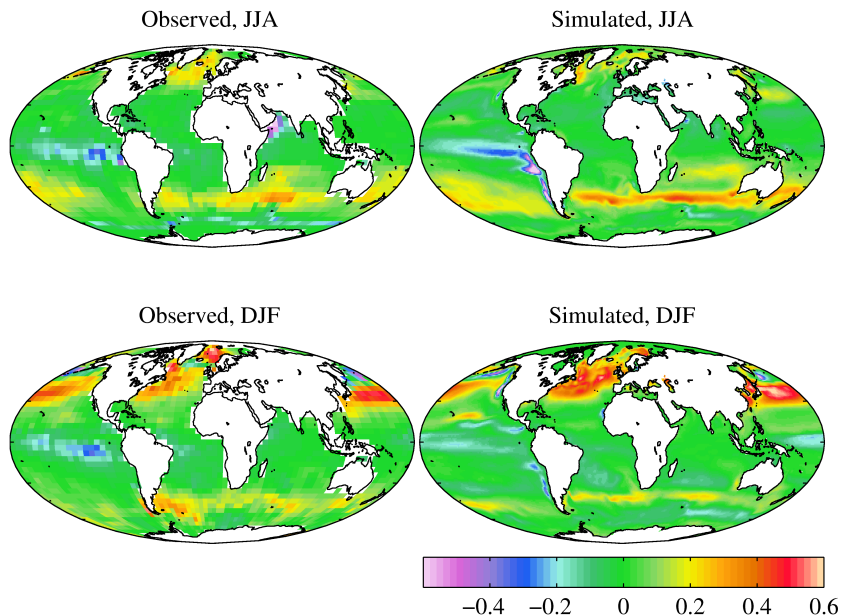


Fig. 21. Observational (Takahashi et al., 2009; left) and simulated (right) air–sea CO₂ flux for northern summer (June–July–August; top) and northern winter (December–January–February; bottom). Air–sea CO₂ flux in mol C m⁻² month⁻¹.

[Title Page](#)[Abstract](#)[Introduction](#)[Conclusions](#)[References](#)[Tables](#)[Figures](#)[⏪](#)[⏩](#)[◀](#)[▶](#)[Back](#)[Close](#)[Full Screen / Esc](#)[Printer-friendly Version](#)[Interactive Discussion](#)

A description of
MEDUSA-2.0

A. Yool et al.

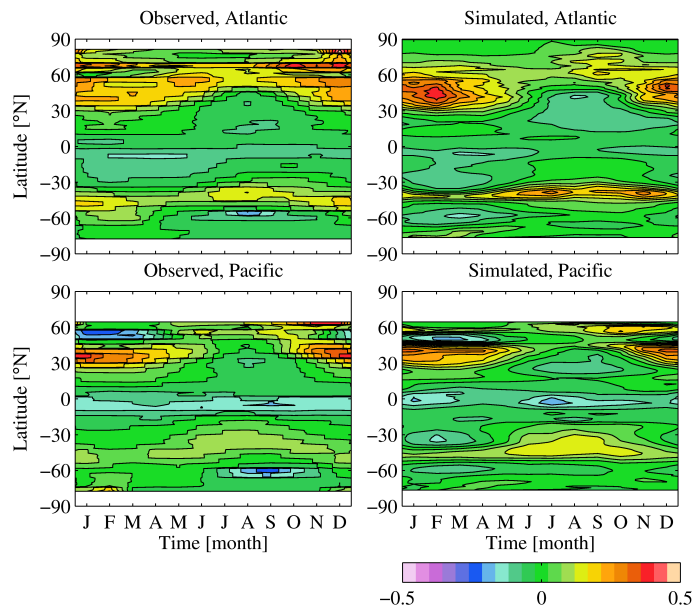


Fig. 22. Hovmöller diagrams of observational (Takahashi et al., 2009; left) and simulated (right) monthly air–sea CO₂ flux, averaged zonally for the Atlantic (top) and Pacific (bottom) basins. Air–sea CO₂ flux in mol C m⁻² month⁻¹.

[Title Page](#)[Abstract](#)[Introduction](#)[Conclusions](#)[References](#)[Tables](#)[Figures](#)[◀](#)[▶](#)[◀](#)[▶](#)[Back](#)[Close](#)[Full Screen / Esc](#)[Printer-friendly Version](#)[Interactive Discussion](#)

**A description of
MEDUSA-2.0**

A. Yool et al.

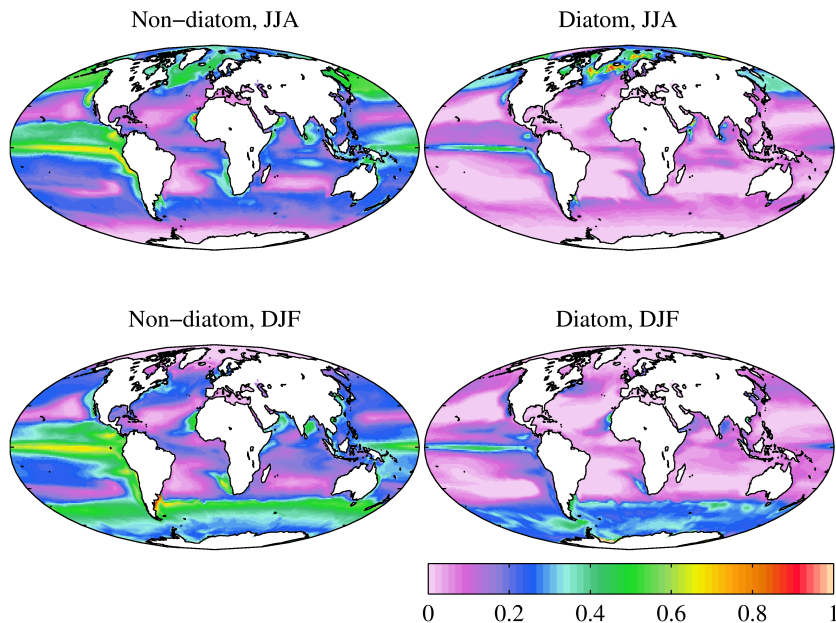


Fig. 23. Simulated surface non-diatom phytoplankton (left) and diatom phytoplankton (right) concentrations for northern summer (June–July–August; top) and northern winter (December–January–February; bottom). Concentrations in mmol m^{-3} .

[Title Page](#)[Abstract](#)[Introduction](#)[Conclusions](#)[References](#)[Tables](#)[Figures](#)[⏪](#)[⏩](#)[◀](#)[▶](#)[Back](#)[Close](#)[Full Screen / Esc](#)[Printer-friendly Version](#)[Interactive Discussion](#)

A description of
MEDUSA-2.0

A. Yool et al.

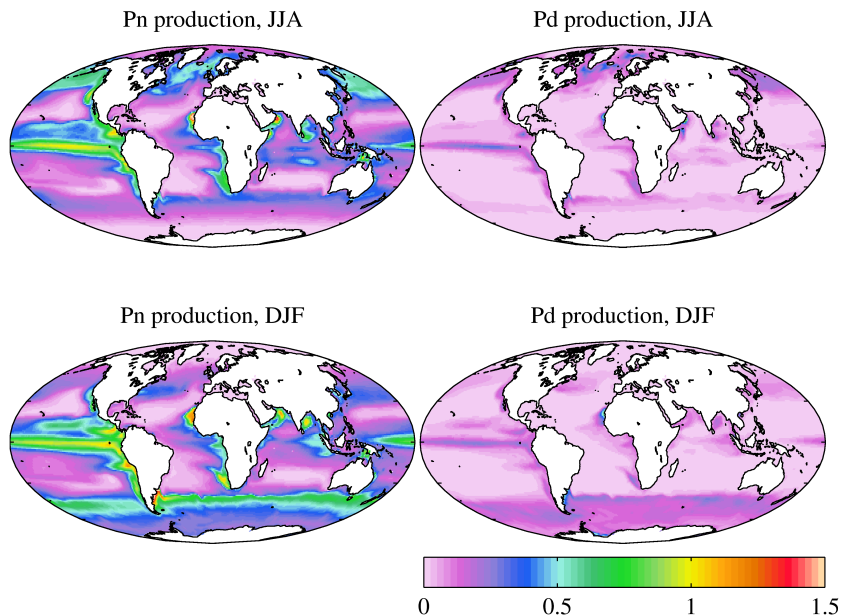


Fig. 24. Simulated non-diatom (left) and diatom (right) primary production for northern summer (June-July-August; top) and northern winter (December-January-February; bottom). Production in $\text{g C m}^{-2} \text{d}^{-1}$.

[Title Page](#)[Abstract](#)[Introduction](#)[Conclusions](#)[References](#)[Tables](#)[Figures](#)[◀](#)[▶](#)[◀](#)[▶](#)[Back](#)[Close](#)[Full Screen / Esc](#)[Printer-friendly Version](#)[Interactive Discussion](#)

A description of
MEDUSA-2.0

A. Yool et al.

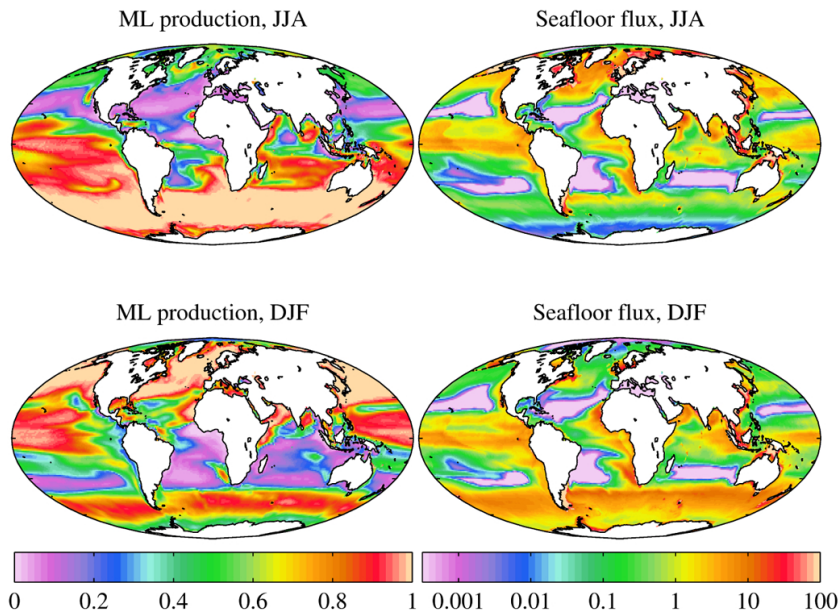


Fig. 25. Simulated mixed layer primary production fraction (left) and seafloor detrital flux (right) for northern summer (June–July–August; top) and northern winter (December–January–February; bottom). Production fraction is dimensionless; seafloor detrital flux in $\text{mg C m}^{-2} \text{d}^{-1}$, and shown on a logarithmic scale.

[Title Page](#)[Abstract](#)[Introduction](#)[Conclusions](#)[References](#)[Tables](#)[Figures](#)[◀](#)[▶](#)[◀](#)[▶](#)[Back](#)[Close](#)[Full Screen / Esc](#)[Printer-friendly Version](#)[Interactive Discussion](#)

A description of MEDUSA-2.0

A. Yool et al.

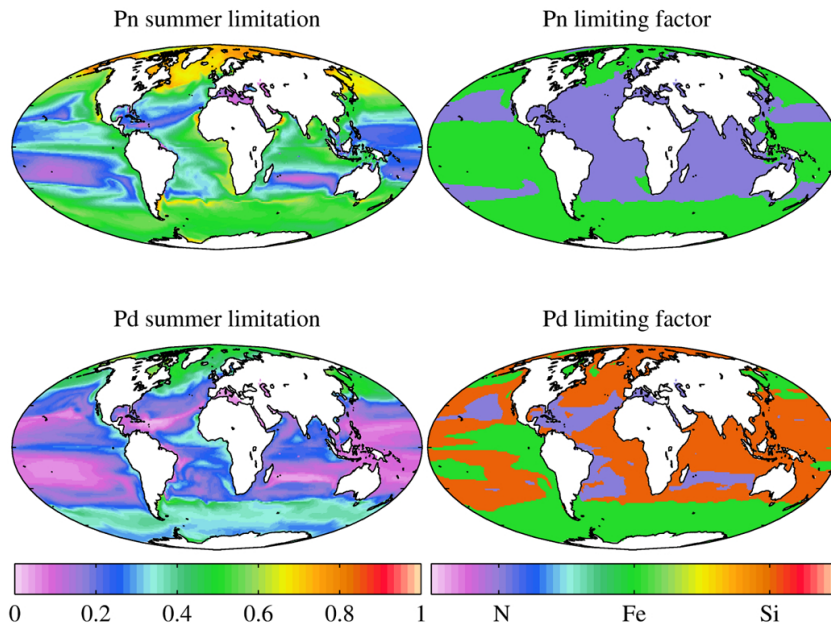


Fig. 26. Simulated summertime average non-diatom (top) and diatom (bottom) integrated nutrient limitation (left) and most-limiting nutrient (right). Limitation is weighted by biomass and integrated for the full water column. Limitation is dimensionless.

Title Page

Abstract

Introduction

Conclusions

References

Tables

Figures

◀

▶

◀

▶

Back

Close

Full Screen / Esc

Printer-friendly Version

Interactive Discussion



A description of
MEDUSA-2.0

A. Yool et al.

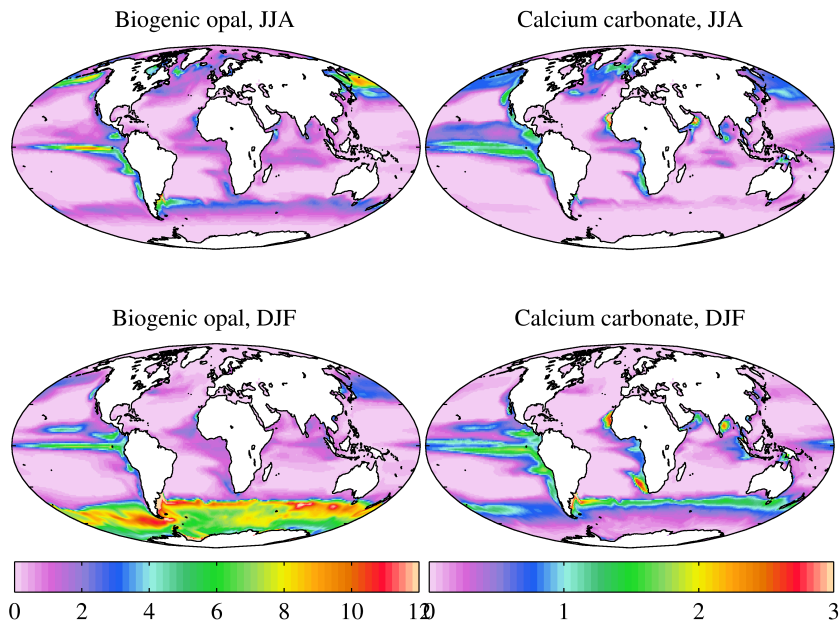


Fig. 27. Simulated diatom biogenic opal (left) and calcium carbonate (right) production for northern summer (June-July-August; top) and northern winter (December-January-February; bottom). Biogenic opal production in $\text{mmol Si m}^{-2} \text{d}^{-1}$; calcium carbonate production in $\text{mmol C m}^{-2} \text{d}^{-1}$.

[Title Page](#)[Abstract](#)[Introduction](#)[Conclusions](#)[References](#)[Tables](#)[Figures](#)[◀](#)[▶](#)[◀](#)[▶](#)[Back](#)[Close](#)[Full Screen / Esc](#)[Printer-friendly Version](#)[Interactive Discussion](#)

**A description of
MEDUSA-2.0**

A. Yool et al.

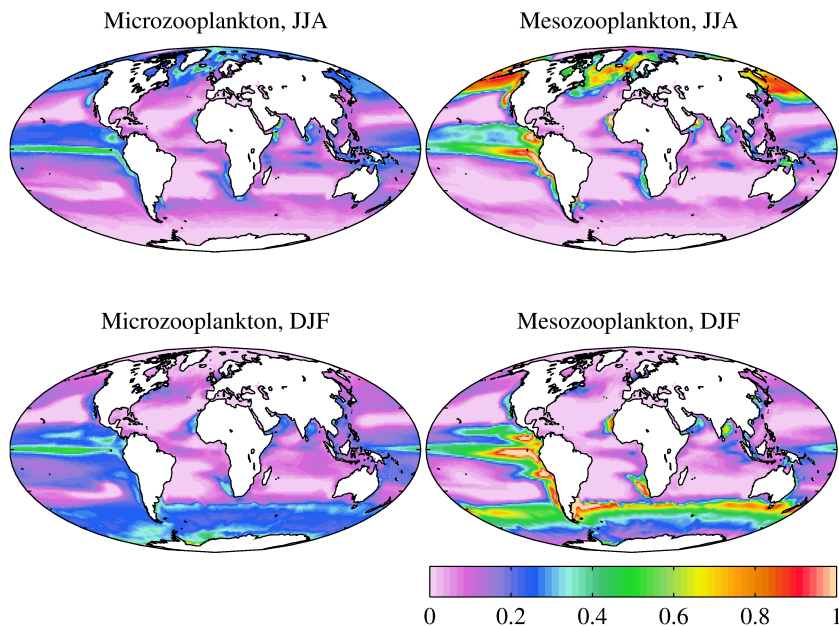


Fig. 28. Simulated surface microzooplankton (left) and mesozooplankton (right) concentrations for northern summer (June-July-August; top) and northern winter (December-January-February; bottom). Concentrations in mmol m^{-3} .

[Title Page](#)[Abstract](#)[Introduction](#)[Conclusions](#)[References](#)[Tables](#)[Figures](#)[⏪](#)[⏩](#)[◀](#)[▶](#)[Back](#)[Close](#)[Full Screen / Esc](#)[Printer-friendly Version](#)[Interactive Discussion](#)

A description of
MEDUSA-2.0

A. Yool et al.

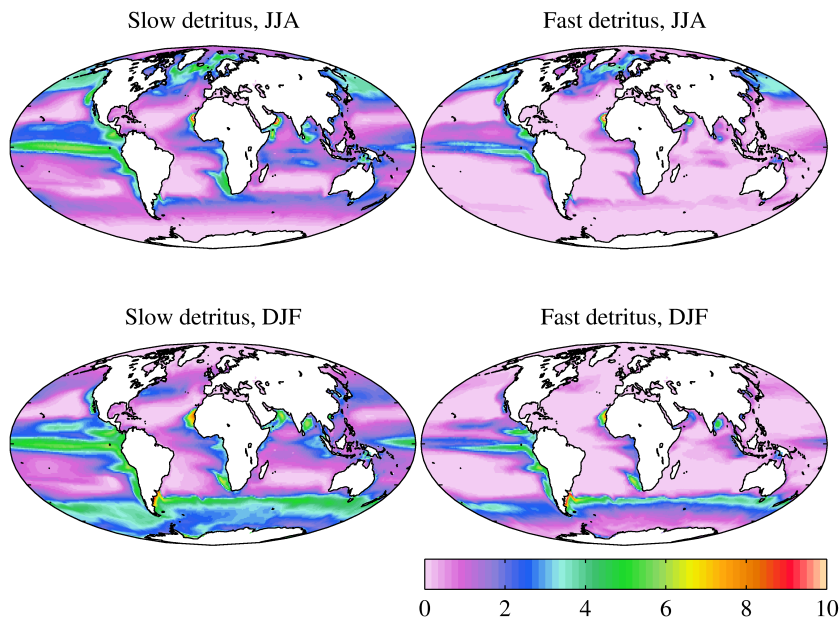


Fig. 29. Simulated slow (left) and fast (right) detritus production for northern summer (June-July-August; top) and northern winter (December-January-February; bottom). Detritus production in $\text{mmol N m}^{-2} \text{d}^{-1}$.

[Title Page](#)[Abstract](#)[Introduction](#)[Conclusions](#)[References](#)[Tables](#)[Figures](#)[◀](#)[▶](#)[◀](#)[▶](#)[Back](#)[Close](#)[Full Screen / Esc](#)[Printer-friendly Version](#)[Interactive Discussion](#)

A description of
MEDUSA-2.0

A. Yool et al.

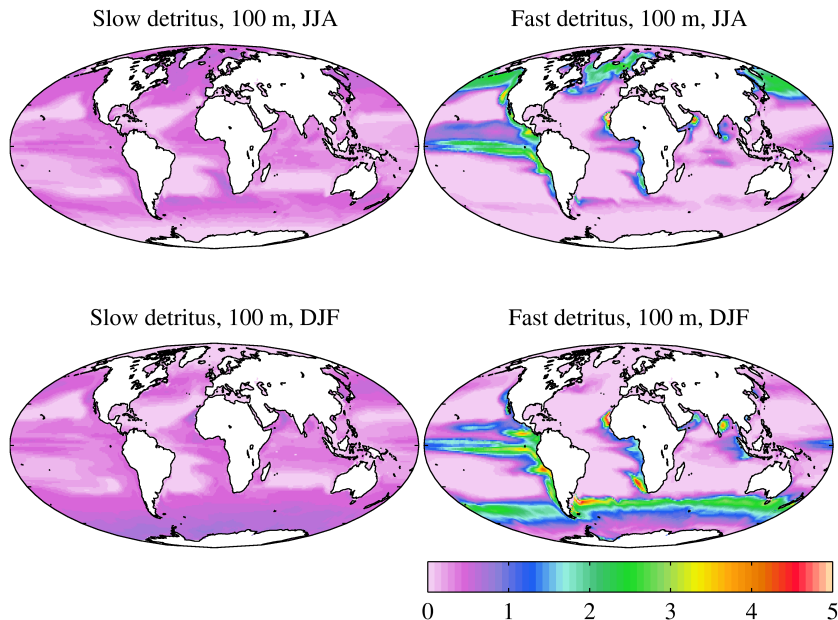


Fig. 30. Simulated slow (left) and fast (right) detrital sinking fluxes at 100 m for northern summer (June–July–August; top) and northern winter (December–January–February; bottom). Detritus production in $\text{mmol N m}^{-2} \text{d}^{-1}$.

[Title Page](#)[Abstract](#)[Introduction](#)[Conclusions](#)[References](#)[Tables](#)[Figures](#)[⏪](#)[⏩](#)[◀](#)[▶](#)[Back](#)[Close](#)[Full Screen / Esc](#)[Printer-friendly Version](#)[Interactive Discussion](#)

A description of MEDUSA-2.0

A. Yool et al.

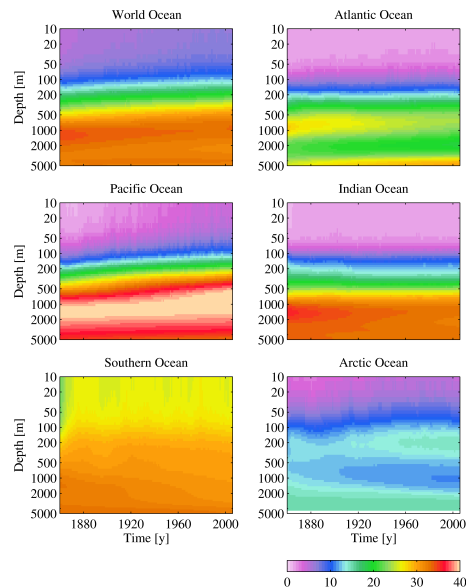


Fig. 31. Simulated vertical profiles of dissolved inorganic nitrogen concentration averaged for the World Ocean (top left) and 5 major regions. Concentrations in mmol N m^{-3} . Note that depth is shown on a logarithmic scale.

[Title Page](#)[Abstract](#)[Introduction](#)[Conclusions](#)[References](#)[Tables](#)[Figures](#)[⏪](#)[⏩](#)[◀](#)[▶](#)[Back](#)[Close](#)[Full Screen / Esc](#)[Printer-friendly Version](#)[Interactive Discussion](#)

**A description of
MEDUSA-2.0**

A. Yool et al.

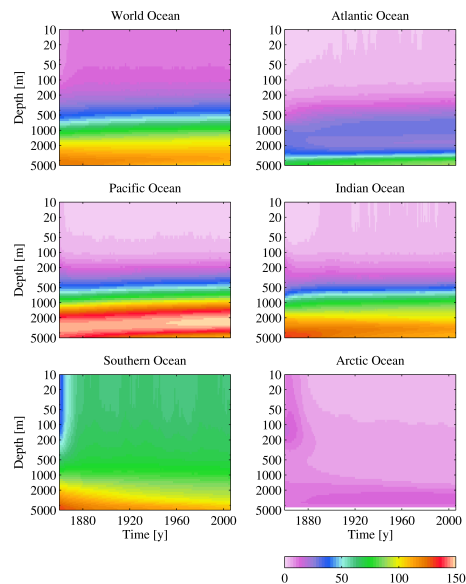


Fig. 32. Simulated vertical profiles of silicic acid concentration averaged for the World Ocean (top left) and 5 major regions. Concentrations in mmol Si m^{-3} . Note that depth is shown on a logarithmic scale.

Title Page

Abstract

Introduction

Conclusions

References

Tables

Figures

I◀

▶I

◀

▶

Back

Close

Full Screen / Esc

Printer-friendly Version

Interactive Discussion



A description of MEDUSA-2.0

A. Yool et al.

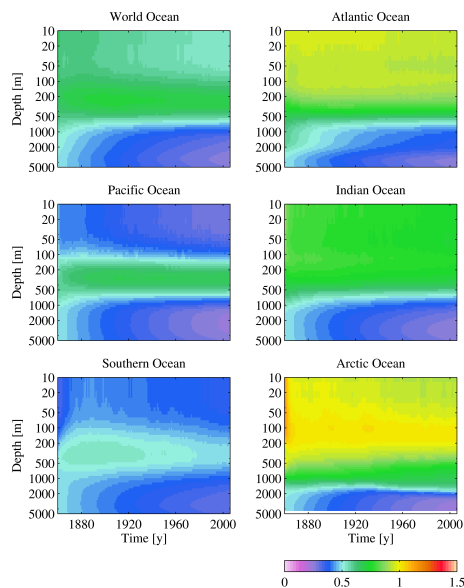


Fig. 33. Simulated vertical profiles of iron concentration averaged for the World Ocean (top left) and 5 major regions. Concentrations in $\mu\text{mol Fe m}^{-3}$. Note that depth is shown on a logarithmic scale.

[Title Page](#)[Abstract](#)[Introduction](#)[Conclusions](#)[References](#)[Tables](#)[Figures](#)[⏪](#)[⏩](#)[◀](#)[▶](#)[Back](#)[Close](#)[Full Screen / Esc](#)[Printer-friendly Version](#)[Interactive Discussion](#)

A description of
MEDUSA-2.0

A. Yool et al.

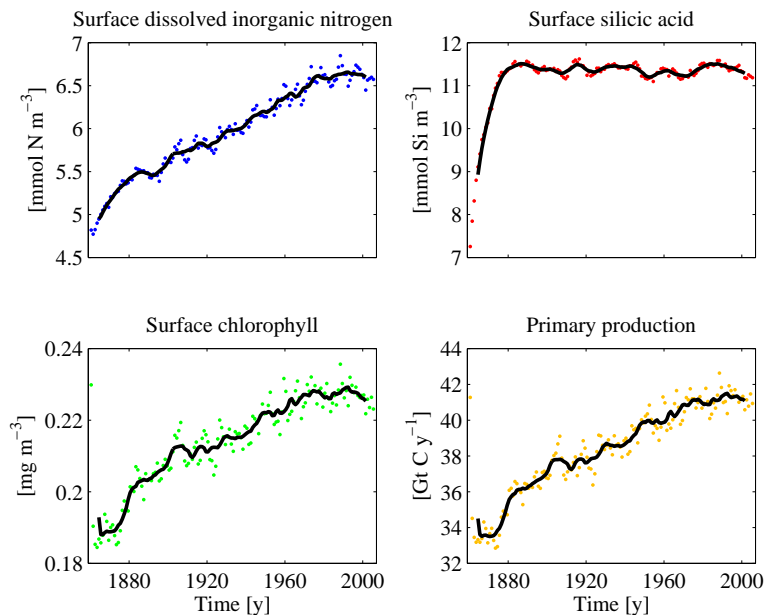


Fig. 34. Globally averaged surface dissolved inorganic nitrogen (top left), surface silicic acid (top right), surface chlorophyll (bottom left) and integrated primary production (bottom right). Solid black lines are annual averages/integral; individual points are individual months. Note that individual monthly primary production values have been normalised so that they appear on the same scale as annual integrals.

[Title Page](#)[Abstract](#)[Introduction](#)[Conclusions](#)[References](#)[Tables](#)[Figures](#)[◀](#)[▶](#)[◀](#)[▶](#)[Back](#)[Close](#)[Full Screen / Esc](#)[Printer-friendly Version](#)[Interactive Discussion](#)